

General Disclaimer

One or more of the Following Statements may affect this Document

- This document has been reproduced from the best copy furnished by the organizational source. It is being released in the interest of making available as much information as possible.
- This document may contain data, which exceeds the sheet parameters. It was furnished in this condition by the organizational source and is the best copy available.
- This document may contain tone-on-tone or color graphs, charts and/or pictures, which have been reproduced in black and white.
- This document is paginated as submitted by the original source.
- Portions of this document are not fully legible due to the historical nature of some of the material. However, it is the best reproduction available from the original submission.

PD- 75-042
March 1975

N76-11639

(NASA-CR-144041) A FEASIBILITY STUDY FOR
THE DETECTION OF UPPER ATMOSPHERIC WINDS
USING A GROUND BASED LASER DOPPLER
VELOCIMETER Final Report (Physical
Dynamics, Inc., Berkeley, Calif.) 165 p HC G3/47 02165

Unclassified

G3/47 02165

A FEASIBILITY STUDY FOR THE DETECTION
OF UPPER ATMOSPHERIC WINDS USING
A GROUND BASED LASER DOPPLER VELOCIMETER

by

J. Alex Thomson

J.C.S. Meng

Contractor: Physical Dynamics, Inc.

Contract Number: NAS8-28984

Effective Date of Contract: 18 December 1972

Contract Expiration Date: 1 April 1975

Amount of Contract: \$89,466.00

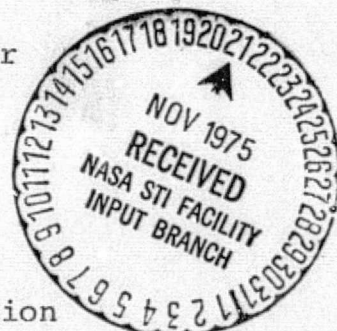
Principal Investigator: J. Alex Thomson
Phone: (415) 848-3063

Procurement Officer: Ray Weems
Phone: (205) 453-2857

Contracting Officer's Representative:
R. Milton Huffaker
Phone: (205) 453-1595

Approved for public release;
distribution unlimited.

This research was supported by the
National Aeronautics and Space Administration
and was monitored by R. Milton Huffaker,
S&E-AERO-A, NASA, Marshall Space Flight
Center, Ala. 38512, under Contract NAS8-28984.



~~UNCLASSIFIED~~

SECURITY CLASSIFICATION OF THIS PAGE (From Data Entered)

REPORT DOCUMENTATION PAGE		READ INSTRUCTIONS BEFORE COMPLETING FORM
1. REPORT NUMBER	2. GOVT ACCESSION NO.	3. RECIPIENT'S CATALOG NUMBER
4. TITLE (and Subtitle)		5. TYPE OF REPORT & PERIOD COVERED
A FEASIBILITY STUDY FOR THE DETECTION OF UPPER ATMOSPHERIC WINDS USING A GROUND BASED LASER DOPPLER VELOCIMETER		Final
7. AUTHOR(s)		6. PERFORMING LAB. REPORT NUMBER
J. Alex Thomson J.C.S. Meng		PD-75-042
8. CONTRACT OR GRANT NUMBER(s)		
9. PERFORMING ORGANIZATION NAME AND ADDRESS		10. PROGRAM ELEMENT, PROJECT, TASK AREA & WORK UNIT NUMBERS
Physical Dynamics, Inc. P.O. Box 1069 Berkeley, CA 94701		
11. CONTROLLING OFFICE NAME AND ADDRESS		12. REPORT DATE
		March 1975
14. MONITORING AGENCY NAME & ADDRESS (if different from Controlling Office)		13. NUMBER OF PAGES
George C. Marshall Space Flight Center National Aeronautics and Space Administration, Marshall Flight Center, Ala 35812		Unclassified
16. DISTRIBUTION STATEMENT (of this Report)		15a. DECLASSIFICATION/DOWNGRADING SCHEDULE
17. DISTRIBUTION STATEMENT (of the abstract entered in Block 20, if different from Report)		
Approved for public release; distribution unlimited.		
18. SUPPLEMENTARY NOTES		
19. KEY WORDS (Continue on reverse side if necessary and identify by block number)		
Clear Air Turbulence Laser Doppler Velocimeter Mountain Lee Waves		
20. ABSTRACT (Continue on reverse side if necessary and identify by block number)		
A possible measurement program designed to obtain the information requisite to determining the feasibility of airborne and/or satellite-borne LDV (Laser Doppler Velocimeter) systems is discussed. Measurements made from the ground are favored over an airborne measurement as far as for the purpose of determining feasibility is concerned.		
The expected signal strengths for scattering at various altitude and elevation angles are examined; it appears that both molecular		

DD Form 1473: Report Documentation Page

Unclassified

SECURITY CLASSIFICATION OF THIS PAGE(Initial Data Entered)

20. Abstract

absorption and ambient turbulence degrade the signal at low elevation angles and effectively constrain the ground based measurement to elevation angles exceeding a critical value.

The nature of the wind shear and turbulence to be expected are treated from a linear hydrodynamic model - a mountain lee wave model. The spatial and temporal correlation distances establish requirements on the range resolution, the maximum detectable range and the allowable integration time.

The ability of available LDV instrumentation to measure typical and shear profiles and turbulence levels is then assessed.

Analysis of the operation of LDV systems under very general conditions is given in appendix I and a mechanical shutter described in appendix II is proposed for solving the ringing problem for the pulsed LDV system.

Unclassified

SECURITY CLASSIFICATION OF THIS PAGE(Initial Data Entered)

ACKNOWLEDGMENT

The authors are greatly indebted to Frederick P. Boynton for reviewing the manuscript and helping to prepare it for publication. We also wish to thank both R. Milton Huffaker and Harold Jeffries for their many suggestions and in-depth discussions.

TABLE OF CONTENTS

	<u>Page</u>
ACKNOWLEDGMENT	i
TABLE OF CONTENTS	ii
LIST OF FIGURES	iii
ABSTRACT	v
I. SUMMARY	1
II. ANALYSIS OF A GROUND-BASED LDV SYSTEM	6
A. S/N Expressions	6
B. Loss Mechanism	8
C. System Application	11
III. MOUNTAIN LEE WAVES - A REVIEW	20
A. Phenomenology of Mountain Lee Waves	20
B. Formulation of the Model	29
1. Equation of Motion	29
2. Boundary Conditions	32
3. Transformation to Physical Variables	37
C. Results and Discussion	39
IV. ASSESSMENTS OF CURRENT SYSTEMS	66
REFERENCES	69
APPENDIX I - LASER DOPPLER VELOCIMETERS: ANALYSIS	72
2.0 Analysis	73
2.1 General	73
2.1.1 Simple Model	75
2.2 Fresnel-Kirchoff Formulation	81

LIST OF FIGURES

<u>Figure No.</u>		<u>Page</u>
1	Two way loss (db) versus scattering altitude, km. at 30° N, July, sea level.	9
2	Two way loss (db) versus scattering altitude, km. at 30° N July, 5000 ft. elevation.	10
3	Dependence of r_o on wavelength and altitude for (1-way) vertical path-lengths, average daytime conditions (from Fried) ⁸	12
4	Dependence of r_o on wavelength, range, and strength of turbulence C_N^2 for horizontal paths. (e.g., $r_o = 10$ cm for $\lambda = .63\mu$, $R = 10$ km, $C_N^2 = 10^{-15-2/3}$) (from Fried) ⁸	13
5	Physical Sketch of the Mountain Leewave	36
6a	Integration Contours for $x > 0$	
6b	Integration Contours for $x < 0$	37
7	The Vertical Profiles of the Mean Wind and the Potential Temperature	42
8	Lee Wave Profiles for the Three-layer Case with Solid Wall Upper Boundary Condition	43
9	Lee Wave Profiles for the Three-layer Case with Evanescent Upper Boundary Condition	44
10a	Potential Temperature and Wind Profiles on February 18, 1970, between Kremmling and Colorado VOR Stations	47
10b	Scorer's Parameter for Meteorological Data on February 18, 1970, between Kremmling and Colorado VOR Stations	48

LIST OF FIGURES

<u>Figure No.</u>		<u>Page</u>
11a	Potential Temperatures and Wind Profiles on February 15, 1968, near the Continental Divide	49
11b	Scorer's Parameters for the Meteorological Data on February 15, 1968, near the Continental Divide	50
12a	Sensitivity of Flow Solution Upon the Lower Portion of Meteorological Data	55
12b	Sensitivity of Flow Solution Upon the Lower Portion of Meteorological Data	55
12c	Sensitivity of Flow Solution Upon the Lower Portion of Meteorological Data	56
13	$K^2(z)$ for the Meteorological Data on February 15, 1968, over the Continental Divide	58
14	Streamline Patterns	59
15	Velocity Vector Plot	60
16	Distribution of Richardson Number (Note difference in vertical and horizontal scales)	61
17	Typical inputs for LDV Sensor Response Simulation.	62
17a	Parallel velocity along line-of-sight	62
17b	Gradient of parallel velocity along line-of-sight	62
17c	Potential temperature along line-of-sight	63
17d	Gradient of potential temperature along line-of-sight	63
17e	Richardson number along line-of-sight	64
18	V_{rms} and ΔV_{pulse} versus Pulse Time	68

ABSTRACT

A possible measurement program designed to obtain the information requisite to determining the feasibility of airborne and/or satellite-borne LDV (Laser Doppler Velocimeter) systems is discussed. Measurements made from the ground are favored over an airborne measurement as far as for the purpose of determining feasibility is concerned.

The expected signal strengths for scattering at various altitude and elevation angles are examined; it appears that both molecular absorption and ambient turbulence degrade the signal at low elevation angles and effectively constrain a ground based measurement to elevation angles exceeding a critical value.

The nature of the wind shear and turbulence to be expected are treated from a linear hydrodynamic model - a mountain lee wave model. The spatial and temporal correlation distances establish requirements on the range resolution, the maximum detectable range and the allowable integration time.

The ability of available LDV instrumentation to measure typical and shear profiles and turbulence levels is then assessed.

Analysis of the operation of LDV systems under very general conditions is given in appendix I and a

mechanical shutter described in appendix II is proposed
for solving the ringing problem for the pulsed LDV system.

I. SUMMARY

There are presently under development coherent laser detection systems designed to measure atmospheric winds and turbulence at both short and long ranges^(1,2). A continuous wave (CW) CO₂ laser system has been demonstrated to provide wind shear information at altitudes up to 500 feet and ranges to 1000 feet^(2,3). A pulsed version of the same instrument designed to detect clear air turbulence (CAT) has been mounted on an airborne platform and operated at various altitudes up to 40,000 feet⁽⁴⁾. Clear air detections at ranges up to several miles have been obtained at lower altitudes (less than 15,000 feet). Clear air returns were not consistently obtained at higher altitudes and it was concluded that greater sensitivity or more output power would be required for operation at these altitudes.

The objective of the latter program was to develop a system capable of detecting hazardous regions of turbulence (CAT) for installation in commercial aircraft, whereas the former program was oriented toward the development of scanning velocimeters that would provide data on local wind shear for various application including aircraft operations in airport environment, artillery applications, etc. In addition to these objectives, there are a number of other important applications of such remote wind shear measuring systems.

In particular, the ability to measure upper atmospheric winds on global scales from a satellite platform is sufficiently attractive for weather forecasting and meteorological studies to merit quantitative analysis of the potential of such a measurement. At a more local level these systems can be used to measure the wind shear field in and near various meteorological phenomena (fronts, large amplitude internal waves, large scale convection cells, regions of developing storms, etc.).

Preliminary tests with a pulsed coherent airborne LDV (laser doppler velocimeter) have been inconclusive, and it has not been possible to assess the feasibility of measuring winds and wind shears of long ranges from these tests alone. Uncertainties exist both in the level of the aerosol backscatter at high altitudes, as well as in the instrument performance. Attempts to sample the aerosol content using mechanical samplers have been carried out also with inconclusive results.

In this report we will discuss a possible measurement program designed to obtain the information requisite to determining the feasibility of airborne and/or satellite-borne laser doppler systems. We will argue that for the purpose of determining feasibility and for the acquisition of the requisite design information, measurements made from the ground are to be preferred over an airborne measurement.

The advantages of a ground based measurement as compared to an airborne measurement are several and include:

- 1) Availability of larger useful apertures (diameter of 2 feet or greater as compared to a probable 1-ft. aperture for an airborne system) resulting in an enhancement of S/N at a given range of about 6 db.
- 2) Availability of a relatively controlled laboratory environment for optics-laser-detectors and electronics.
- 3) Space and power limitations are not severe.
- 4) The line of sight is stable.
- 5) Ability to take extended and repeated measurements under a variety of conditions. Experiments can be repeated at relatively low cost.
- 6) Ability to make extensive use of pulse integration techniques.
- 7) Ability to utilize bread board laser and electronic instrumentation.

The disadvantages of such a measurement include:

- 1) Increased molecular absorption along the line of sight.
- 2) Degraded propagation characteristics by turbulence in the lower atmosphere.
- 3) Poorer aspect for high elevation angles for measurements of the horizontal wind vector.

- 4) Inability to resolve fine scale vertical stratifications.
- 5) A lessened ability to identify turbulence from the spectral broadening of the scattered signal (greater interference from vertical gradients in the horizontal wind).

In the following sections we first examine (Section II) the expected signal strengths for scattering at various altitude and elevation angles. It will appear that both molecular absorption and ambient turbulence degrade the signal at low elevation angles and effectively constrain the possible measurements to elevation angles exceeding a critical value. This value depends upon output power, integration or averaging time and, at least for turbulence effects, ambient conditions.

Following this analysis we treat in some detail (Section III) the nature of the wind shear and turbulence to be expected. The nature of the vertical profile and the spatial and temporal correlation distances establish requirements on the range resolution, the maximum detectable range and the allowable integration time.

The ability of available LDV instrumentation to measure typical wind shear profiles and turbulence levels is then assessed (Section IV). Both ground and airborne platforms are considered. For a ground based measurement, it is

concluded that extensive pulse integration techniques may be needed to derive wind profiles up to 10 km, depending on the actual value of the backscatter coefficient. For detection of winds at the tropopause, the elevation angle is probably limited to being greater than 30°. This implies a minimum vertical resolution of the order of 300 meters.

The current available pulsed LDV system⁽¹⁾ has a ringing problem that limits the minimum detectable relative velocity. Since expected relative velocities at lower altitudes are relatively small, techniques for eliminating this ringing are required. One such technique using a mechanical shutter is described in Appendix II.

In Appendix I, an analysis of the operation of LDV systems under very general conditions is given. Most of this material has been taken from a previous limited-distribution report (Thomson and Dorian, 1967), which is presently unavailable and is included here for completeness.

II. ANALYSIS OF A GROUND-BASED LDV SYSTEM

In this section the expected signal to noise ratio (SNR) for a ground-based pulsed LDV is evaluated. Expressions for the SNR derived from the general analysis of LDV operation in Appendix I are given. Atmospheric losses due to molecular absorption and turbulence are significant for the proposed ground based system even under good seeing conditions, and limit the measurement of elevation angles greater than 30 degrees. The single-pulse SNR's are small for the current system (pulse energy 20 mJ, aperture diameter 30 cm); increased power (200 mJ) or larger optics (~ 50 cm) would be required to achieve a marginally detectable signal on a single-pulse basis. Further improvement requires pulse integration. The ground-based measurement is found to have an SNR comparable to or slightly higher than an equivalent airborne system for similar conditions. A comparison of the ground-based LDV system with the Wallops Island radars, which have detected CAT produced by high-altitude internal waves, shows that the SNR's can be of the same order.

A. S/N Expressions

For a pulsed system operating in a collimated mode (focused at infinity), the SNR is

$$S/N = \eta \frac{J}{32 hc/\lambda} \frac{D^2 n\sigma ct}{R^2 + \left(\frac{\pi D^2}{4\lambda}\right)^2}$$

where

J = net output energy in the observation time

D = aperture diameter

τ = pulse time

$\overline{n\sigma}$ = particle density times scattering cross-section
(mean value at range R)

η = detection efficiency

R = range

L = propagation loss factor

The factor L is the product of the molecular loss L_{mol} and
the turbulent loss L_{turb} .

At ranges less than the Rayleigh distance ($R_* = \pi D^2 / 4\lambda$),
the signal to noise ratio varies with range only as a result
of the loss factor L :

$$S/N \approx \eta \frac{J}{2\pi^2 h\nu} \frac{\overline{n\sigma} \lambda^2 c\tau}{D^2} L(R) \quad \text{for } R < R_*$$

For a 30 cm effective aperture diameter and $\lambda = 10.6\mu$, this
expression is appropriate for ranges less than about 7 km.

Within the range limits, some benefit can be obtained
by focusing on the range interval of primary interest. For
pulse lengths less than the focal depth ($\frac{c\tau}{2} < 4R^2\lambda/D^2$), the
signal to noise from the region near the focal point is

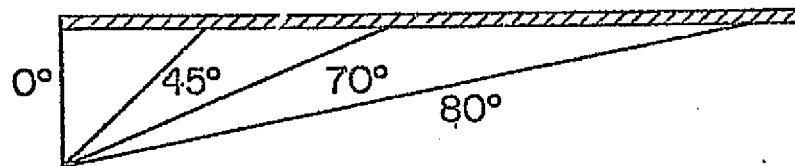
$$S/N = \eta \frac{J\lambda}{32hc} \frac{D^2}{R^2} \frac{\overline{n\sigma}_c \tau}{L(R)}$$

and exhibits an inverse square dependence on range in addition to the range dependence through the propagation loss factor.

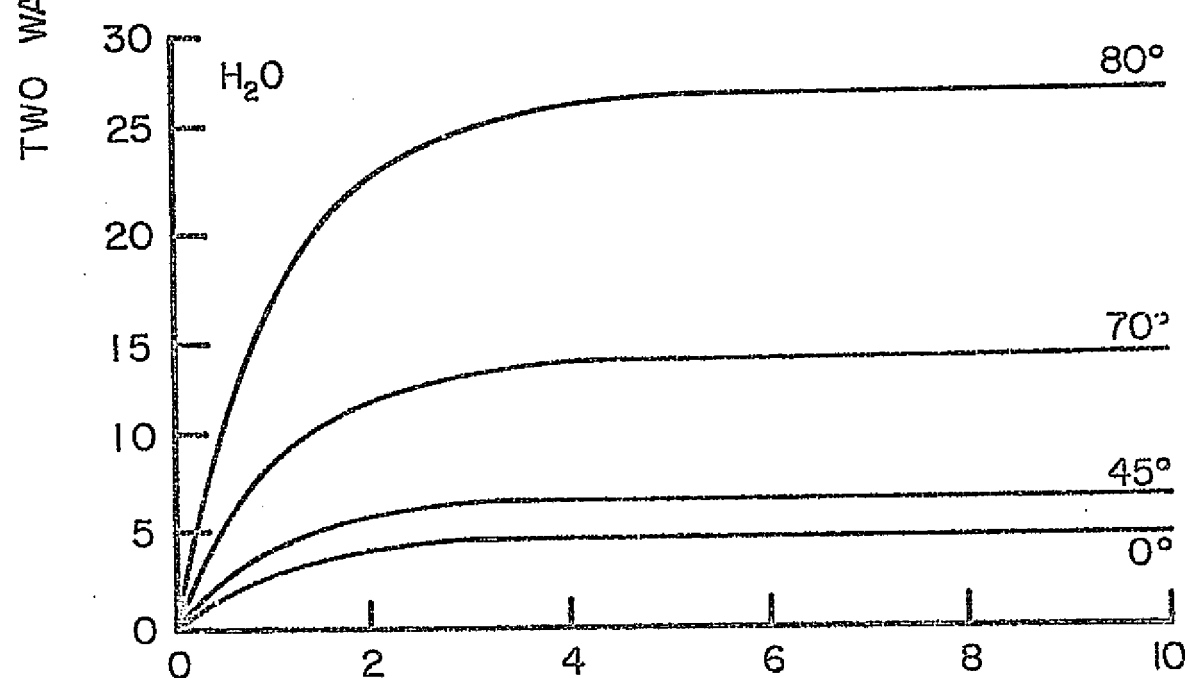
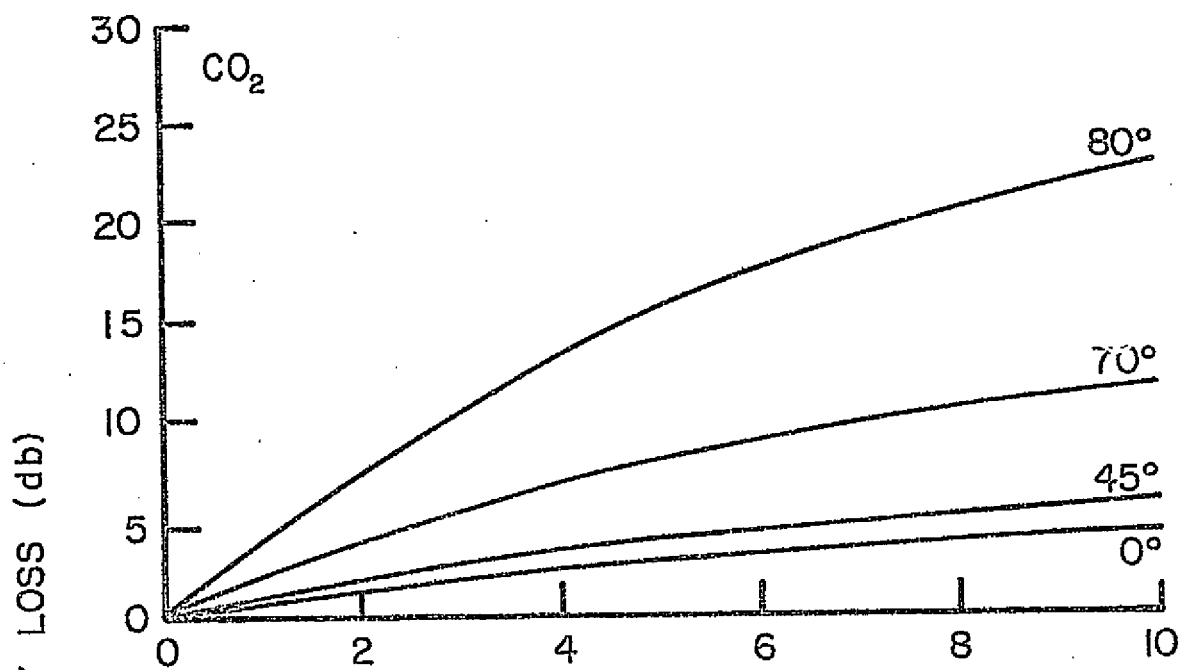
B. Loss Mechanism

Molecular absorption results principally from CO₂ lines and the wings of the nearby water vapor bands. Two-way absorption losses as a function of the altitude at which the light is scattered are given in Figure 1 for various elevation angles of the line of sight. For a sea level installation, the losses are moderate (less than 12 db) only for elevation angles (above the horizon) greater than 45°. An improved situation exists for a higher altitude installation under low humidity conditions. In Figure 2 two-way losses are shown for a source located at an elevation comparable to that at Boulder, Colorado (~ 5,000 feet).

Under conditions of strong surface heating, low altitude turbulence will materially degrade the returns from the higher altitudes. The signal to noise ratio in this case is conveniently expressed in terms of an effective coherent aperture radius r_a (r_a is related to Fried's effective aperture diameter r_o according to r_o = 3.18 r_a)³. When r_o is small compared to the actual aperture D, the optimum signal to noise (that obtained when the beam is focused on the range point of interest) is given by

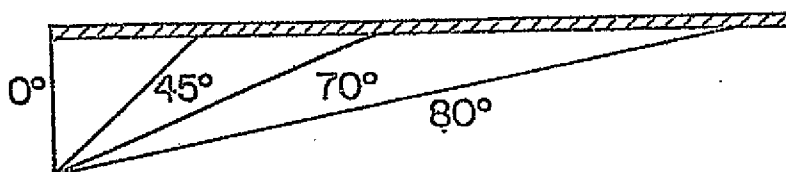


30° N, JULY, SEA LEVEL

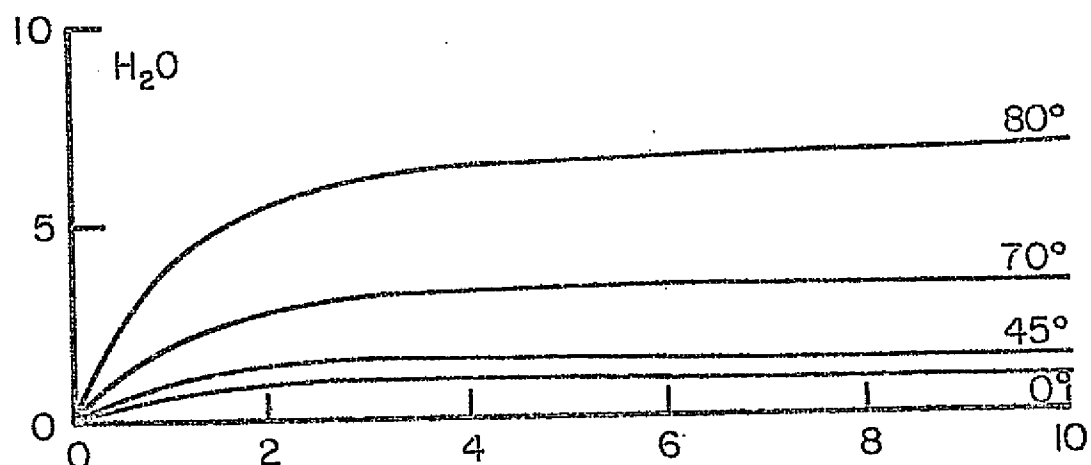
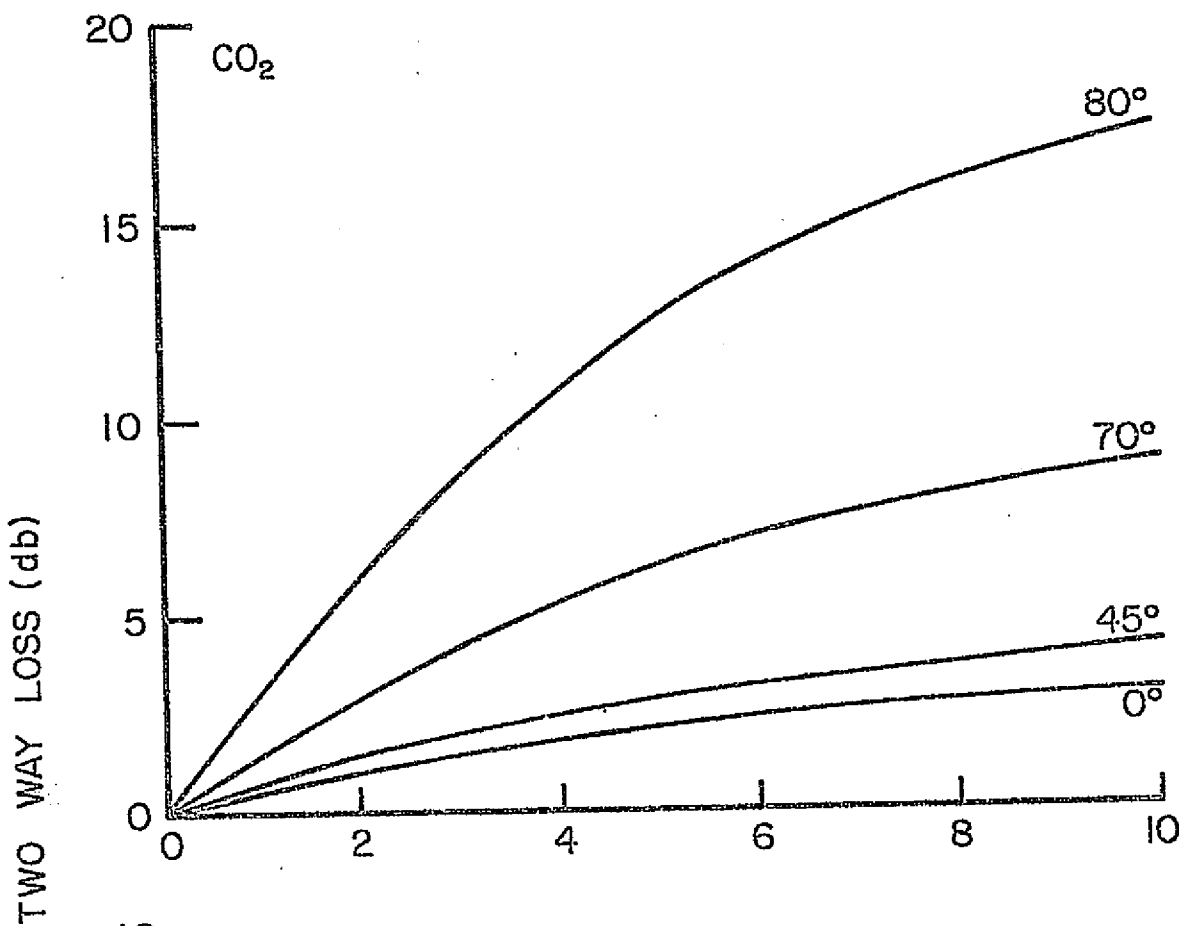


SCATTERING ALTITUDE, km.

FIGURE 1



30°N, JULY, 5000 FT. ELEVATION



SCATTERING ALTITUDE, km.

FIGURE 2

$$\text{S/N} = \frac{\eta}{8} \frac{J}{hv} \overline{n\sigma} \frac{r_a^2}{R^2} c\tau$$

In Figures 3 and 4 we have reproduced Fried's figures for effective apertures for both horizontal and vertical paths. These data may be scaled to finite elevation angles by the relation

$$r_a = 0.0581 \lambda^{6/5} / (C_N^{6/5} R^{3/5})$$

where R is the slant range. For a vertically stratified atmosphere, the following expression should be used:

$$r_a = 0.581 \lambda^{6/5} \cos^{3/5} \theta / \left(\int_0^H C_N^2 dz \right)^{3/5}$$

where θ is the angle from the vertical and H the scattering height.

C. System Application

The preceding relations have been used to derive estimates for expected signal to noise ratios for a suggested ground measurement. These values are shown in Table I. Under moderate to good seeing conditions ($\int_0^\infty C_N^2 dz < 7 \times 10^{-12} \text{ meters}^{1/3}$) turbulence is not a significant degrading factor for 30 cm optics. In Table I we have assumed an overall optics-detector-electronics efficiency η of 2.0 percent. Theoretically, it should be

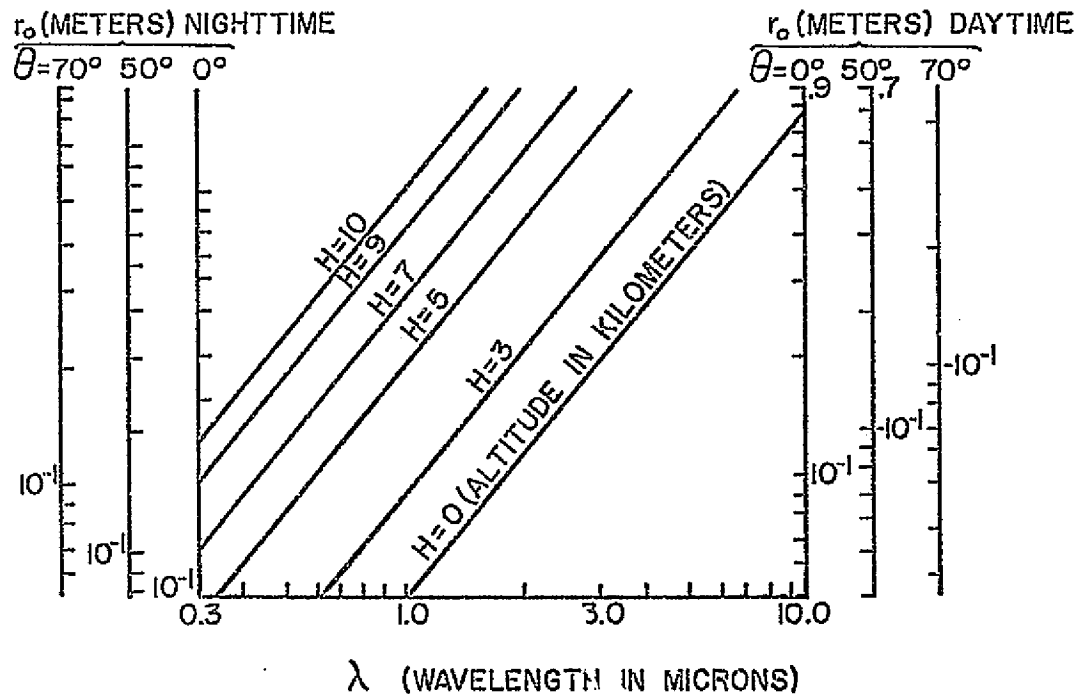


Figure 3. Dependence of r_o on wavelength and altitude for (1-way) vertical path lengths, average daytime conditions (from Fried⁸)

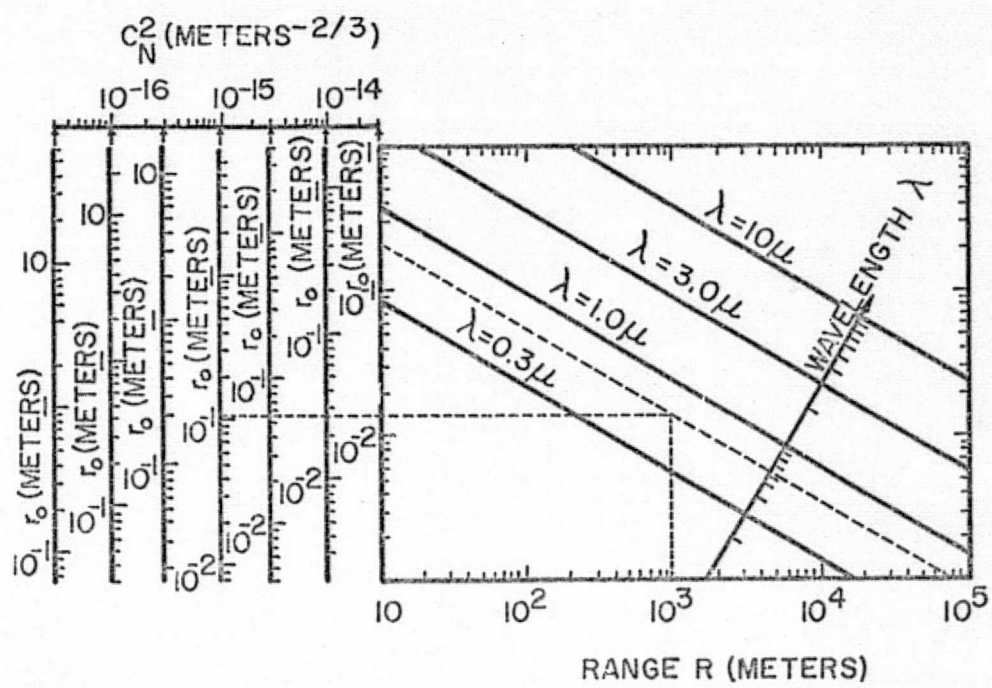


Figure 4. Dependence of r_o on wavelength, range, and strength of turbulence C_N^2 for horizontal paths. (e.g., $r_o = 10$ cm for $\lambda = .63 \mu$, $R = 10$ km, $C_N^2 = 10^{-15} \text{ m}^{-2/3}$)
(from Fried⁸)

TABLE I: Ground-Based LDV System

Aperture diameter D = 50 cm

$$C_n^2 < 3 \times 10^{-15} \text{ m}^{-2/3}; \int C_N^2 dz < 7 \times 10^{-12} \text{ m}^{1/3}$$

Detection Altitude: 10 km

Angle from Vertical: 45°

Pulse: 2 μ sec (8 μ sec)

$$\overline{n\sigma} = 10^{-6} \text{ km}^{-1} \text{ ster}^{-1}$$

Absorption = 6 db

System/Detector Efficiency = 0.02

Single Pulse SNR

Pulse Energy	S/N
20 mj	0.24 (0.8)*
200 mj	2.4 (8)

Integrate 600 pulses incoherently

Pulse Energy	S/N
20 mj	6.4 (19)*
200 mj	64 (190)*

*Values in parentheses correspond to the 8 μ sec pulse length.

possible in a pulsed system to achieve efficiencies approaching the detector quantum efficiency (30-50%). However, current estimates for the airborne system are much lower and we choose 2% as a currently achievable value. Two pulse lengths are considered: 2μ sec and 8μ sec. At an elevation angle of 45° , these imply a vertical resolution of 300 and 900 meters respectively. For these parameters the single pulse SNR's are below detectability for a 20 mj pulse and are marginal for a 200 mj pulse. Since the external losses in this case are only 6 db, similar numbers (actually, a factor 4 higher) will apply to the airborne platform measurement at the same range (14 km).

Under these conditions the single pulse signal to noise ratios are very low for the current system capability ($J < 20$ mj) and substantial increases in pulse output at power or sensitivity would be required for detection. Integration (incoherent) of 600 or more pulses is required to bring the SNR up to acceptable values. It should be noted that these values apply to the entire signal and implicitly assume that the doppler spread in the returning signal is no greater than the inverse of the pulse width, that is, 100 to 500 K Hz (or 0.5 to 2.5 meters per second). Substantial velocity gradients along the line of sight or significant turbulence levels will broaden the signal beyond these limits, further reducing the SNR.

The above estimates imply that substantial pulse integration may be required to obtain useful data. The maximum allowable integration time is limited by the air transit time through the resolution volume. For a ground-based system this time is

$$\Delta t = \frac{c\tau}{2} \frac{\sin\theta}{V_w}$$

where V_w is the horizontal wind velocity. For our nominal system with $\tau = 5\mu$ sec and a wind velocity of 40 meters/sec, integration times of the order of 13 seconds are permitted. In the equivalent airborne system (travelling at a relative velocity of 300 m/sec) the integration time would be about 2.5 seconds. At a pulse repetition rate of 200 pps and 20 mj pulses (mean power of 5 KW), the ground-based system could average over 2600 pulses, yielding an SNR of about 7.6 (~ 9 db) as compared to the airborne system value of 6.6.

Thus, we conclude that, where operated under similar conditions, the ground-based measurement would achieve comparable or slightly higher S/N than the airborne measurement. The available increase in integration time in the ground system compensates for the increased absorption in the lower atmosphere. However, the signal to noise ratios predicted in this somewhat conservative estimate are not high (less than 10 db). For these estimates we have assumed that a

spatial resolving power comparable to .3 km to 1 km. was required. Improved SNR could be attained in the ground system by increasing the integration time to times of the order of the natural internal wave period of the stratosphere (typically several minutes). Also, the pulse duration could be chosen to match more closely the velocity spread expected. The major source of CAT at high altitudes (see Section III) is presently surmised to be the instability of large amplitude internal waves near the tropopause. These waves and their instabilities have been detected by high power sensitive radar. In Table II we present comparative data for the Wallops Island radars and for the laser system described above.

Since the laser system provides a measurement of the mean velocity parallel to the line of sight in the coherence volume (or, by time differentiation, its gradient: $dV_{||}/dr$), and the radar detects the rms refractive index fluctuations, simultaneous measurements at comparable sensitivities of scattering from the upper atmosphere can be expected to be a fruitful source of information on atmospheric motion and turbulence. A laser system such as the one described cannot be considered as an operational tool for detection of high altitude CAT on a routine basis because of the constraints of clear weather and good seeing conditions. However, as a research tool, it appears to offer considerable promise if

TABLE II

Comparison of Signal/Noise per Pulse for Ground-Based Laser
and Radar Detection at 10 km Altitude

System Characteristics

Wallops Island Radars		10.6 Coherent Laser
Pulse Energy	Resolution	
UHF 6 joules	150 m	Pulse energy: 200 mJ
S band 3	150 m	Pulse length: 2 μ sec
X band 1.8	300 m	Aperture: 50 cm
		Efficiency: $\eta=0.02$
		Absorption loss: 6 db

Signal/Noise Ratio per Pulse

Radar			
c_n^2	S/N		
	UHF	S	X
$2.1 \times 10^{-16} \text{ m}^{-2/3}$	420	70	5
$0.21 \times 10^{-16} \text{ m}^{-2/3}$	42	7	0.5

	CO_2 Laser	
$\text{no}(10.6\mu)$	(S/N) (single pulse)	(S/N (600 pulses- incoherent)
$10^{-6} \text{ km}^{-1} \text{ ster}^{-1}$	2.4	64

an overall efficiency factor of 2% can actually be achieved and if the backscattering conditions at 10.6μ are as high as assumed here.

In general, two modes of operation may be envisaged, one where the line of sight is fixed in space and the returning signal is spectrally analyzed or filtered to yield the distribution of velocities in the scattering medium, and another mode which requires measuring only the mean frequency offset or mean velocity of particles in the coherence volume and presenting this data as a function of range and angular inclination of the line of sight. This latter mode of presentation has the advantage of allowing presentation of the local mean velocity as a function of range and elevation angle while only being about 3 db in signal/noise below the full bandwidth signal.

III. MOUNTAIN LEE WAVES - A REVIEW

Mountain lee waves are an important source of CAT. An authoritative and comprehensive survey of mountain lee waves theories, including many historical references and selected references of recent work in the USSR, can be found in Miles (1969). A more recent review was given by Vergeiner (1971). We shall draw from these and other sources to describe the phenomenology of the mountain lee waves and then discuss the implementation of a linear model to represent the velocity fields. In Section IV, we discuss the nature of a simulated LDV sensor response.

A. Phenomenology of Mountain Lee Waves

Standing wave trains of wavelengths of the order of 15 km and vertical amplitudes of perhaps .5 km are frequently found in the lee of mountain ranges and may extend for several complete cycles downwind. Many well-documented cases are given by Holmboe and Klieforth (1957) and Aanensen (1965). This stationary pattern of waves may also extend with substantial amplitude upwards into the stratosphere, where it is occasionally made visible by mother-of-pearl clouds in the height range of 20 to 30 km (Hesstvedt, 1958). In general, the vertical wavelengths are of the order of 1.2 km and horizontal wavelengths of 50 km or more; the periods (the inverse of Brunt-Väisälä frequency) are in

the range of 10 to 200 minutes. The propagating velocity relative to the wind at cloud height is about 80 m/sec. The mountain lee waves are basically a regulated motion of a stably-stratified atmosphere when it is perturbed. The perturbing force pushes the atmosphere away from equilibrium while the gravitational force acts to pull it back. Much of the phenomenology of the lee waves can be visualized by considering a stable configuration composed of two flowing layers of different density. As they flow over a finite mound, the fluids are displaced so that part of the total energy is transferred to potential energy to move the heavier fluid upwards. However, due to the conservative nature of the system in the absence of dissipative mechanisms, a continuous interchange between potential and kinetic energy is established so that an oscillatory motion (internal gravity wave) is formed. Depending upon the nature of the fluid layers, their degree of stratification, the vertical dimensions of the fluid, and the relative dimensions of the mound, it is conceivable that certain modes of the oscillation (resonant waves) are more excited than others. In the lee of the mountains, these resonant waves are the only ones that do not decay rapidly with distance downstream and are usually referred to as the 'lee waves'.

We can consider the surface of discontinuity between these two fluids mentioned above as a wave guide on which

the gravity wave travels; as a matter of fact, ocean surface waves are another extreme example of ducted waves. In the atmosphere, however, no such discontinuous surfaces exist, but layers of varying stratification (or layers of different stability $\beta \equiv -\frac{g}{\rho} \frac{dp}{dz}$) are imbedded within each other. The layer of higher stability (β large) imbedded in a region of lower stability (β small) forms a duct or wave guide for horizontal propagation of internal gravity waves.

This phenomenon was demonstrated by Whitham (1971), starting from the dispersion relation for the gravity wave

$$\omega^2 = \frac{\omega_0^2 k_x^2}{k_x^2 + k_z^2} .$$

ω_0 is the Brunt-Väisälä frequency. Whitham indicated that no gravity waves are possible except when $\omega \leq \omega_0$. But because $\nabla p \times \nabla(\frac{1}{\rho}) = g \frac{\nabla \theta}{\theta} \times \vec{k} \equiv \beta$, where θ is potential temperature and \vec{k} is now the vertical unit vector, the amount of vorticity generated in a stratified flow is exactly the square of the Brunt-Väisälä frequency. Therefore, the layer of higher stability can carry higher amounts of vorticity or disturbance than its neighboring layers. If the vorticity contained in the gravity wave of frequency ω is greater than ω_0^2 , either viscous damping or acoustic radiation must take place in order to maintain the wave form. In fact, this was the early version

of Richardson's criterion of stability, i.e.

$$\Omega^2 < \frac{g}{\theta} \frac{d\theta}{dz}$$

or

$$R_i > 1.$$

The more commonly adopted critical Richardson's number is 1/4, which can be derived by balancing the potential energy required to move the heavier fluid upwards and the kinetic energy contained in the flow motion [see Ludlam (1967)]. Whitham also indicated that the gravity wave is transverse, i.e., the group velocity

$$\vec{c}_g = \left(\frac{\omega_0 k_z^2}{k^3}, - \frac{\omega_0 k_x k_z}{k^3} \right)$$

is perpendicular to the wave vector (k_x, k_z) , so that a linear model can be applicable to larger amplitudes than when it is applied to the problems of (say) an acoustic wave.

The importance of the ducting phenomena to the present study is revealed in the following aspects: first, only ducted modes are apt to be found at or near the disturbance source altitude when observations (such as the LDV measurements) of internal gravity waves are made at some lateral distance away from the source. Second, since the ducted modes are confined in the duct for a long period

of time, large wave amplitude resonance, for example the lee waves, often are realized. Specific studies of this ducting process were made by Jones (1972) and Danielsen and Bleck (1970).

The relationship between the presence of the ducted internal gravity waves to CAT has long been sought in hopes that it may explain why CAT appears as sporadic patches in a free atmosphere isolated from any visible vertical convective activity, and how and from where CAT derives its energy. Work by Scorer, Bretheren and Hines has illuminated this relationship. The phenomena of wave resonance, the ducted waves process and the discovery of the existence of a critical level in the atmosphere and the energy transferring mechanism between the mean wind shear and the internal waves are all involved. Booker and Bretheren (1967a) found the critical level (which is defined as the altitude where the wave's horizontal phase velocity is equal to the mean wind velocity). Above which the solution shows no disturbance; however, large amplitude perturbations build up underneath the level so that the breakdown into turbulence is possible. Evidence of this critical level was presented by Gerbier and Berenger (1961) who reported turbulence found by glider pilots at such heights with little or no lee wave action above. The effect of this level was analyzed through a series of papers by Bretheren (1966,

1967a, 1967b, 1968, 1969a, 1969b) and Hazel (1967). In summary, the mechanism of this critical level is to reabsorb the internal gravity wave energy back to the mean wind flow. Bekofske and Liu (1972) demonstrated that the mean wind shear is enhanced by this mechanism so that the local Richardson number is reduced to a value smaller than 1/4. The process eventually leads to Kelvin-Helmholtz instabilities and thus causes turbulence production.

Other physical aspects of lee waves are: 1) upstream propagation of disturbances in a stratified medium; 2) the effect of the earth's rotation upon the flow; 3) three-dimensionality effects.

The disturbances caused by a barrier in an ordinary homogeneous fluid flow usually decay very rapidly upstream. Therefore, the description of the upstream boundary condition is not very critical. However, in a stratified fluid flow, the disturbances propagate far upstream by riding on the internal waves, so that the details of the upstream conditions are quite important. In reality, viscosity ensures that the disturbance is dissipated at a finite distance upstream. But unless the practical application warrants the mathematical complexities required to include either viscous effects or to treat the problem from an unsteady point of view, it is necessary to remove the upstream

perturbations a priori. Scorer (1949) arbitrarily added terms to the solution to cancel disturbances generated at positions far upstream; Danielsen and Bleck (1970) and Vergeiner (1971) chose the complex integration contour to ensure that the upstream disturbances are very small.

For a small enough wavelength λ , the effect of the earth's rotation can be neglected. This can be shown by comparing the quantities gH to $U\Omega\lambda$. The former represents the maximum potential energy required to flow over the mountain height H (~ 1 km); the latter measures the kinetic energy due to the earth's rotation. Substituting typical values in lower atmosphere, U (wind speed) ~ 100 m/sec, $\Omega \sim 7 \times 10^{-5}$ rad/sec, $\lambda \sim 50$ km, we have $\frac{gH}{U\Omega\lambda} \sim 35$. Therefore, unless waves have wavelengths of thousands of kilometers (i.e., comparable to the earth's radius), the energy derived from the earth's rotation contributes little to the wave motion.

Although a fully three-dimensional analysis can be formulated much the same way, for example by Scorer (1953, 1956), nearly all analyses in the literature are two-dimensional. This is partly due to the dearth of meteorological data collected on a horizontal plane and partly because most essential information can be derived from the understanding of a simpler two-dimensional analysis. Basically, Scorer's investigations indicate that in addition to the waves on the vertical plane containing the flow direction,

transverse wave systems are created by the lateral flow around the mountain. The disturbances behind the mountain would interfere with each other. The portion of the air flow around the mountain reduces the mass of air passing over it and leads to a reduction of wave amplitude and a comparatively rapid damping downstream. Therefore, one can believe that a 2-D model should provide an upper bound upon the wave amplitude. One should bear in mind, however, that three-dimensional effects, such as the convective instability and the preferred ducting cones (Jones, 1972) are excluded.

The present model will be formulated according to the following assumptions: the processes are rapid enough to be adiabatic, the disturbances of velocity are small compared to the free stream mean wind, and the displacement is a small fraction of the layer depth. The earth's rotation is negligible, and the Boussinesq approximation is valid for gravity waves in a compressible atmosphere.

We will follow a procedure here similar to that of Danielson and Bleck (1970). The stratified atmosphere is divided into several layers; each is assigned a constant value of Scorer's parameter. The linearized equation of motion is Fourier-analyzed in the horizontal direction. The resonant wave modes are then solved as an eigenvalue problem. The inverse Fourier transform is performed on

the complex plane as a contour integral. Contours are chosen to include the poles and to minimize the computation. Sample calculations are performed for two sets of data collected by Lilly (1971) on February 18, 1970, along the cross-section between the Kremmiling and Colorado VOR stations, and on February 15, 1968, near the continental divide (given by Lilly and Toutenhoofd (1969)).

⑩

B. Formulation of the Model

1. Equation of Motion

The linearized equations of motion for steady horizontal two-dimensional flow of a vertically stratified atmosphere in the Boussinesq approximation have been shown (Bretherton, 1966 and Vergeiner, 1971) to be reducible to the form

$$\frac{\partial^2 \phi}{\partial z^2} + \frac{\partial^2 \phi}{\partial x^2} + K^2(z)\phi = 0 \quad (1)$$

where x is the direction of the unperturbed wind and z the vertical direction. The coefficient $K^2(z)$ is given by

$$K^2(z) = \frac{g}{\theta} \frac{\partial \theta}{\partial z} \frac{1}{U^2} - \frac{1}{U} \frac{\partial^2 U}{\partial z^2} \quad (2)$$

Here $U(z)$ is the horizontal wind and θ is the "potential" temperature:

$$\theta = T \left[\frac{p_0}{p(z)} \right]^{\frac{\gamma-1}{\gamma}} \quad (3)$$

where T is the temperature at altitude z , $p(z)$ is the pressure at that altitude and p_0 is a reference pressure (conveniently the surface pressure). The quantity ϕ can be taken as the streamline vertical displacement, the streamline slope or the vertical velocity as desired. We will find it convenient

to choose $\phi(z)$ to represent the streamline displacement since this quantity is continuous even though there may be discontinuities in the horizontal wind profile $U_0(z)$.

Several investigations have shown how lee waves develop downstream of mountain ridges (Scorer, 1948; Foltz, 1966; Danielsen and Bleck, 1970). We follow a procedure here similar (although not identical) to that of Danielsen and Bleck. We think of the atmosphere as being divided into a number of horizontal layers in each of which we approximate $K(z)$ as having a constant value (Figure 5). The n th layer lies between the altitudes of z_n and z_{n+1} and in this layer $K(z) = K_n$.

To solve Equation (1) subject to boundary conditions at the bottom and the top of the atmosphere, we Fourier analyze the lower boundary profile in the form

$$h(x) = \int_{-\infty}^{\infty} \zeta_{k_x} e^{ik_x x} \frac{dk_x}{\sqrt{2\pi}} \quad (4)$$

The general solution for the displacement may be written in terms of its Fourier components,

$$\phi(z, x) = \int_{-\infty}^{\infty} \phi_{k_x}(z) e^{ik_x x} \frac{dk_x}{\sqrt{2\pi}} \quad (5)$$

The equations for the coefficients ϕ_{k_x} have the form

$$\frac{\partial^2 \phi_{k_x}}{\partial z^2} + (K^2(z) - k_x^2) \phi_{k_x} = 0 \quad . \quad (6)$$

In each layer we assume $K(z)$ to have a constant value (k_n) . The solution in the nth layer is

$$(\phi_{k_x})_n = A_n(k_x) e^{+ik_n(z-z_n)} + B_n(k_x) e^{-ik_n(z-z_n)} \quad (7)$$

where

$$\kappa_n = \sqrt{K_n^2 - k_x^2} \quad .$$

Continuity of value and slope* relate A_{n+1} and B_{n+1} to A_n and B_n :

$$A_n e^{ik_n(z_{n+1}-z_n)} + B_n e^{-ik_n(z_{n+1}-z_n)} = A_{n+1} + B_{n+1} \quad (8)$$

and

$$\kappa_n \left[A_n e^{ik_n(z_{n+1}-z_n)} - B_n e^{-ik_n(z_{n+1}-z_n)} \right] = \kappa_{n+1} [A_{n+1} - B_{n+1}] \quad .$$

In terms of the vectors $\psi_n = \begin{pmatrix} A_n \\ B_n \end{pmatrix}$ we have the recursion relation

$$\psi_{n+1} = C_n \psi_n \quad (9)$$

where $C_n(k_x)$ is a 2×2 matrix of the form:

*Continuity of slope is required to conserve mass.

$$c_n = \frac{1}{2} \begin{pmatrix} \alpha \left(1 + \frac{\kappa_n}{\kappa_{n+1}}\right), \alpha^{-1} \left(1 - \frac{\kappa_n}{\kappa_{n+1}}\right) \\ \alpha \left(1 - \frac{\kappa_n}{\kappa_{n+1}}\right), \alpha^{-1} \left(1 + \frac{\kappa_n}{\kappa_{n+1}}\right) \end{pmatrix} \quad (10)$$

$$\text{where } \alpha = \exp[i\kappa_n(z_{n+1} - z_n)]$$

2. Boundary Conditions

2.1 The upper Boundary

At the top layer we have two possible boundary conditions. For the first, the level z_{N+1} is taken to be a rigid horizontal surface (i.e., there is no motion in the Nth layer). Here we must set $A_N \exp[i\kappa_n(z_{N+1} - z_N)] + B_N \exp[-i\kappa_n(z_{N+1} - z_N)] = 0$. For the other boundary condition we choose the Nth layer to be infinite in extent and require that no energy be propagating downwards from above. This state may be achieved only by setting $B_N = 0$. Thus our upper condition has one of the following forms

$$A_N \exp[i\kappa_N(z_{N+1} - z_N)] + B_N \exp[-i\kappa_N(z_{N+1} - z_N)] = 0$$

$$\text{or } B_N = 0 \quad . \quad (11)$$

2.2 Lower Surface Boundary Condition

For the general case of a homogeneous upper boundary condition we can write

$$\psi_N = A_N \epsilon_0 \quad (12)$$

where, in our two cases,

$$\varepsilon_0 = \begin{pmatrix} 1 \\ 0 \end{pmatrix} \text{ or } \begin{pmatrix} 1 \\ \exp [-2ik_N(z_{N+1}-z_N)] \end{pmatrix}. \quad (12)$$

Using the inverse relation to Eq. (9):

$$\psi_n = C_n^{-1} \psi_{n+1}, \quad (13)$$

we can write

$$\psi_{N-1} = A_N C_{N-1}^{-1} \varepsilon_0. \quad (14)$$

Thus we may deduce by repeated application of Eq. (13)

$$\psi_1 = A_N C_1^{-1} C_2^{-1} \dots C_{N-1}^{-1} \varepsilon_0 = \begin{pmatrix} A_1 \\ B_1 \end{pmatrix}. \quad (15)$$

It is convenient to define the 2×2 matrix ζ_n according to

$$\zeta_n = C_n C_{n-1} C_{n-2} \dots C_1; \quad (16)$$

thus

$$\psi_1 = \begin{pmatrix} A_1 \\ B_1 \end{pmatrix} = A_N \zeta_{N-1}^{-1} \varepsilon_0. \quad (17)$$

The vector $\zeta_{N-1}^{-1} \varepsilon_0$ can be written in terms of two parameters $C_A(k_x)$ and $C_B(k_x)$ according to

$$\zeta_{N-1}^{-1} \varepsilon_0 \equiv \begin{pmatrix} C_A \\ C_B \end{pmatrix}. \quad (18)$$

Now our lower boundary condition says that

$$A_1 + B_1 = \zeta_{k_x} \quad (19)$$

where ζ_{k_x} is the fourier component of the surface displacement.

Thus

$$A_N = \frac{\zeta_{k_x}}{C_A + C_B} \quad (20)$$

Denoting the diagonal function matrix F_n as

$$F_n = \begin{pmatrix} e^{ik_n(z-z_n)} & 0 \\ 0 & e^{-ik_n(z-z_n)} \end{pmatrix} \quad (21)$$

we can write the solution (for the k_x component) in the form

$$\phi_{k_x} = \frac{\zeta_{k_x}}{C_A + C_B} \zeta_{n-1} \zeta_{N-1}^{-1} \epsilon_0 F_n e^{ik_n x} \quad (22)$$

and thus the general solution in the form

$$\phi(z, x) = \int_{-\infty}^{\infty} \frac{\zeta_{k_x}}{C_A + C_B} \zeta_{n-1} \zeta_{N-1}^{-1} \epsilon_0 F_n e^{ik_x x} \frac{dk_x}{\sqrt{2\pi}} \quad (23)$$

Here C_A , C_B , ζ_{k_x} , ζ and F_n all depend on k_x .

Resonant modes (those waves that can propagate far from the region of the disturbance: lee waves) are those free modes for which the integrand has poles. These will

correspond to the zeros of the factor $(C_A + C_B)$ along the real axis (these zeros will always occur in pairs at $\pm k_{x_i}$) since κ involves only k_x^2 .

In order that the integral in Eq. (23) have a unique value, it is necessary to specify on which side of the various poles the integration path passes. This is easily determined by the following considerations. Suppose that we add a small but finite amount of viscous damping to the atmosphere. The poles will then be shifted off the real axis by a small amount $\gamma \left(k_{x_i} - (k_{x_i})_{\text{real}} + i\gamma \right)$ and the resonant contributions (corresponding to the residues of Eq. (23) will have an x dependence of the form

$$e^{-\gamma x + i(k_{x_i})_{\text{real}} x}$$

Viscous effects will result in positive values of γ . Thus, taking the limit of $\gamma \rightarrow 0$ (to the inviscid case), we find that the integration path in Eq. (23) passes below all the poles of the integrand on the real axis.

The direct numerical integration of Eq. (23) along the real axis is very difficult because of the presence of the poles, and it is convenient to use the theory of residues to obtain a more convenient path. Consider the integration paths shown in Figure 6. For $x > 0$ it is necessary to choose a path constrained to the upper half plane in order that convergent integrals result. Here we may write

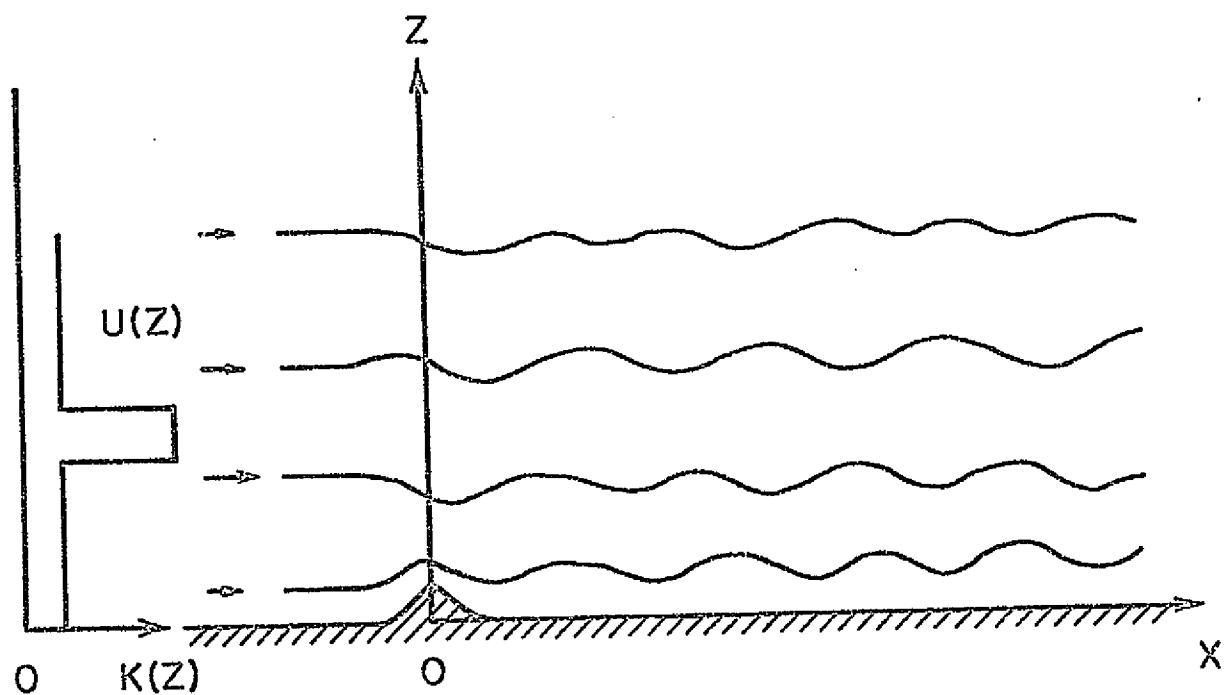


Figure 5. Physical Sketch of the Mountain Leewave

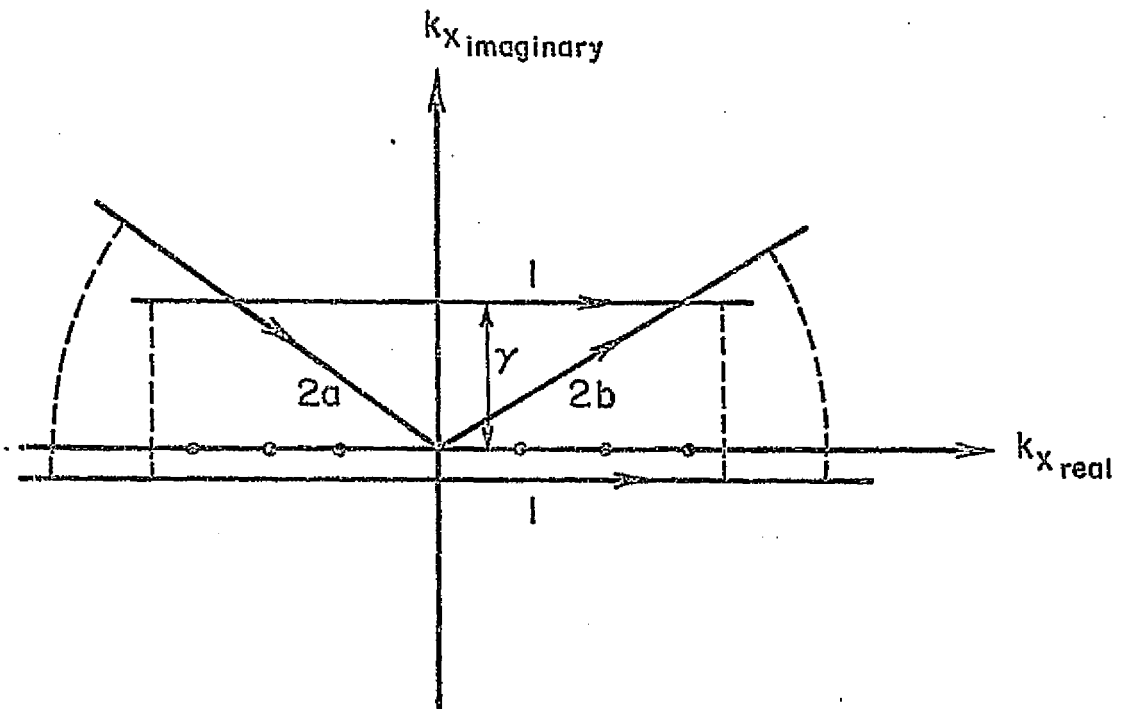


Figure 6a. Integration Contours for $x > 0$

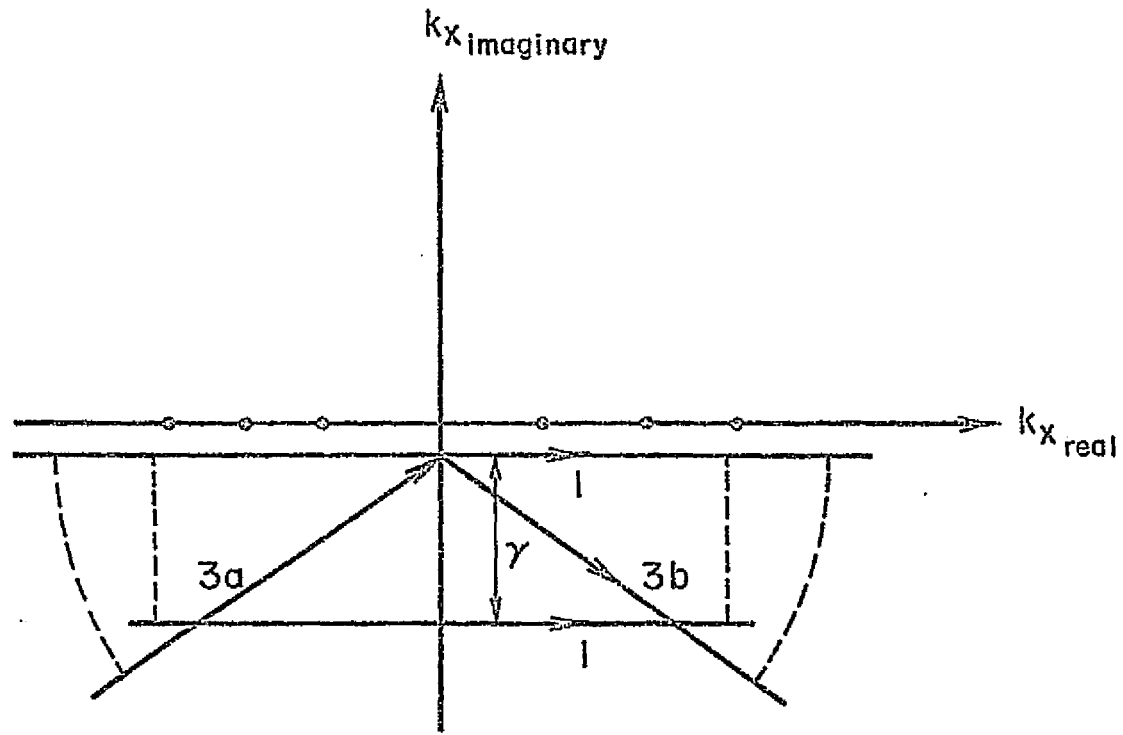


Figure 6b. Integration Contours for $x < 0$

$$\int_1 [] dk_x = \sum_{\text{poles}} (\text{residues}) + \int_2 [] dk_x \quad (24)$$

On the other hand, for $x < 0$, a path constrained to the lower half plane is appropriate. Here

$$\int_1 [] dk_x = \int_3 [] dk_x \quad (25)$$

The integrals over the paths 2 or 3 represent the non-resonant contributions to the wave motion. In general, they are symmetric with respect to the mountain and are significant only in the neighborhood of the disturbing boundary due to the factor $ik_x e^{ik_x x}$ in Eq. (23). On the other hand, the sum over residues give rise to the lee waves which can be significant well downstream of the boundary disturbance. Integration of the non-resonant contribution of Eq. (23) can further be simplified by using the fact that the integrands evaluated on the contours 2a (or 3a) and 2b (or 3b) are complex conjugates to each other, such that only half of the contours need to be taken, and the result is the real part of ($2 \times$ integrand of (23) $\times dk_x$) along contour 2b or 3b. The present choice of the contours greatly simplifies the integration of the non-resonant contribution without generating any artificial discontinuity at the mountain peak (Scorer, 1949) or requiring the cumbersome operations pursued by Vergeiner (1971) to remove the singularities.

3. Transformation to Physical Variables

The perturbed variables u' , w' , ρ' , p' , T' and θ' can be obtained by simple derivations from the continuity equation and the kinematic condition. Considering the flow confined in a stream tube which is formed by the streamlines $\phi(x, z)$ and $\phi(x, z + \Delta z)$ and knowing that the fluid is incompressible, we can show that the horizontal velocity is given by:

$$U\Delta z = (U+u') \left(\Delta z + \phi(z+\Delta z) - \phi(z) \right)$$

or

$$\frac{u'}{U} = - \frac{\frac{\partial \phi}{\partial z}}{1 + \frac{\partial \phi}{\partial z}}, \quad (26)$$

where Δz is the spacing between the same streamlines at $x = -\infty$. By kinematic condition, we have the relation for the vertical velocity

$$w' = U \frac{\partial \phi}{\partial x}. \quad (27)$$

Substituting these relations to the incompressibility condition,

$$U \frac{\partial \rho'}{\partial x} + w' \frac{dp}{dz} = 0$$

we have

$$\frac{\rho'}{\rho} = - \frac{1}{\rho} \frac{dp}{dz} \phi \quad (28)$$

Taking into account the adiabatic condition and the energy equation, we have

$$\frac{p'}{p} = - \frac{1}{p} \frac{dp}{dz} \phi \quad (29)$$

and using the ideal gas law we will have

$$\frac{T'}{T} = \left(\frac{gp}{p} + \frac{1}{\rho} \frac{dp}{dz} \right) \phi = - \frac{1}{T} \frac{\partial T}{\partial z} \phi \quad (30)$$

or

$$\frac{\theta'}{\theta} = \left(\frac{gp}{\gamma p} + \frac{1}{\rho} \frac{dp}{dz} \right) \phi = - \frac{1}{\theta} \frac{\partial \theta}{\partial z} \phi \quad (31)$$

From Eqs. (26) through (31), one can then derive the local Richardson number. By assuming that the flow will become turbulent when it is unstable ($R_i < \frac{1}{4}$) and that irregularities will continue to exist until the local Richardson number increases to 1, we can locate regions in which we expect CAT to exist in the lee of the mountain. The Richardson number describes conditions under which the flow becomes unstable, and indicates where turbulence is likely, but it does not allow estimates to be made of such important turbulence characteristics as the magnitude of the velocity fluctuations and their length scales. This information would have to be extracted by other means and will be discussed elsewhere.

C. Results and Discussion

These investigations are divided into two parts: a three-layer test case, and two seven-layer cases chosen to represent observations. The first part was undertaken to prove the convergence of the present linear analysis, to reveal the effects of the different boundary conditions applied on the top, and to test the present computer code.

In the limit as the thickness Δz_2 of the middle layer approaches zero, with the product of thickness and Scorer's parameter $K_2^2 \Delta z_2$ being constant, the resonant wavenumber found by the present numerical scheme converges to that given by the relation derived in Appendix III. The close agreement between numerical and analytical results gives us confidence that this code is working properly.

Boundary conditions for this problem are not uniquely defined. Solutions to Eq. (1) are presented in Figures 8 and 9, with the input vertical profiles of the mean wind and the potential temperature shown in Figure 7. Figure 8 shows the displacement profiles when the solid wall condition is applied on the top boundary; a purely real resonant mode corresponding to wavelength $\lambda = 118.5$ km was found and the wave amplitude is about 1.5 km. Figure 9 gives the result when the evanescent condition is applied; one resonant wavenumber was obtained with a small imaginary part, and the wavelength is 68.87 km. The smaller wave amplitude in the

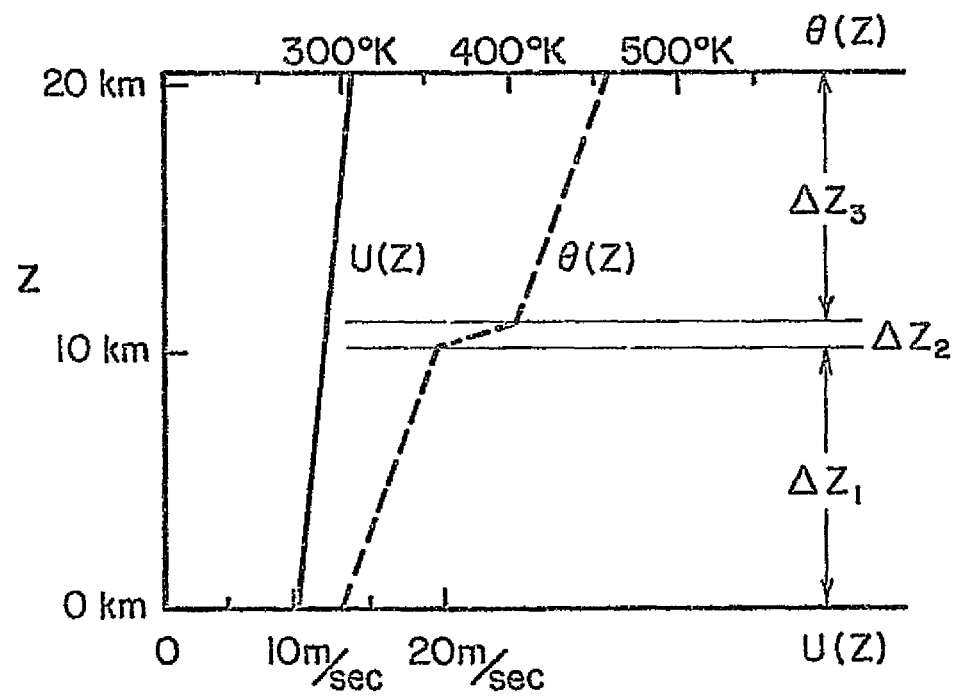


Figure 7. The Vertical Profiles of the Mean Wind and the Potential Temperature

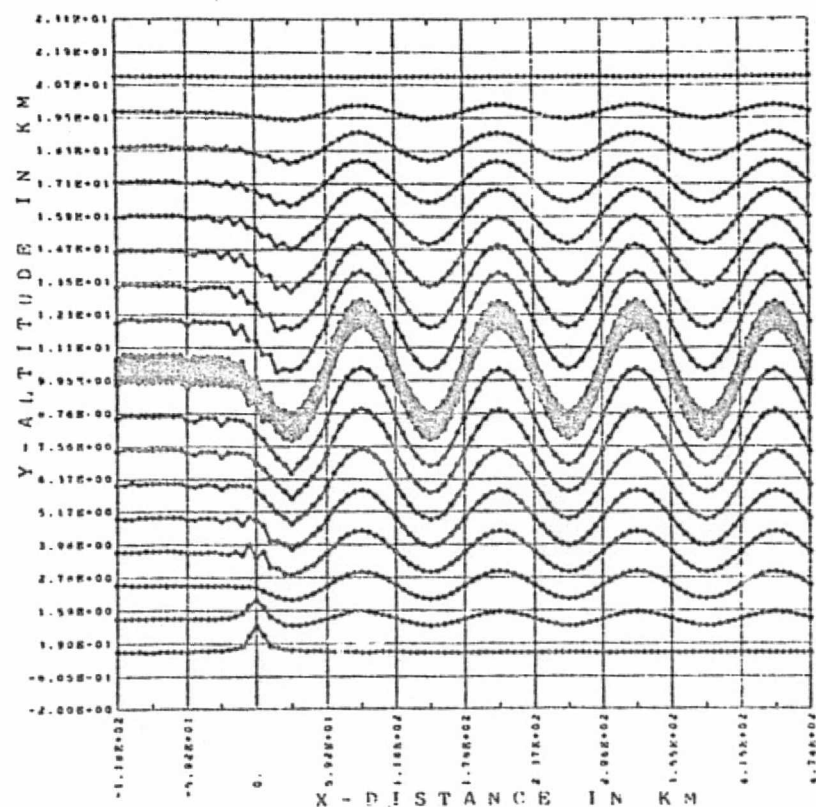


Figure 8 . Lee Wave Profiles for the Three-layer Case
with Solid Wall Upper Boundary Condition

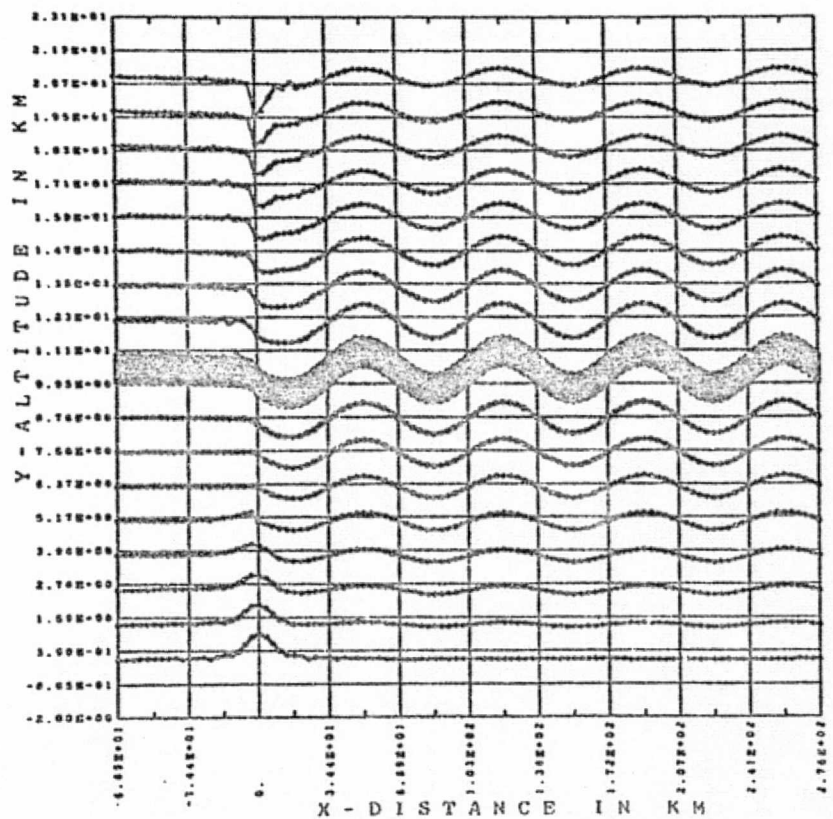


Figure 9. Lee Wave Profiles for the Three-layer Case
with Evanescent Upper Boundary Condition

middle layer in Figure 9 indicates the effect of energy leaking through the upper boundary, i.e., the waves are not completely ducted. The continual radiation of energy upwards results in the decreasing of wave amplitudes downstream even without friction, in contrast to the case of a rigid upper lid where the energy is reflected back and remains in the flow. Notice that in both cases the lower boundary condition is satisfied.

Neither of these two upper boundary conditions is exact. Evidence exists that the upper atmosphere extracts energy from the lower troposphere (this corresponds to the evanescent case). On the other hand the solid wall case may approximate the critical level. The existence of a more realistic upper boundary condition for the linear formulation is still in doubt. One may avoid the difficulty by extending the top boundary to infinity, but then the flow cannot be treated from the adiabatic and the linearized point of view, nor does there exist any obvious physical boundary upon which the above conditions apply. Nevertheless, the critical level formulation by Booker and Bretherton (1967a) represents a realistic upper boundary condition and this is approximated by the solid wall condition. One should notice, however, as will be shown below, the solutions obtained by applying either the solid

wall or the evanescent upper boundary condition are in many cases nearly indistinguishable. As long as the wave amplitude is small, which boundary condition applies is not a critical question.

The second part of this investigation deals with a number of real cases. The vertical profiles of the mean wind and the potential temperatures are shown in Figure 10a and 11a, which approximates the data obtained by Lilly (1971) on February 13, 1970, along the cross section between the Kremmling and Colorado VOR stations, and on February 15, 1968, near the continental divide given by Lilly and Toutenhoofd (1969). In contrast to the $K(z)$ profiles used in the first part of the computation, the $K(z)$ profiles for these cases, as shown in Figure 10b and 11b have a minimum in the middle layer. The air is less stable close to the ground and is increasingly stable upwards such that one can expect that most of the CAT should occur beneath the stratosphere.

It is generally found to be true that the strong wind shear and stable layers are the two factors conducive to gravity wave formation. To manifest this, the chosen two cases for which lee wave activities were observed are especially interesting. Actual computation for both cases was difficult, as it turned out, due to their extreme properties.

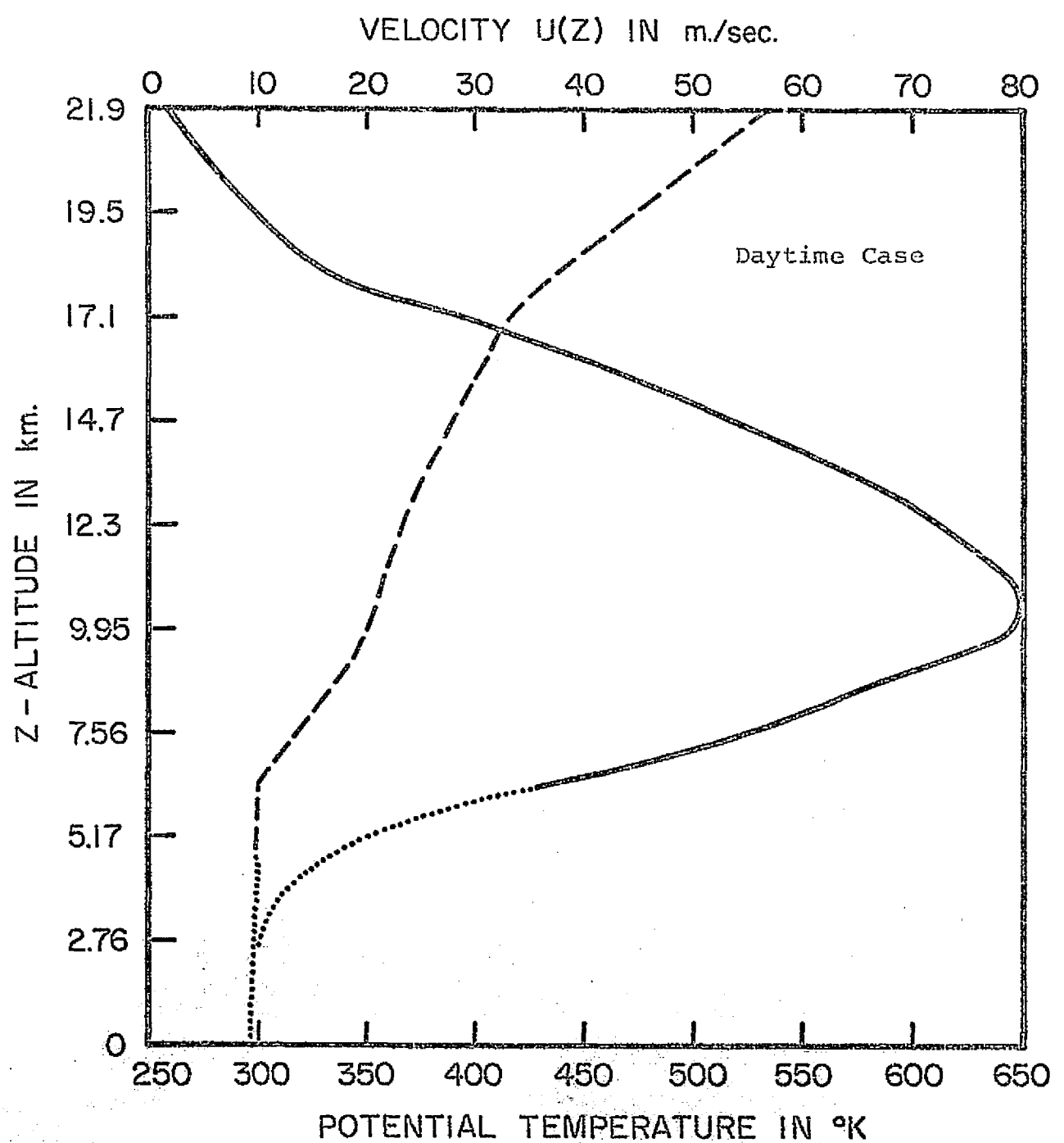


Figure 10a. Potential Temperature and Wind Profiles on February 18, 1970, between Kremmling and Colorado VOR Stations

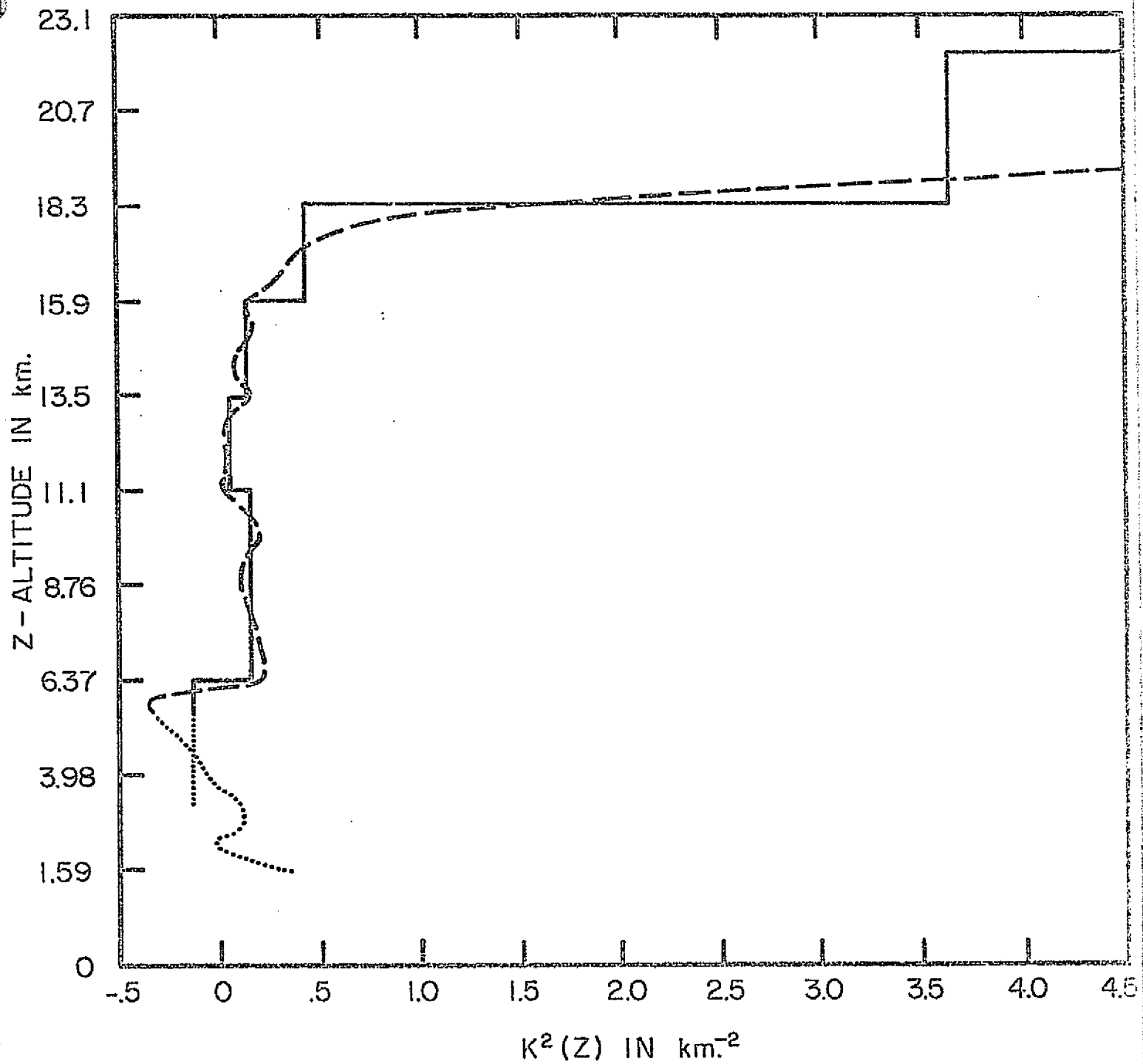


Figure 10b. Scorer's Parameter for Meteorological Data on February 18, 1970, between Kremmling and Colorado VOR Stations

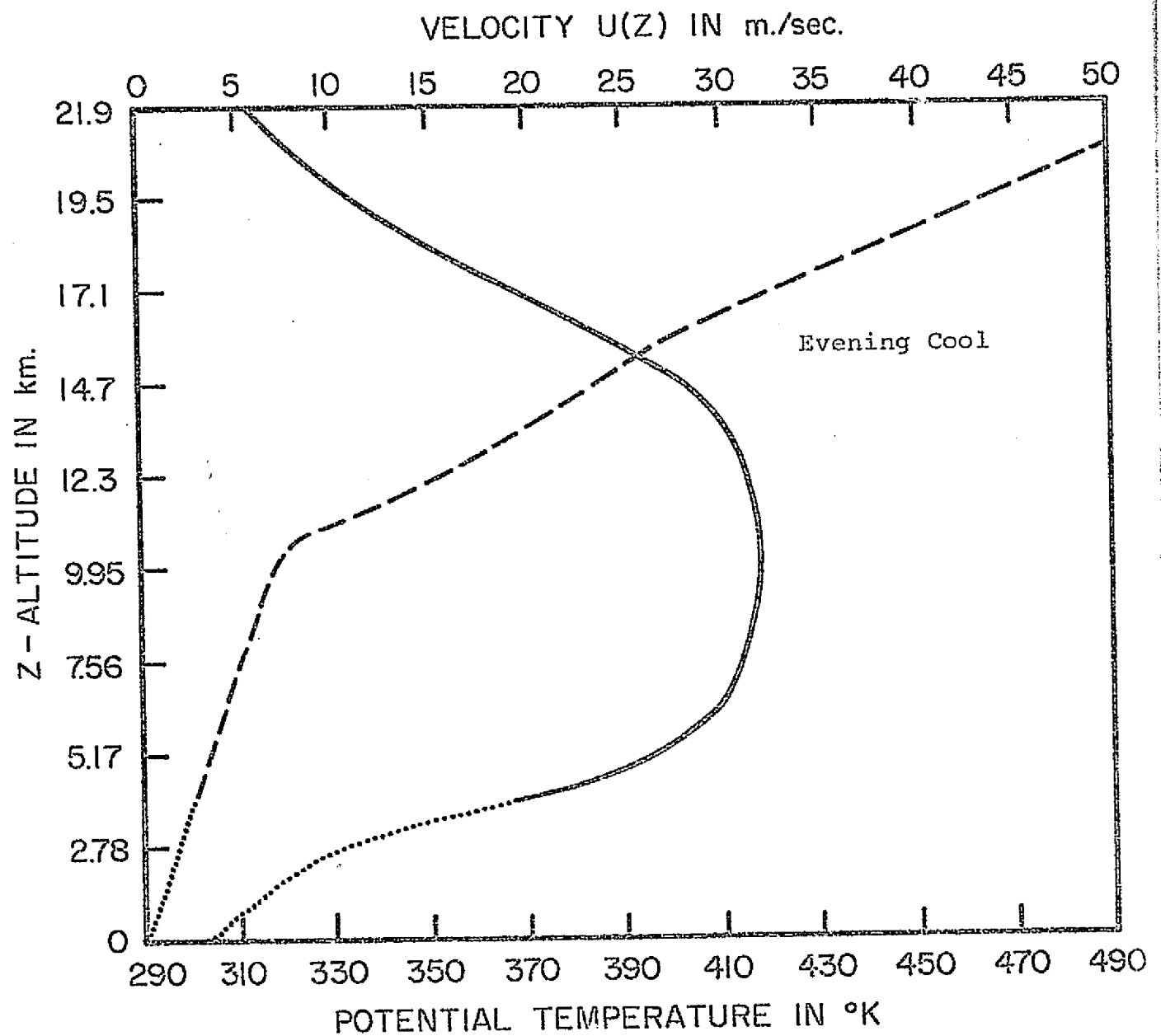


Figure 11a. Potential Temperatures and Wind Profiles on February 15, 1968, near the Continental Divide

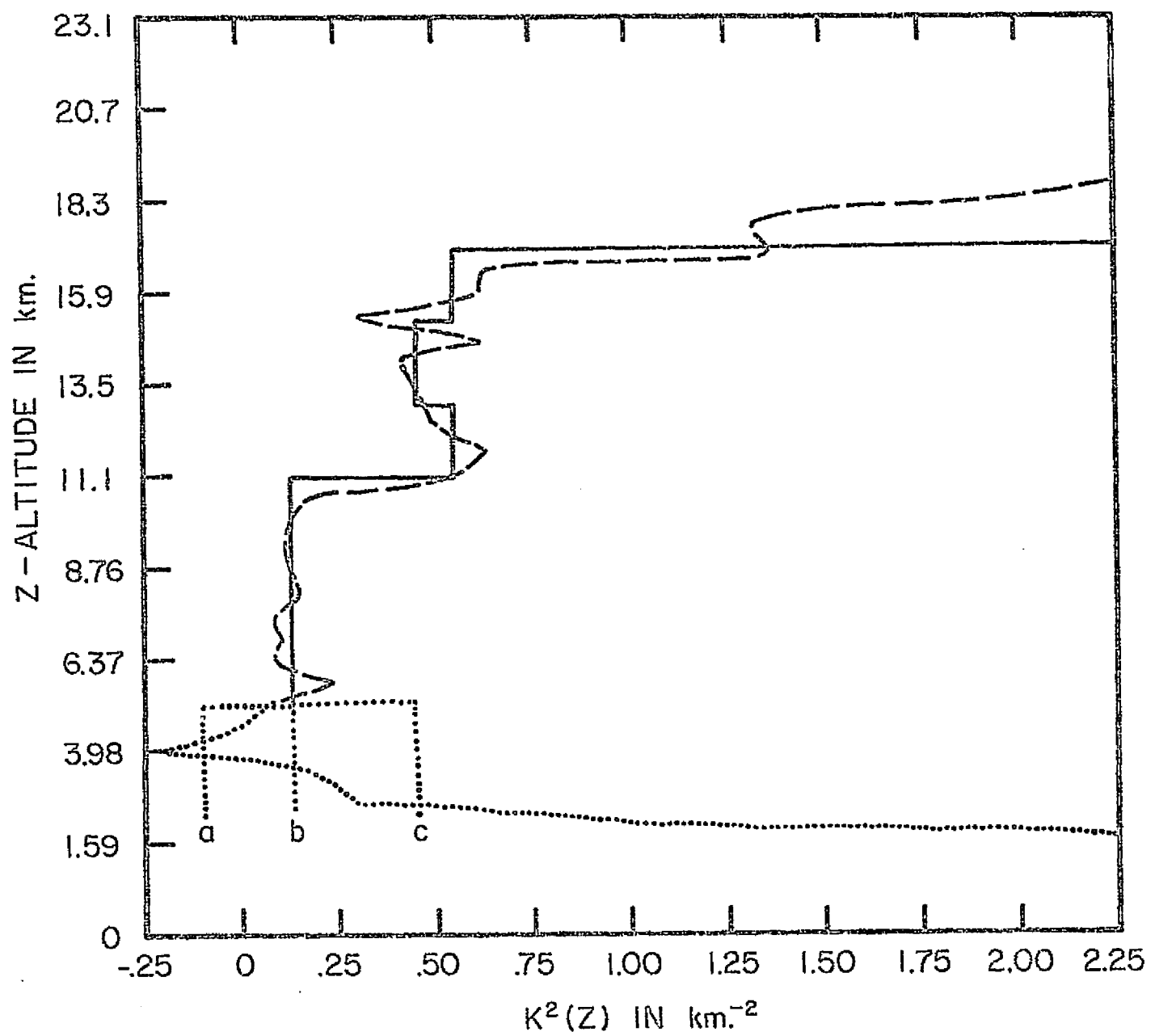


Figure 11b. Scorer's Parameters for the Meteorological Data on February 15, 1968, near the Continental Divide

In one case the Scorer parameter $K^2(z)$ in the ground layer was large and in another it becomes negative. The first case occurs when the ground layer is very stable and the wind shear is not strong; this usually occurs in the evening (the February 15, 1968, case) such that the flow is blocked upstream of the mountain, as was observed by Lilly and Toutenhoofd (1969). In this blocked area the perturbed horizontal velocity must be comparable to the mean flow in order to produce a stagnation point; in consequence, the small perturbation assumption breaks down. Another way of looking at this phenomenon is that blocking occurs when the gravity wave fronts are vertical; i.e., the disturbance will propagate to upstream infinity and hence contradicts the definition of the mean flow condition. Unless a priori information is obtained about the blocked profile, a detailed solution in this region cannot be expected from the linear theory. The second case corresponds to a nearly neutral stable ground layer with strong wind shear; this usually appears in the daytime profiles (for example, the February 18, 1970, case) so that the flow can easily be churned into vortex motion.

To avoid dealing with imaginary $K(z)$ values, which upon substitution into Eq. (7) will lead to exponential solutions, Foldvik (1962), Conover (1964) and Lovill (1969) simply dropped the second shear term in Eq. (2). Similarly,

Danielsen and Bleck (1970) applied heavy smoothing to the $K^2(z)$ profile, and Vergeiner (1971) also applied discontinuous shear profiles. However, this shear term affects the vertical convection of the horizontal mean momentum and the horizontal convection of vertical perturbation momentum, and should be included in evaluating the flow. (A physical argument could be advanced to remove this difficulty, but was not applied in the present study: It is well known from Rayleigh's criterion for an inviscid unstratified flow that a flow with a point of inflection in its velocity profile is unstable; it can be shown that this criteria still holds for the stratified flow. For the wind profiles in Figure 10 for February 18, 1970, there are two points of inflection, turbulence must exist to reduce the wind shear and restore the flow stability. Without dealing with a nonlinear problem, one could be content with the assumption that the flow there should be well mixed so that no gradients exist in either velocity or in the potential temperature profiles. Therefore, one could assign a small positive value to $K^2(z)$ wherever it is negative, and the solution would not be found to be sensitive to the assumed value, as was shown in the first set of computations.)

Difficulties were encountered due to the lack of information in the ground layer, represented by the dotted region in Figs. 10a and 11a, from 3 to 5 km above sea level, even with the best available meteorological data. Unfortunately, the

leewave solution depends critically upon the input mean flow, the wind shear profile in particular. To demonstrate this, Figure 11b shows the three possible $K^2(z)$ profiles near the ground for the February 15, 1968, case; the real profile could be anywhere between them. The results are shown in Figure 12. In cases a and b there is little wave action, while case c produces a leewave pattern with some similarity to the experimental data given by Lilly and Toutenhoofd (1969). The resonant wave numbers are tabulated in the following table.

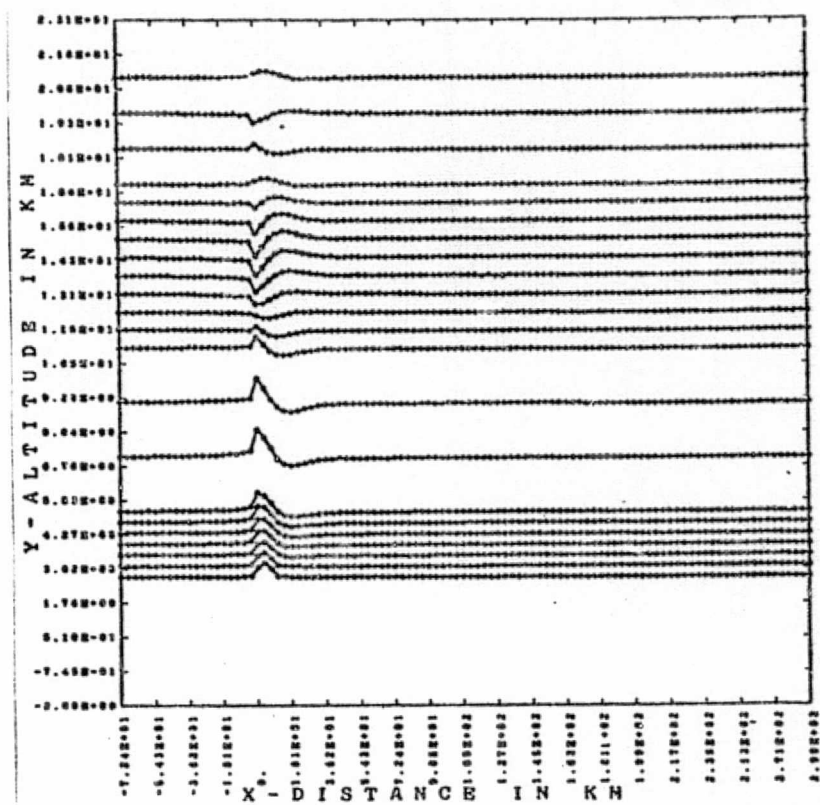
resonant wave numbers	Case		
	a	b	c
1) Real	.1315699	.14943	.228069
Imaginary	.1132932	.081939	.028817
2) Real	.573351	.573387	.573475
Imaginary	.0213953	.021373	.0213169

The second resonant wave number does not vary significantly as it is not controlled by the ground layer property. It is

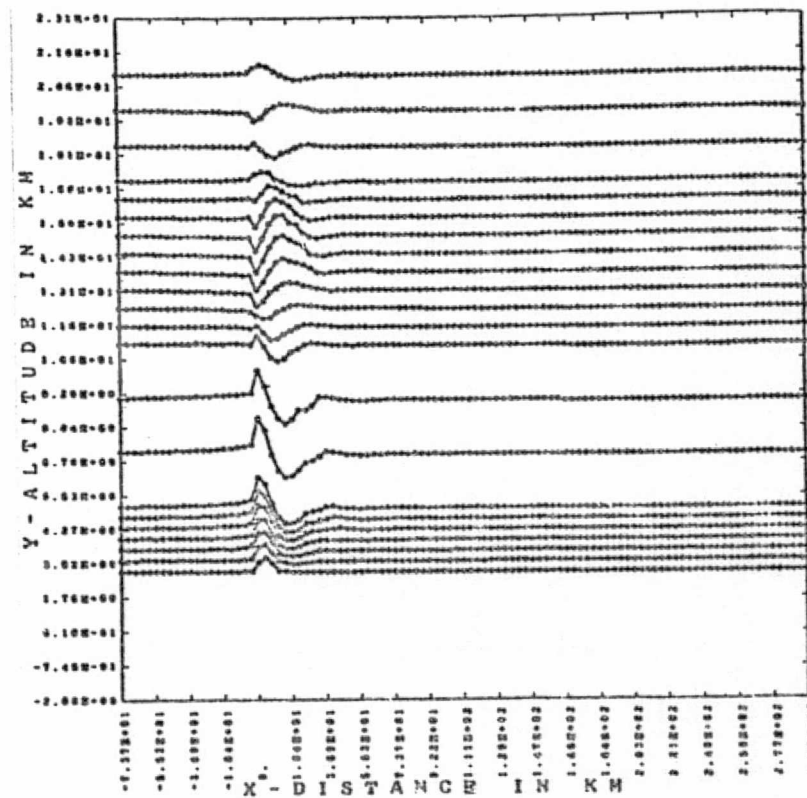
interesting to see that as the ground $K^2(z)$ value gradually increases from negative values, the imaginary part of the first resonant wavenumber gradually decreases. Figure 12a shows rapid decay downstream and increasingly visible wave activities in Figures 12b and 12c.

Both cases investigated were really pathological cases for the linear theory. However, one can still get realistic results if one is willing to give up the flow details in the ground layer. Linear adiabatic theory is not valid near the ground due to the existence of the turbulent Ekman planetary boundary layer, blocking, and non-isentropic processes such as viscous damping and heat transfer. Here we only attempted to preserve information far from the disturbances without invoking trial and error methods for fitting the blocked profile or applying nonlinear boundary conditions.

The Scorer's parameter $k^2(z)$ determined from the dotted profiles in Figure 11a near ground is also shown in dotted lines in Figure 11b. It is difficult to assign an arbitrary constant value for $k^2(z)$ in the ground layer, since it varies from 2.25 to -.25 over a height of only 2 km. However, if we take the same case and ignore the small scale structures (variations over dimensions less than 1 km) and recalculate the $k^2(z)$, we obtain the dashed

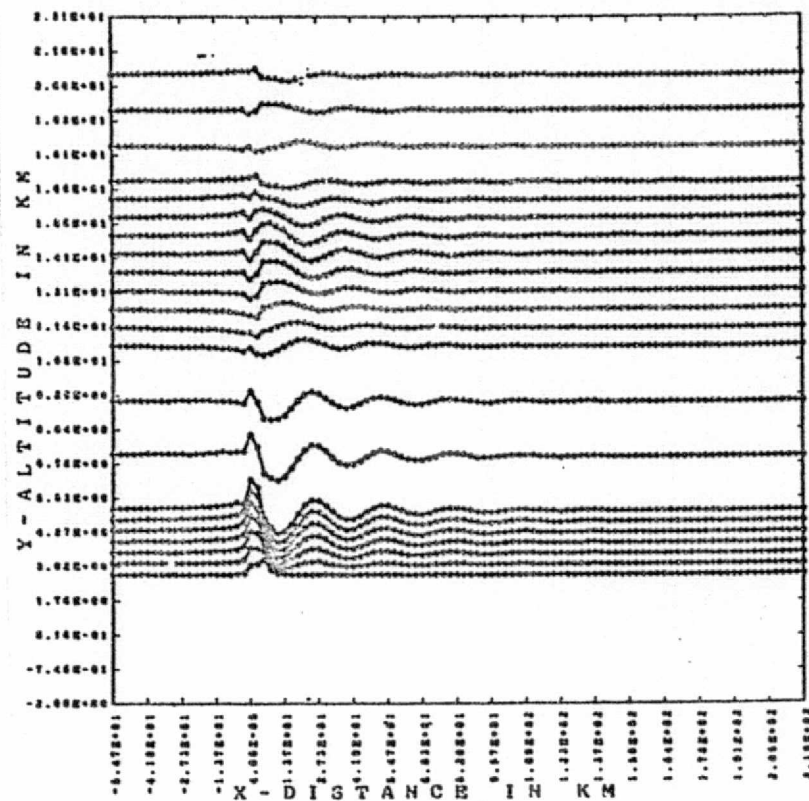


a



b

Figure 12. Sensitivity of Flow Solution Upon the Lower Portion of Meteorological Data



C

Figure 12. Sensitivity of Flow Solution Upon the Lower Portion of Meteorological Data

lines in Figure 13. The solid line in Figure 13 represents the approximate profile actually applied in the calculation. The results are shown in Figure 14 through Figure 16. Figure 14 shows the streamline pattern where lee wave motions are apparent; all scales are in km. Hatched areas represent the cross-section of topography over the continental divide. A velocity vector plot is shown in Figure 15, where strong up-and-down motion over the mountains can be seen. Figure 16 shows the distribution of Richardson's number. The dots represent unstable regions (where $R_i < 1/4$) and stars show where regions are marginally unstable. ($1/4 < R_i < 1$) Unstable and marginally stable regions can be identified as those where CAT is likely to be found.

In Figure 16, several horizontal lines at different altitudes and three lines at angles of 6.6° , 45° and 171.5° are drawn to simulate the lines-of-sight for an LDV system. Along each line-of-sight, the parallel velocity, its gradient along the line-of-sight, potential temperature and its gradient and Richardson number can be calculated. A series of these plots are given in Figure 17 for $\theta=45^\circ$, where θ is the elevation angle. From these types of plots, Table III was compiled for different lines-of-sight. On these data we will establish, in Section IV, the basic requirements on range resolution, integration time, and maximum detectable range for a possible LDV system.

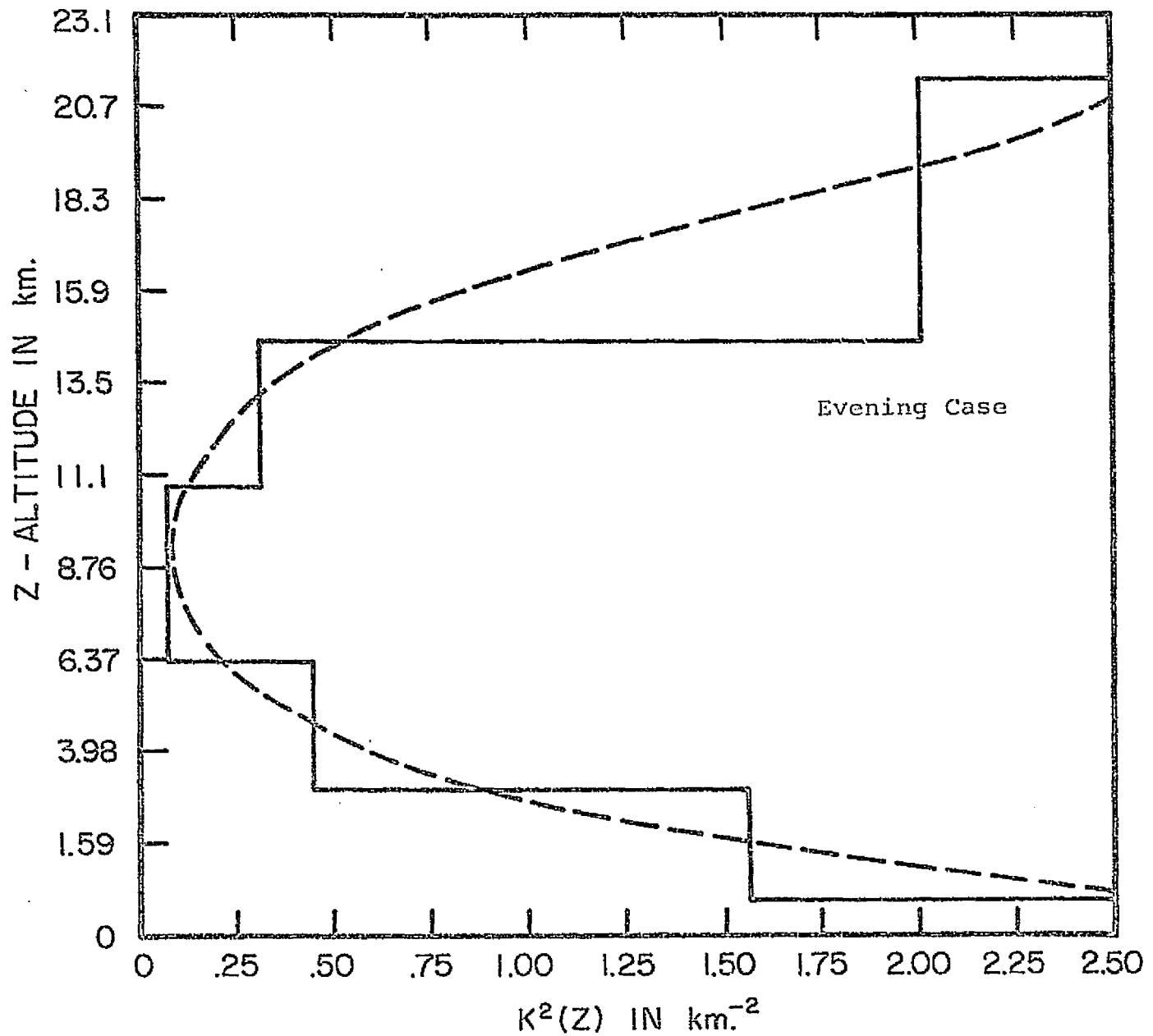


Figure 13. $K^2(z)$ for the Meteorological Data on February 15, 1968, over the Continental Divide

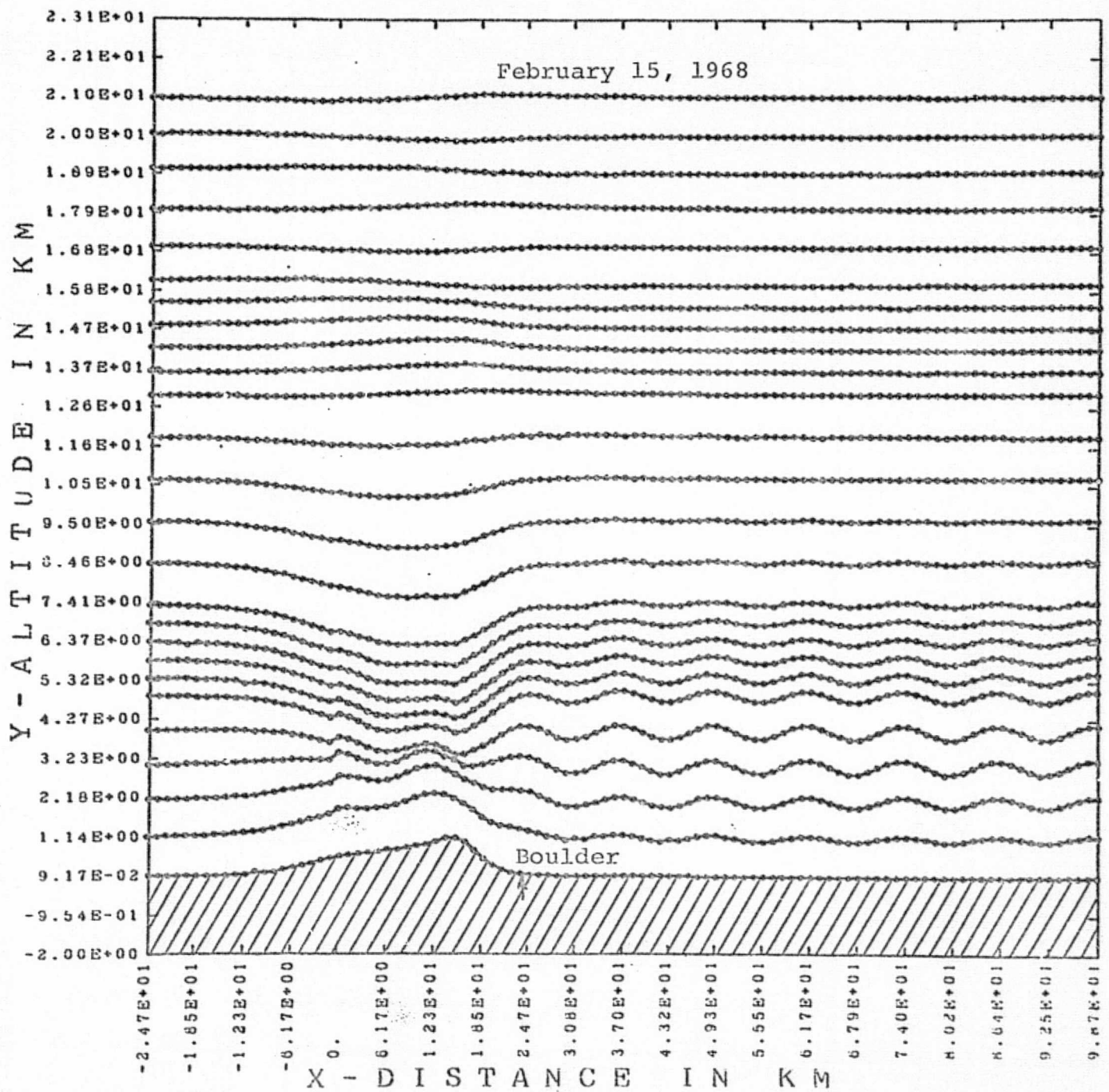


Figure 14. Streamline Patterns

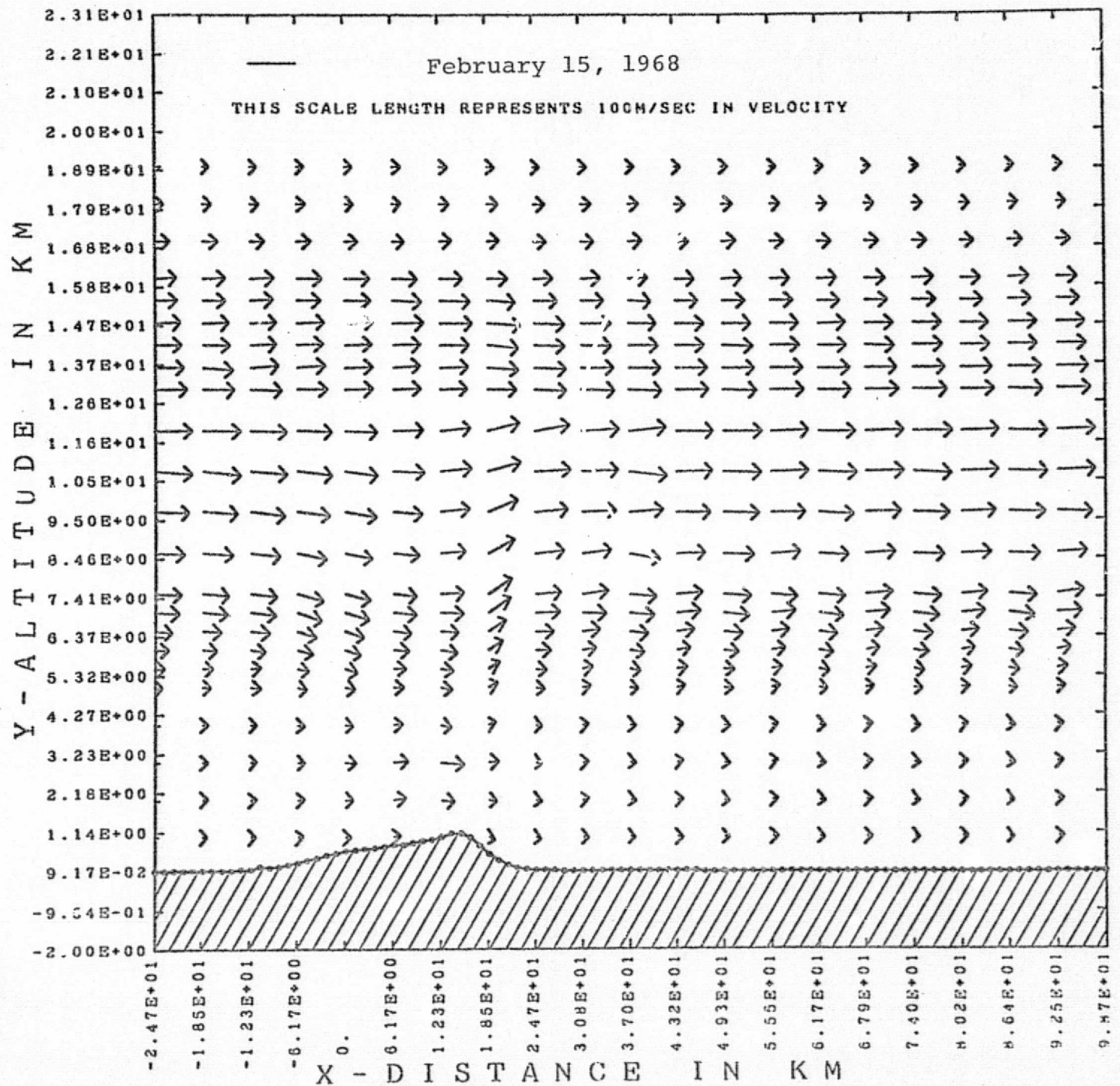


Figure 15. Velocity Vector Plot

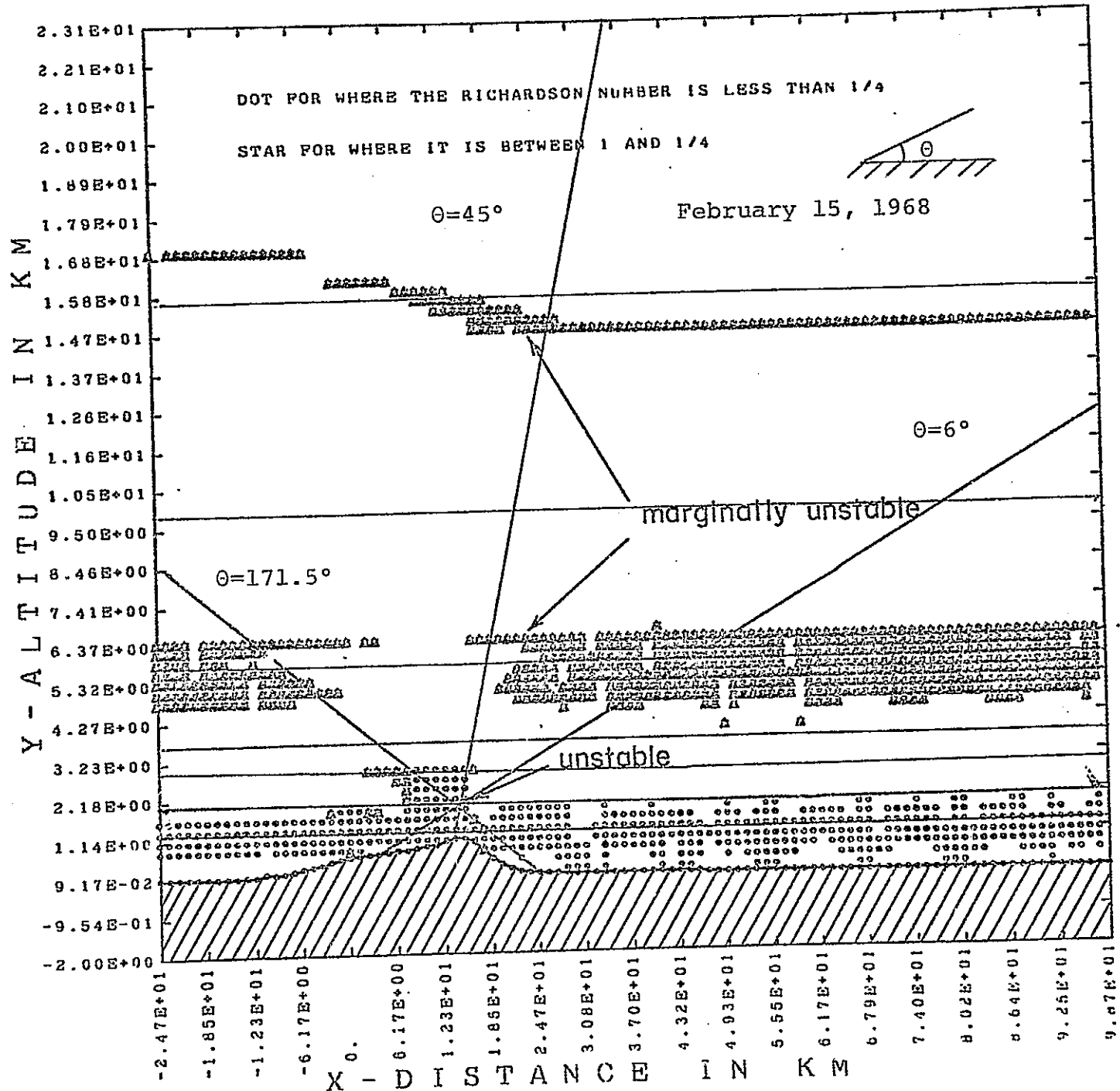


Figure 16. Distribution of Richardson Number
 (Note difference in vertical and horizontal scales)

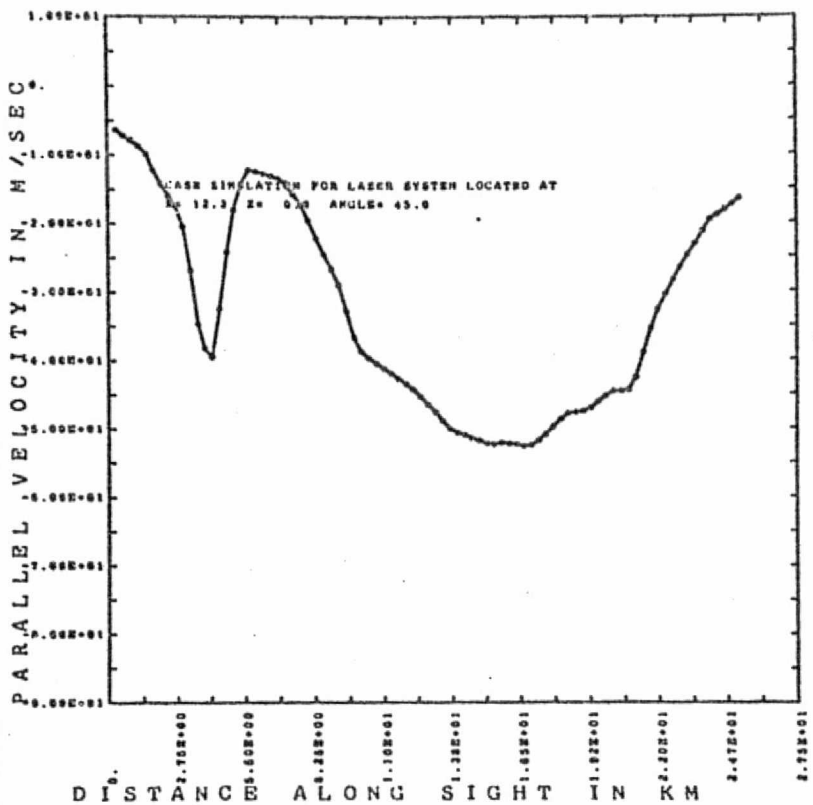


Figure 17a. Parallel velocity along line-of-sight

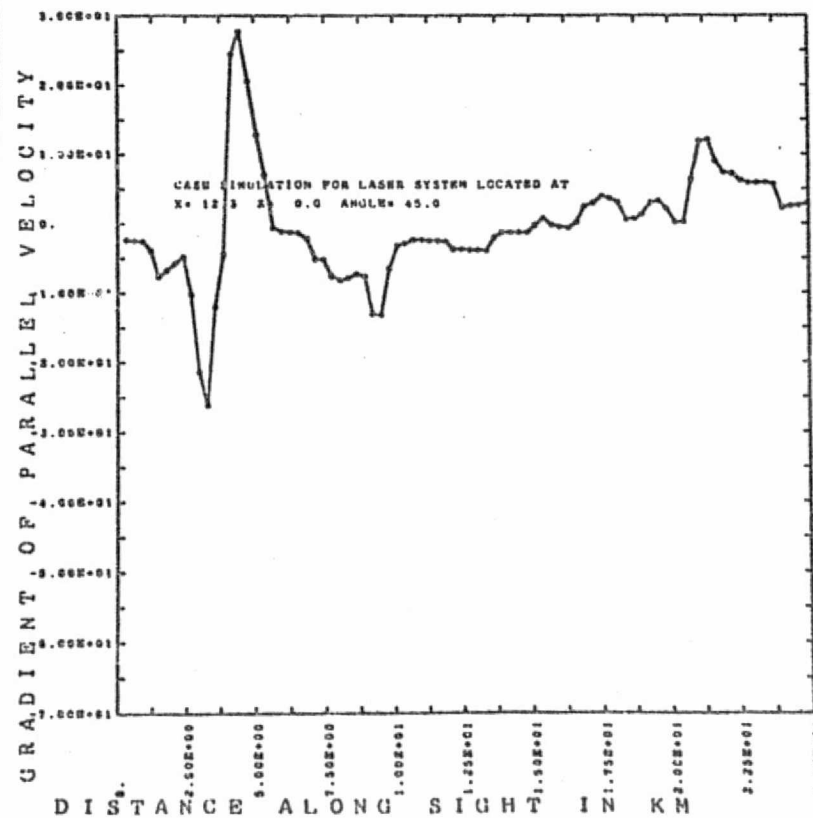


Figure 17b. Gradient of parallel velocity along line-of-sight

Figure 17. Typical inputs for LDV Sensor Response Simulation.

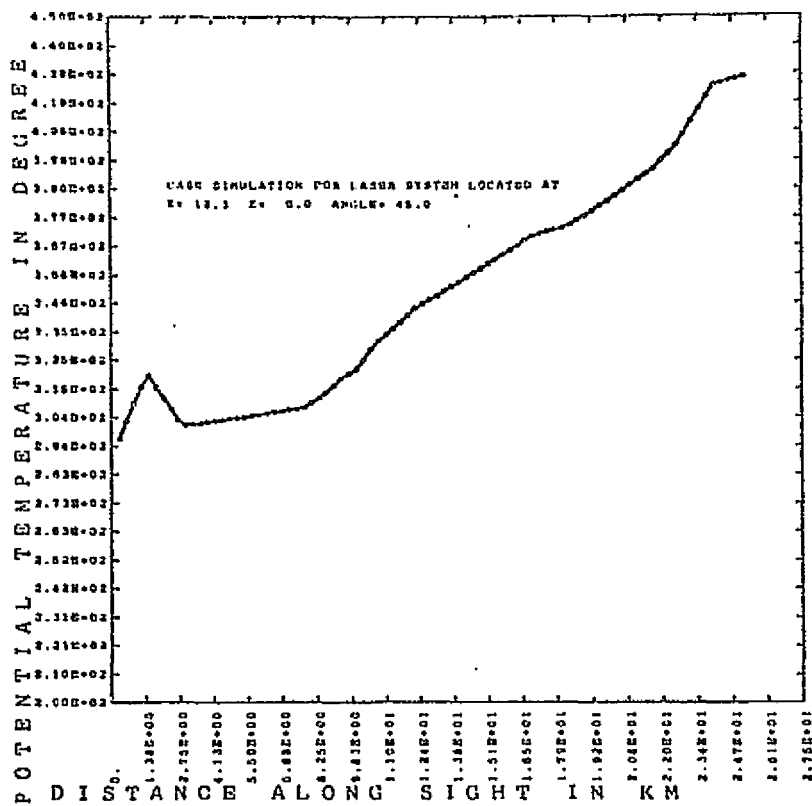


Figure 17c. Potential temperature along line-of-sight

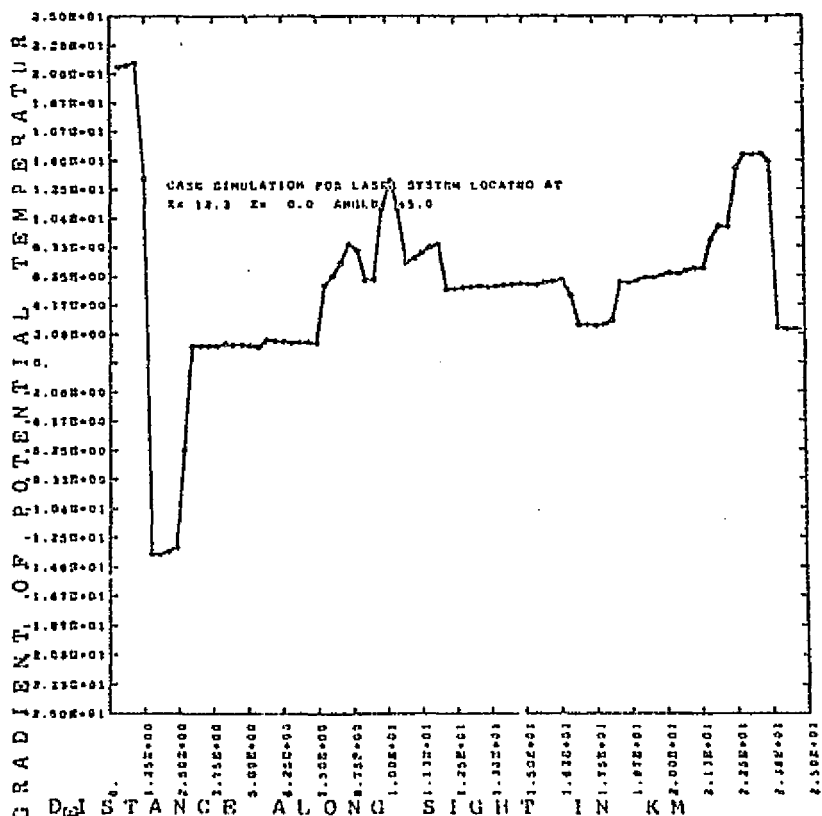


Figure 17d. Gradient of potential temperature along line-of-sight

Figure 17. Typical Inputs for LDV Sensor Response Simulation.

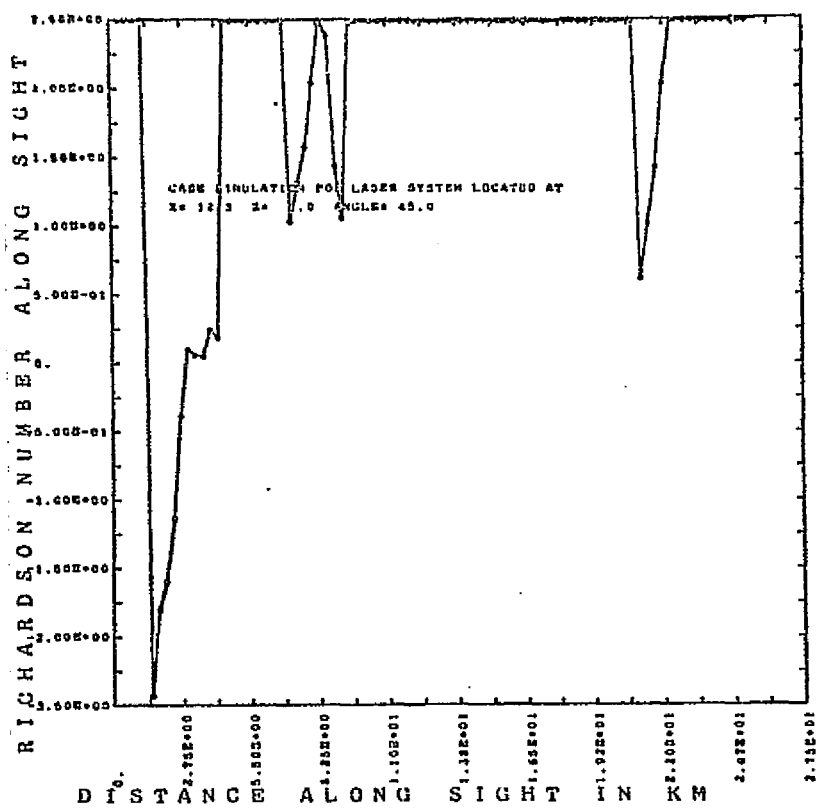


Figure 17e. Richardson number along line-of-sight

Figure 17. Typical Inputs for LDV Sensor Response Simulation.

θ	Altitude	Maximum $\partial v_{ } / \partial r$	Range at Maximum	Range Resolution Required	Maximum $\Delta v_{ }$ m/sec
Aircraft Platform	0° 3.7 km	12×10^{-3}		8.5 km	20
	0° 5.7 km	1×10^{-3}		8.5 km	5
	0° 9.7 km	2.5×10^{-3}		8.5 km	1.2
Ground Platform	6.6° ground	4×10^{-3}	17 km	4.25 km	20
	45° ground	30×10^{-3}	4 km	1.3 km	40

Table III. Compilation of Atmospheric Wind Data

The temporal variation of wind velocity cannot be obtained from the lee-wave model, but a rough estimate can be made here. Two time scales are relevant here: a long time scale associated with the wave motion in a stratified medium $\left(\frac{g}{\rho} \frac{\partial \rho}{\partial y}\right)^{-1/2}$ and a short time scale for dissipation of small eddies $\sqrt{v/\epsilon}$, where v is kinematic viscosity and ϵ is the dissipation rate. The former is in the order of several tens of minutes, while the latter is in the order of .01 second. Any time scales between those two extremes are possible and are associated with medium size eddies.

IV. ASSESSMENTS OF CURRENT SYSTEMS

For a pulsed system, we have constructed Table IV from the results in Section III. This table relates pulse length to vertical range resolution, ΔV_{pulse} and peak $\Delta V_{||}$ for several elevation angles.

Elevation Angle	Pulse Duration τ	Pulse Length $C\tau/2$	Vertical Resolution	$\Delta V_{pulse} = \lambda/2\tau$	Peak $\Delta V_{ } = \max \left(\frac{\partial V}{\partial R} \right) \cdot \frac{C\tau}{2}$
$\theta = 0^\circ$	$6.7\mu \text{ sec}$	1000 m	0	.79 m/sec	$\sim 4 \text{ m/sec}$
	$2.2\mu \text{ sec}$	330 m	0	2.4 m/sec	$\sim 1.3 \text{ m/sec}$
$\theta = 7^\circ$	$6.7\mu \text{ sec}$	1000 m	114 m	.79 m/sec	$\sim 4 \text{ m/sec}$
	$2.2\mu \text{ sec}$	330 m	38 m	2.4 m/sec	$\sim 1.3 \text{ m/sec}$
$\theta = 45^\circ$	$6.7\mu \text{ sec}$	1000 m	707 m	.79 m/sec	$\sim 27 \text{ m/sec}$
	$2.2\mu \text{ sec}$	330 m	230 m	2.4 m/sec	$\sim 9 \text{ m/sec}$

Table IV. Characteristics of a Pulsed System at Various Elevation Angles

At lower angles $\theta = 0^\circ, 7^\circ$, higher range resolution can be achieved; however, at low angles, it takes longer ranges to probe higher altitude wind information. At $\theta = 45^\circ$, the range resolution is poor but higher wind variation exists along the line-of-sight.

To assess the measurability of turbulence level by a pulsed system, it is important to compare the root mean square turbulence fluctuation expected in CAT to ΔV_{pulse} .

From the available data collected by Vinnichenko, et al. (1903), we have plotted V_{rms} versus pulse time in Figure 18. The V_{rms} is obtained by

$$V_{rms} = \sqrt{\frac{3}{2} C \frac{\epsilon}{k}}^{2/3}$$

and $k = ct$, $C = 1.375$. Four levels of turbulence are given, each corresponding to a different dissipation rate which is directly related to the severity of CAT experienced by commercial aircraft pilots. $\Delta V_{pulse} = \frac{\lambda}{2\tau}$ is also shown in Figure 18. It defines turbulence levels measurable for each pulse time. For example, the 2μ second pulse system cannot measure turbulence below moderate levels.

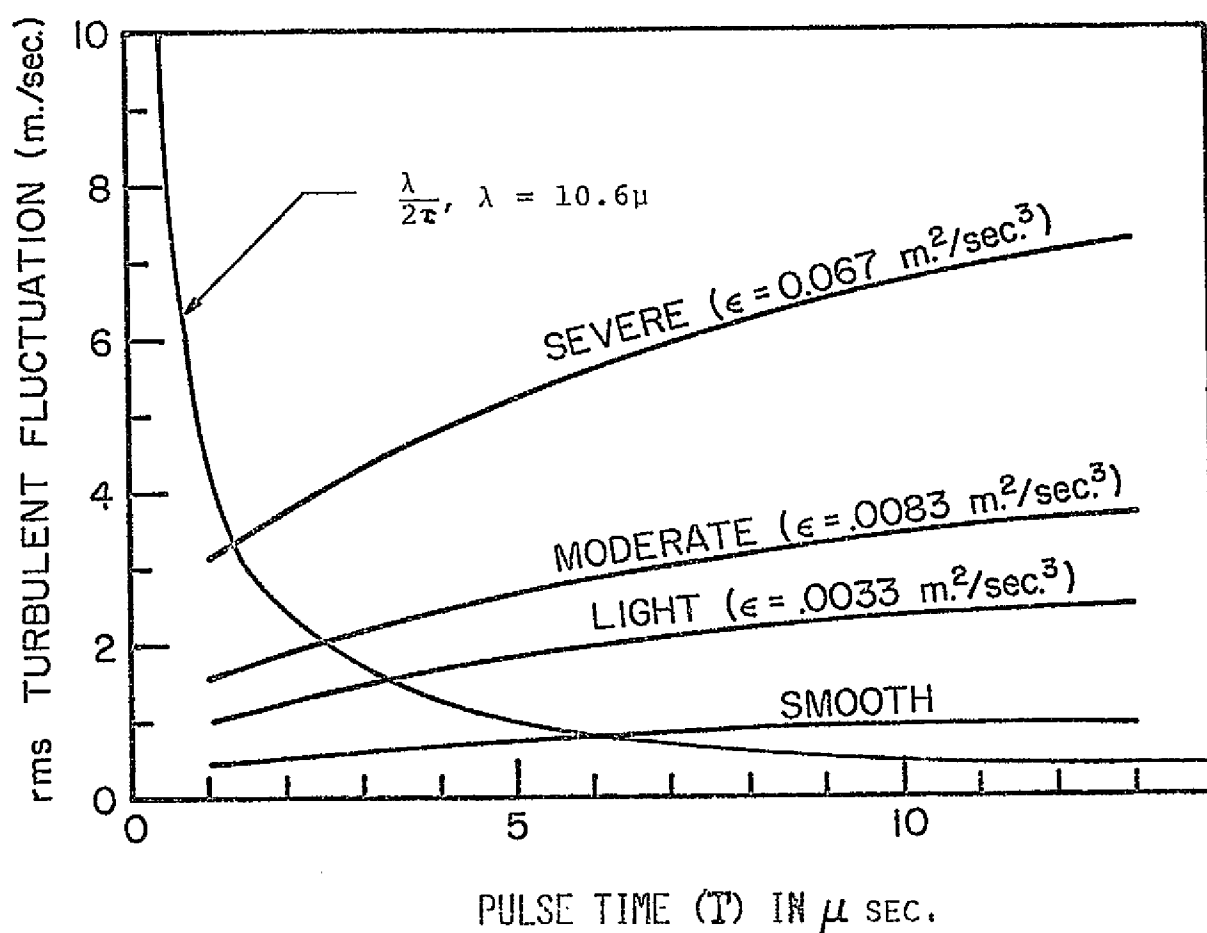


Figure 18. V_{rms} and ΔV_{pulse} versus Pulse Time

REFERENCES

- Hazel, P., "The Effect of Viscosity and Heat Conduction on Internal Gravity Waves at a Critical Level"
J. Fluid Mech., 30, pp. 529-554, 1967
- Booker, J. R. and Bretherton, F. P., "The Critical Layer for Internal Gravity Waves in a Shear Flow"
J. Fluid Mech., 27, pp. 513-539, 1967a
- Bretherton, F.P. and Garrett, C. J. R., "Wave Trains in Inhomogeneous Moving Medium",
Proc. Roy. Soc., A, 302, pp. 529-554, 1968
- Bretherton, F. P., "On the Mean Motion Induced by Internal Gravity Waves"
J. Fluid Mech., 36, pp. 785-803, 1969a
- Bretherton, F. P., "Momentum Transport by Gravity Waves"
Quart. J. R. Met. Soc., 95, pp. 213-243, 1969b
- Miles, J. W., "Waves and Wave Drag in Stratified Flows"
Proc. 12th International Congress of Applied Mechanics,
Stanford University, Stanford, Calif., Aug. 1968
Springer, Verlag, Berlin 1969
- Vergeiner, I., "An Operational Linear Lee Wave Model for Arbitrary Basic Flow and Two Dimensional Topography"
Quart. J.R. Met. Soc., 97, pp. 30-60, 1971
- Bretherton, F. P., "The Propagation of Groups of Internal Gravity Waves in Shear Flow"
Quart. J. R. Met. Soc., 92, pp. 466-480, 1966
- Bretherton, F. P., Hazel, P., Thorpe, S. A., and Wood, I. R., Appendix to "The effect of Viscosity and Heat Conduction on Internal Gravity Waves at a Critical Level" by F. Hazel,
J. Fluid Mech., 30, pp. 781-784, 1967b
- Gerbier, N. and Berenger, M., Quart. J. Roy. Met. Soc., 87, 13, 1961
- Danielsen, E. F. and Bleck, R., "Tropospheric and Stratospheric Ducting of Stationary Mountain Lee Waves"
J. of the Atm. Sciences, 27, pp. 758-772, 1970

- Jones, Walter L., "Ducting of Internal Gravity Waves on a Stable Layer with Shear", J. of Geophysical Research, 77, No. 21, pp. 3879-3885, 1972.
- Klieforth, H. and Holmboe, J., "Sierra Wave Project", Final Report, University of California, 1957.
- Aanensen, C. J. M. editor, Geophys. Mem., No. 108, H.M.S.O., London, 1965.
- Hesstvedt, E., Geophys. Publ., 20, pp.10, 1958.
- Bekofske, K. and Liu, V.C., "Internal Gravity Wave - Atmospheric Wind Interaction: A Cause of Clear Air Turbulence", Science, 178, pp. 1089-1092, Dec. 1972.
- Holmboe, J. and Klieforth, "Investigation of Mountain Lee Waves and the Air Flow over the Sierra Nevada", Los Angeles, University of California, Dept. of Meteorology. Final Report, AFCRC Contract No. AF 19(604)-728, 1957.
- Scorer, R.S., "Theory of Waves in the Lee of Mountains", Quart. J. of Roy. Met. Soc., London, 75, pp. 41-56, 1949.
- Witham, G.B., "Dispersive Waves and Variational Principles", Studies in Applied Math. V. 7, Edited by A.H. Taub, 1971, pp. 181-212.
- Hines, C.O., Physics of the Earth's Upper Atmosphere, Prentice-Hall (19), pp. 150.
- Scorer, R.S., Clouds of the World - A Complete Color Encyclopedia, Stackpole Books, Harrisburg, Pa., 1972.
- Ludlam, F.H., "Characteristics of Billow Clouds and Their Relation to Clear Air Turbulence", Quart. J. of Roy. Meteo. Soc., 93, pp. 419-435, 1967.
- Scorer, R.S., "Theory of Airflow Over Mountains II: The Flow Over a Ridge", Quart. J. of Roy. Meteo. Soc., 79, 1953.
- Scorer, R.S., "Air Flow Over an Isolated Hill", Quart. J. Roy. Meteo. Soc., 82, 1956.

Lilly, D.K. "Observations of Mountain-Induced Turbulence," Journal of Geophysical Research, Vol. 76, No. 27, Sept. 20, 1971, pp. 6585-6588.

Lilly, D.K. and Toutenhoofd, W., The Colorado Lee Wave Program, "Clear Air Turbulence and Its Detection," Plenum Press, 1969, pp. 232-245.

Folvik, A., "Two-Dimensional Mountain Waves - A Method for the Rapid Computation of Lee Wavelengths and Vertical Velocities." O.J. Roy. Meteor. Soc., Vol. 88, pp. 271 - 285.

Conover, J.H., "The Identification and Significance of Orographically Induced Clouds Observed by TIROS Satellites. J. Appl. Meteor., Vol. 3, pp. 226 - 234.

Lovill, J.E., "Transport Processes in Orographically Induced Gravity Waves as Indicated by Atmospheric Ozone" Dept. of Atmospheric Science, Colorado State University, Fort Collins, Colorado, Feb. 1969, Atmospheric Science Paper No. 135.

APPENDIX I
LASER DOPPLER VELOCIMETERS: ANALYSIS

by
J. Alex Thomson and Mark F. Dorian

1.0 INTRODUCTION

In this appendix we present an analysis of a general bistatic laser doppler velocimeter system and its application to the measurement of atmospheric winds in the presence of turbulence. This analysis is excerpted from a draft of a report originally co-authored in 1967 by one of the present authors (JALT). Although several copies of the report have been circulated privately, no formal distribution has ever been made. Part of the work covered here has been treated subsequently by Sonnenschein (1970)--particularly that for the coaxial configuration in the absence of turbulence, and that work follows closely the approach described herein. However, since neither the bistatic configuration nor the effects of turbulence appear to have been treated elsewhere, we include the entire treatment here. Section 4.2 of this Appendix, "Atmospheric Attenuation", was updated by F.P. Boynton to reflect current atmospheric transmission models.

2.0 ANALYSIS

2.1 General

In a typical optical heterodyne system for detection of scattered light, an optical transmitter projects a beam of coherent light into a particle cloud. After passing through the receiver optics (which are focused at some particular point in the incident beam), the scattered light is mixed with a coherent reference beam. The mixed beam is then detected by a square law photodetector and the spectrum of beat frequencies is diagnosed to evaluate the particle velocity distributions. The transmitter optics may act also as the receiver optics (for direct backscatter measurements) or separate optical systems may be used. The antenna properties of such detection systems are well understood in the radio and microwave frequency region and, as is well known, the identical analysis applies to optical heterodyne systems; the only differences of importance to the present discussion are associated with the dimensions of the near field of the antennas*. For easily available optical apertures (say up to 30 cm), the length of the near field for visible wavelengths can be as large as 200 kilometers, whereas at common radar wavelengths, for example 10 cm, the near

* The near field (Fresnel or transitional region) extends to the range at which diffraction has doubled the width of a collimated beam. Only within the near field can focusing be achieved.

field for antennas up to 10 meters diameter is less than one kilometer. Thus, in applying results from radar and microwave theory to optical heterodyne systems, it is important to remember that theory valid only for the far field may be inapplicable at typical atmospheric ranges for some optical systems. This point is critical to the present application since it turns out that the greatest sensitivity for detection of aerosol motion at moderate ranges (.01 to 1.0 km) in the atmosphere is achieved at direct ($\theta = \pi$) backscatter. The only way of obtaining range discrimination with CW monostatic systems under these conditions is to focus on the region of interest and this can only be accomplished by working in the near field. In the far field it is necessary either to utilize pulsed systems or to work with crossed beams (i.e., scattering angles different than π).

In the present analysis, the Fresnel-Kirchoff formulation is used to evaluate the signal-to-noise ratio for the heterodyne detection of the Doppler-shifted light scattered from a cloud of moving particles. However, before proceeding to this detailed analysis, it is instructive to treat a simplified model of the scattering and detection process that contains the basic elements of the more detailed formulation but not the complex formalism.

2.1.1 Simple Model

There are two quantities which must be evaluated to determine the signal-to-noise ratio that can be expected in a Doppler-scattering measurement of a particle cloud: the level of the signal return from an individual particle and the number of particles or volume of space that can be heterodyned efficiently at one time. If N is the total number of photons transmitted during the observation time and σ the particle scattering cross section (at the appropriate angle), then the number of photons scattered by a particle located within the transmitter beam at a station where its cross sectional area has the value d_t^2 is $N \sigma / d_t^2$. Assuming the area of the receiver aperture to be πR_r^2 and that it is located at a range L , the number of photons detected by the receiver is $\eta N \sigma \pi R_r^2 / d_t^2 (4\pi L^2)$, where η is the detector quantum efficiency. The power signal-to-noise ratio (i.e., the number of received photons which contribute significantly to the heterodyne signal) is

$$[\eta N n_f \sigma \pi R_r^2 / d_t^2 (4\pi L^2)] V_H .$$

Here n_f is the local density of particles in the velocity range of interest and V_H is the volume of the cloud that can be heterodyned effectively.

The easiest configuration to visualize is that where the receiver optics are focused at some point in the transmitter beam. In the normal heterodyne system, the local oscillator (reference beam) may be considered a point source. A diffraction limited virtual image of this point source is present in the particle cloud at the focal point of the receiver optics. This image is a slender ellipsoid with a diameter (d_r) of the order $\lambda L / 2R_r$ and a length determined by the depth of focus ($\approx 2d_r L / R_r$). Any light scattered by a particle in this volume will have wavefronts that are parallel, within a fraction of a wavelength, to the reference beam wavefronts and will thus give rise to strong beat frequencies. Light scattered from particles outside this volume will have wavefronts that are either inclined to reference beam fronts or have a considerably different curvature and will thus not result in broad fringes (i.e., will not chop efficiently). The more detailed calculations presented in the next section show that, although less important, the region outside the diffraction ellipsoid is not completely negligible at backscatter. Nevertheless, for a very rough estimate of V_H , we will use a value equal to that volume of the transmitter beam which is intersected by the virtual ellipsoidal image of the local oscillator (see Figure I-1).

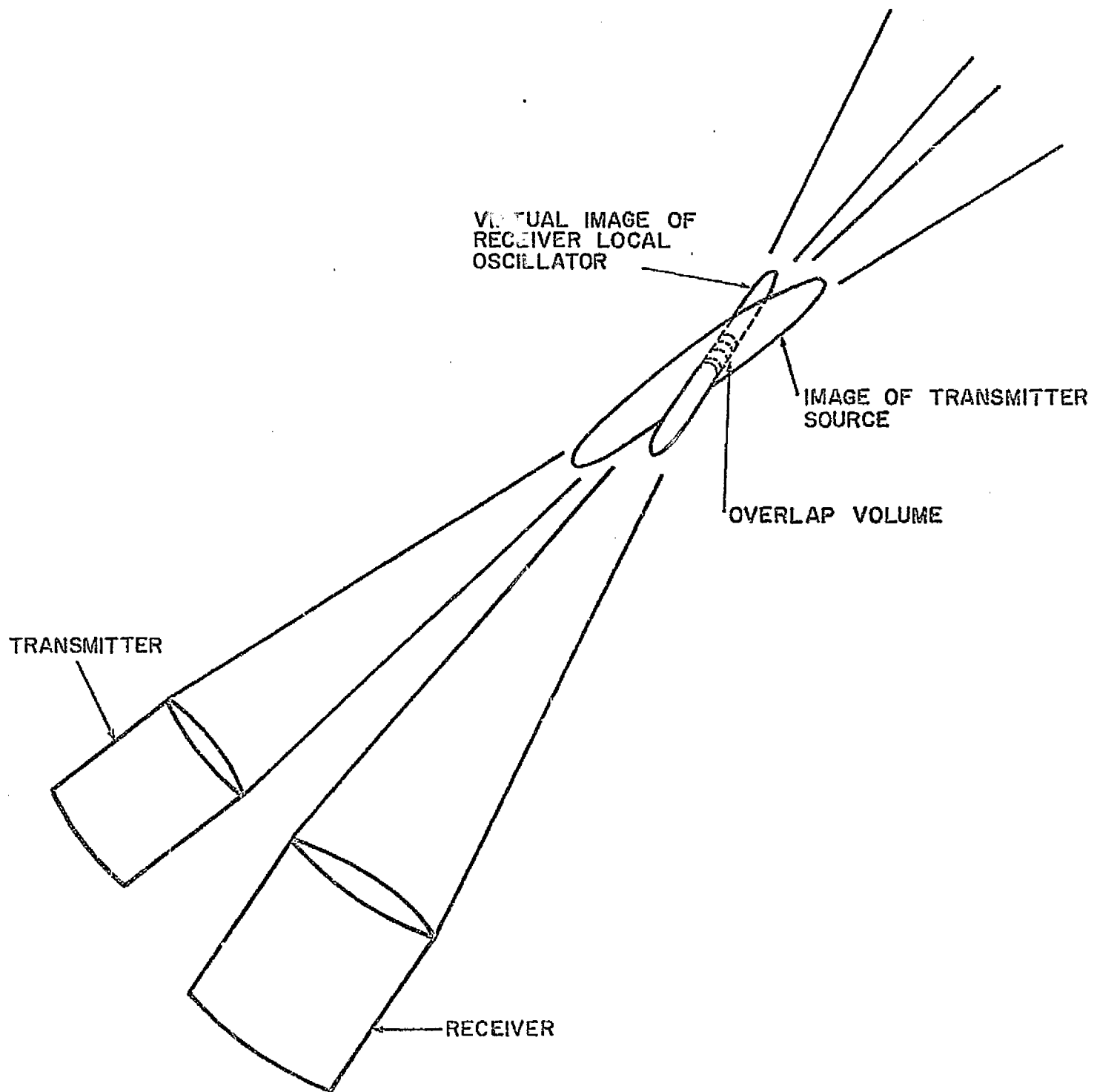


Figure I-1. Effective Detection Volume for Separate Transmitter and Receiver

For scattering at angles large compared to both R_r/L and to the angular width of the transmitter beam, this volume is approximately equal to

$$d_t^2 d_r^2 / \sin\theta \sqrt{d_t^2 + d_r^2}$$

whereas for direct backscatter, it is of the order

$$2d_r^3 d_t^2 L/R_r (d_r^2 + d_t^2)$$

The approximation of uniform transmitter beam width and negligible contributions from regions outside the receiver diffraction ellipsoid are poor for direct backscatter and render this latter expression useful only when $d_t \approx d_r$.

When the transmitter is focused on the same point as in the receiver, d_t is equal to $\lambda L/2R_t$ and the power signal-to-noise ratio for scattering at a finite angle ($\sin\theta \gg R/L$) is given by the expression

$$(S/N) \approx \left(n N n_f \sigma \frac{\lambda}{4} \right) \frac{R}{2L \sin\theta} \quad (I-1)$$

where R is effectively the smaller of R_r or R_t
 $(R = R_r R_t / \sqrt{R_r^2 + R_t^2})$. At backscatter for equal apertures
 $(0 < \pi$ and $R_t = R_r$):

$$(S/N) \approx \frac{1}{2} \left(\eta N n_f \sigma \frac{\lambda}{4} \right). \quad (I-2)$$

These expressions agree with the results of the more exact calculation described in the latter part of this section except for numerical factors of order 0.5. According to Eq. (I-2), the signal-to-noise ratio at backscatter is independent both of range and of aperture, whereas for scattering at a finite angle, it increases with aperture and decreases with range. Siegmann³ indicates that the value $\eta N n_f \sigma \lambda/4$ (i.e., essentially the backscatter value) is an upper limit for the signal-to-noise ratio that can be achieved with normal heterodyne systems. Although it is theoretically possible to attain signal-to-noise ratios greater than this limit, the optical or electronic techniques required to achieve these increases are sufficiently complex and awkward that they may not be practical.

Comparison of Eqs. (I-1) and (I-2) shows that, at moderately long ranges where the angle subtended by the aperture is small, the signal-to-noise exhibits a strong dependence on scattering angle. For an aperture of 10 cm diameter and a range of 100 meters, the direct backscatter signal is three or four orders of magnitude greater than that for right-angle scatter. These high levels can be achieved, however, only for scattering angles very close to 180° (within 0.3 milliradians for this example).

At direct backscatter the range resolution for a CW system is determined by the depth of focus ($\delta L \approx \lambda L^2/R^2$) and, in the visible for a 10 cm aperture, is of the order of 2% at 100 meters range and 20% at a kilometer. At ranges comparable to or greater than the length of the near field ($L \approx R^2/\lambda$), significant resolution can only be obtained by pulsing the laser or by working at finite scattering angles. In this latter method, the range resolution is of the order $\lambda/2R \sin\theta$. When the scattering angle is always adjusted to yield a given range resolution, the signal-to-noise ratio exhibits the expected inverse square dependence on range:

$$(S/N) \approx \left(n N n_f \sigma \frac{\lambda}{4} \right) L_n \delta L / L^2 \text{ for } L \gg L_{\text{near field}} . \quad (I-3)$$

In the following section we carry out a more rigorous analysis of the scattering-heterodyne measurement for more general conditions than the focused configuration just considered. The calculation is essentially a more exact formulation of the above model. In Section 3 we repeat the calculations including the distorting effects of atmospheric turbulence between the scattering point and the transmitter-receiver system.

2.2 Fresnel-Kirchoff Formulation

In order to obtain a formulation that will permit fairly general optical configurations to be considered but also allow explicit and simple evaluation of the various integrals that arise, we will introduce a number of simplifying assumptions. First, we assume that the angle between the axis of the transmitting lens or mirror and the receiver axis is sufficiently small that various cosine terms can be set equal to unity. This will limit the scattering angles which can be treated to be within 5 or 10 degrees of direct forward or backscatter. The extension to larger angles will be made subsequently in a less rigorous fashion on the basis of the physical picture that evolves from the more detailed analysis. Second, we assume the radial intensity distributions in the transmitted and reference beams are Gaussian [i.e., $|\psi|^2 \sim \exp(-2r^2/R^2)$] and the field stops in the transmitter and receiver optics do not appreciably vignette these beams. This is a fairly good approximation for well adjusted single mode lasers (see Figure I-2). This approximation permits explicit and simple evaluation of the various integrals that arise in the Fresnel approximation. We also assume that separate beam expanders are used in transmitter and reference beams so that the widths of the two beams may be controlled independently (see

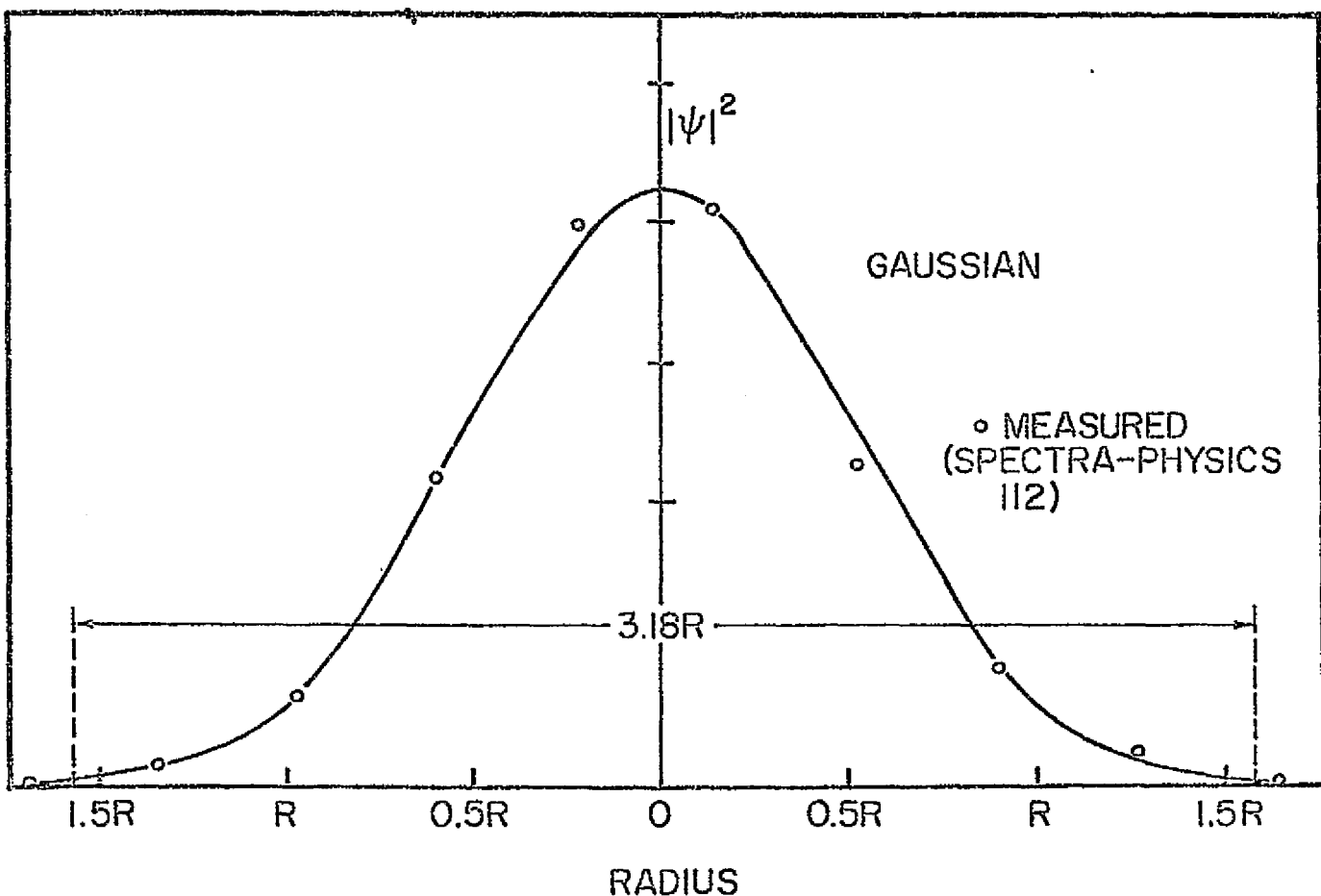


Figure I-2. Comparison of Measured Radial Intensity Distribution with Theoretical Gaussian Distribution.

Figure I-3). Third, we neglect any depolarization effects and use a scalar formulation of the wave equation.

The optical configuration considered is shown in Figure I-3. At a range L from the transmitter, the amplitude of the outgoing beam at a distance $\vec{r} = (x, y)$ from the optical axis is proportional to

$$\psi = \sqrt{2} A_t \frac{\exp[i(kL - \omega t)]}{\sqrt{\pi} L R_t \lambda} \int_{-\infty}^{\infty} \int_{-\infty}^{\infty} \exp\left[i \frac{\pi}{\lambda L} (\vec{r} - \vec{r}'')^2 - \frac{i\pi \vec{r}''^2}{\lambda f_t} - \frac{\vec{r}''^2}{R_t^2}\right] dx'' dy'' \quad (I-4)$$

where \vec{r}'' is the radius vector to a point x'', y'' in the plane of the transmitting lens and A_t^2 is the total transmitted flux (in photons/sec). The amplitude has been normalized so that

$$\int |\psi|^2 d\vec{r} = A_t^2$$

Equation (I-4) may be shown to be equivalent to the expression

$$\psi = \frac{\sqrt{2} R_t A_t}{\lambda L \eta^2} \exp\left\{i(kL - \omega t + \phi_t) - (\beta_t \vec{r}/R_t)^2 / \left[1 + \beta_t^2 (1 - \xi_t)^2\right]\right\} \quad (I-5)$$

where

$$\beta_t = \pi R_t^2 / \lambda L$$

$$\xi_t = L/f_t$$

$$\eta^2 = 1 - i \beta_t (1 - \xi_t)$$

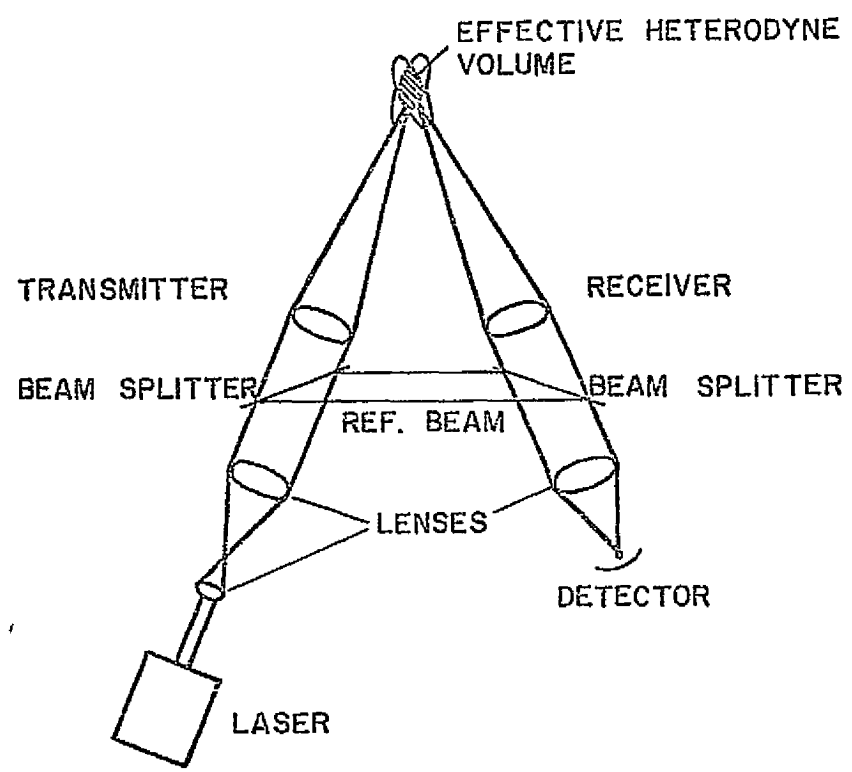


Figure I-3. Optical Configuration

and

$$\phi_t = \frac{\pi r^2}{\lambda L} \left[\frac{1 - \beta_t^2 (1 - \xi_t) \xi_t}{1 + \beta_t^2 (1 - \xi_t)^2} \right].$$

At the beam splitter or mixer in the receiver, the amplitude of the wave scattered by a particle in the plane L but displaced an amount \vec{r} from the transmitter axis is given by

$$\psi_{sc}(\vec{r}') = \frac{\sqrt{\sigma/\pi}}{2L} \psi \exp \left\{ -i \left[\frac{\pi}{\lambda f_r} (\vec{r} - \Delta \vec{r})^2 - \frac{2\pi}{\lambda} (\vec{r}' - \Delta \vec{r}) \cdot \vec{n}_r \right. \right. \\ \left. \left. - \frac{\pi}{\lambda L} (\vec{r} - \vec{r}')^2 - (kL + \Delta \omega t) \right] \right\} \quad (I-6)$$

where $\Delta\omega (= \omega v/c)$ is the Doppler shift due to the component of velocity of the particle parallel to the line bisecting the optical axes of the transmitting and receiving lens and σ is the backscattering cross section of the particle. Here f_r is the focal length of the receiver lens, \vec{n}_r is a unit vector parallel to the receiver optic axis (which is inclined at an angle θ to the transmitter axis) and $\Delta \vec{r}$ is the separation of the two lenses. Low frequency chopping of the transmitted beam, although desirable in practice, is irrelevant to the present analysis and is ignored, although if present it would reduce the average signal power by a factor of 2. The reference beam which is added to the scattered signal at the mixer has been chosen to be a plane wave:

$$\psi_{\text{ref}} = \alpha A_t \exp[-i\omega t + i\phi - (\vec{r}' - \Delta\vec{r})^2/R_r^2] \quad (I-7)$$

where α is some constant amplitude factor and ϕ a constant phase difference. We may set $\phi = 0$ with no loss of generality. The photocurrent per unit effective area induced in the detector is equal to $\eta |\psi_{\text{sc}} + \psi_{\text{ref}}|^2$ electrons/cm²-sec where η is the quantum efficiency (electrons/photon). In a well designed system, the reference signal level is to be chosen so that $|\psi_{\text{ref}}|^2 \gg |\psi_{\text{sc}}|^2$. Thus, the total signal current is given by the expression

$$i_s = \int W(\vec{r}') \eta (\psi_{\text{sc}} \psi_{\text{ref}}^* + \psi_{\text{sc}}^* \psi_{\text{ref}}) d\vec{r}' \text{ electrons/sec} \quad (I-8)$$

and the reference current is

$$i_R = \int W(\vec{r}') \eta |\psi_{\text{ref}}|^2 d\vec{r}' \text{ electrons/sec} . \quad (I-9)$$

Here $W(\vec{r}')$ is the apodization or transmission function for the receiver aperture and, in the present analysis, is assumed equal to unity over the region where $|\psi_{\text{ref}}|^2 \neq 0$. The signal current per unit effective detector area is equal to the real part of the expression

$$\alpha \eta A_t^2 \frac{\sqrt{2\sigma}}{\lambda L^2} R_t \exp \left[i(\Lambda \omega t + \phi) - \frac{(\beta_t \vec{r}/R_t)^2}{1+\beta_t^2 (1-\xi_t)^2} - \frac{(\vec{r}' - \Delta\vec{r})^2}{R_r^2} \right]$$

where

$$\phi = \frac{\pi r^2}{\lambda L} \left[1 - \frac{\beta_t^2 (1-\xi_t)}{1+\beta_t^2 (1-\xi_t)^2} \right] + \frac{\pi}{\lambda L} (\vec{r}-\vec{r}')^2 - \frac{\pi}{\lambda f_r} (\vec{r}'-\Delta\vec{r})^2 + \frac{2\pi\vec{n}_r \cdot (\vec{r}'-\Delta\vec{r})}{\lambda} .$$

After carrying out the integration over the receiver aperture, we find the signal current due to the scattering by an individual particle to be given by the expression

$$(i_s)_{\text{particle}} = \eta \alpha A_t^2 \frac{\sqrt{2\sigma} R_t}{\lambda L^2} \pi R_r^2 \frac{\exp\left(-\left\{\frac{(\beta_t \vec{r}/R_t)^2 + [\beta_r (\vec{r}-\Delta\vec{r}')/R_r]^2}{1+\beta_t^2 (1-\xi_t)^2} + \frac{[\beta_r (\vec{r}-\Delta\vec{r}')/R_r]^2}{1+\beta_r^2 (1-\xi_r)^2}\right\}\right)}{\sqrt{\left[1+\beta_t^2 (1-\xi_t)^2\right] \left[1+\beta_r^2 (1-\xi_r)^2\right]}} \times \cos(\Delta\omega t + \phi') . \quad (I-10)$$

Here ξ_r and β_r are defined in a fashion analogous to that for ξ_t and β_t . The term ϕ' is a phase factor which depends on the system parameters as well as the coordinates of the scattering particle, and the vector $\Delta\vec{r}'$ is the separation of the two optic axes at the range L . If the axes intersect at some range L_0 , $\Delta\vec{r}'$ has the magnitude $\Delta r = L \sin\theta = (L_0 - L) \sin\theta$ and is parallel to $\Delta\vec{r}$.

In the near field of both the transmitter and receiver ($\beta_t, \beta_r \gg 1$), Eq. (I-10) indicates that the signal current is large only for particles that simultaneously fall within the diffraction ellipsoid that corresponds to the image of the receiver local oscillator (also a point source).

In the far field these two images become the usual conical lobes rather than ellipsoids. When a single particle is being tracked (i.e., it is at the focus of both the transmitter and the receiver: $\vec{r} = \Delta\vec{r}' = 0$, $\xi_r = \xi_t = 1$, the total power signal-to-noise ratio, i_s^2/i_n^2 , can be shown to be given by the relation

$$(S/N) = \left[\eta N (\pi R_t^2) (\pi R_r^2) \sigma / \pi L^4 \lambda^2 \right] \left[\frac{1}{2 \cos^2(\Delta\omega t + \phi')^2} \right] \quad (I-11)$$

where N is the total number of photons transmitted ($= A_t^2 \tau$) and we have assumed the noise to be only shot noise in the reference beam*. Since the observation time τ is typically much greater than the beat period $2\pi/\Delta\omega$, this expression may be rewritten in the more familiar form

$$(S/N) = \eta N G_t G_r \frac{\sigma (\lambda^2 / 4\pi)}{(4\pi L^2)^2} . \quad (I-12)$$

Here G_t and G_r are gains of the transmitter and receiver antennae relative to omnidirectional antennas:

$$G_t = 8\pi^2 R_t^2 / \lambda^2$$

$$G_r = 8\pi^2 R_r^2 / \lambda^2$$

*The shot noise power (i_n^2) in a bandwidth $1/\tau$ is equal to $2i_R/\tau$, i.e., to $\eta \alpha^2 A_t^2 \pi R_r^2 / \tau$.

and $\lambda^2/4\pi$ is the effective aperture of an isotropic receiver*.

When all the scatterers lie within both diffraction lobes (far field) or diffraction ellipsoids (near field) of the transmitter and the receiver, the signal-to-noise ratio exhibits the usual proportionality to both antenna gains and to the inverse fourth power of the range. However, when the particles are distributed over larger volumes, only those within overlap of the two diffraction lobes or ellipsoids can be detected efficiently in a heterodyne system. In this case the functional dependence on range, aperture, wavelength, and scattering angle can be quite different.

Since the signal currents due to waves scattered by different particles add incoherently, we obtain the total signal power by summing the power due to each particle. If $n_f(L)$ is the number density of particles at the range L that give rise to a Doppler beat frequency within the band pass Δf of the electronic filters, the total signal power from all particles is given by the expression

$$i_s^2 = \int (i_s^2)_{\text{particle}} n_f(\vec{r}, L) d \text{vol} . \quad (\text{I-13})$$

Assuming that the particle density is uniform over the beam cross section, we may express this power in the form

* These gain expressions are equivalent to the usual expressions for radar antennas if the effective antenna areas are taken to be $2\pi R_t^2$ and $2\pi R_r^2$.

$$i_s^2 = \frac{\eta^2 \alpha^2 A_t^4 (\pi R_r^2)}{2} \int_0^\infty \text{on}_f(L) R_t^2 R_r^2 \exp \left[-2 \left(\frac{\pi R_r}{\lambda} \right)^2 \frac{R_t^2}{R_t^2 + R_r^2} \left(\frac{\Delta x'}{L} \right) \right] dL \quad (I-14)$$

where we have defined

$$R_t^2 = R_t^2 / [1 + \beta_t^2 (1 - \xi_t)^2]$$

and

$$R_r^2 = R_r^2 / [1 + \beta_r^2 (1 - \xi_r)^2] .$$

In a well designed system, the noise should be only shot noise from the reference beam. Thus, the noise power in a band width $1/\tau$ is given by

$$i_n^2 = \eta \alpha^2 A_t^2 \pi R_r^2 / \tau \text{ (electron/sec)}^2 . \quad (I-15)$$

In order to obtain an easily interpretable expression for the power signal-to-noise ratio, it is desirable to define a number of characteristic parameters for the optical system. It will be found more convenient to represent the results in terms of two mean focal lengths f_1 and f_2 , where

$$f_1 = \left(\frac{R_r^2}{f_r} + \frac{R_t^2}{f_t} \right) / \left(\frac{R_r^2}{f_r^2} + \frac{R_t^2}{f_t^2} \right)$$

and

$$f_2 = \left[\left(\frac{R_t^2}{f_t^2} + \frac{R_r^2}{f_r^2} \right) / \left(\frac{R_r^2}{f_r^2} + \frac{R_t^2}{f_t^2} \right) \right]^{\frac{1}{2}}$$

The ratio f_1/f_2 is close to unity under all conditions.

When one aperture greatly exceeds the other, f_1 and f_2 both approximate the value of the focal length of the larger aperture system. When the two apertures are equal, both f_1 and f_2 approximate the value of the smaller of f_t or f_r .

Also, it is convenient to define a characteristic range L^* according to the relation

$$L^* = f_1 / \left[1 + (\lambda f_2 / \pi R_t R_r)^2 \right]$$

a depth of field parameter ΔL by the expression

$$\Delta L = \left\{ \left[\frac{\lambda f_1 / \pi R_t R_r}{1 + (\lambda f_2 / \pi R_t R_r)^2} \right]^2 + \frac{\left[\frac{R_r R_t}{(R_r^2 + R_t^2)} \left(\frac{f_2}{f_t} - \frac{f_2}{f_r} \right) \right]^2}{\left[1 + \left(\frac{\lambda f_2}{\pi R_t R_r} \right)^2 \right]} \right\}^{1/2} f_2$$

and an angular spreading parameter γ by the relation

$$\gamma = \sqrt{\theta_{\text{geom}}^2 + \theta_{\text{diff}}^2}$$

where

$$\theta_{\text{geom}} = \sqrt{R_r^2 + R_t^2 / f_2}$$

$$\theta_{\text{diff}} = \lambda \sqrt{R_t^2 + R_r^2} / \pi R_t R_r$$

In terms of these parameters and assuming that the optic axes intersect at a range L_o , the power signal-to-noise ratio may be expressed in the form

$$(S/N) = \frac{nN}{2} \left(\frac{\lambda}{\pi \gamma} \right)^2 \int_0^\infty \sigma n_f(L) \frac{\exp \left(-\left\{ 2 \sin^2 \theta (L-L_o)^2 / \gamma^2 [(L-L^*)^2 + \Delta L^2] \right\} \right)}{[(L-L^*)^2 + \Delta L^2]} dL \quad (\text{I-16})$$

where N is the total number of transmitted photons in the observation time τ .

We first consider the case of direct backscatter. For a uniform distribution of particles, the power signal-to-noise ratio in this case is given by the expression

$$(S/N) = \frac{\pi}{2} \frac{nN}{\Delta L} \left(\frac{\lambda}{\pi \gamma} \right)^2 \overline{\sigma n_f} \left(\frac{1}{2} + \frac{1}{\pi} \tan^{-1} \frac{L^*}{\Delta L} \right) \quad (\text{I-17})$$

with the major contribution coming from an interval of length ΔL . In order that a significant range resolution be obtained, the depth of field ΔL must be small compared to

the effective range L^* , i.e., the apertures must be chosen large enough that the particles are in the near field ($\lambda f_2 / \pi R_t R_r \ll 1$). In this case the signal-to-noise ratio may be expressed in the form

$$(S/N) = \eta N \frac{\pi}{n_f \sigma} \frac{2R_t R_r}{(R_r^2 + R_t^2)} \cdot \frac{|f_2/f_1|}{\left\{ 1 + \left[\frac{\pi R_t^2 R_r^2}{\lambda f_1 (R_r^2 + R_t^2)} \left(\frac{f_2}{f_t} - \frac{f_2}{f_r} \right) \right]^2 \right\}} \quad (I-18)$$

In Figure I-4 we have plotted the signal-to-noise ratio as a function of receiver aperture for the case $f_r = f_t$. According to Eq. (I-18), the maximum signal-to-noise and the sharpest range resolution is obtained only when the diffraction patterns of the transmitter and receiver match, i.e., when both $R_t = R_r (= R)$ and $f_t = f_r (= L_o)$. The power signal-to-noise ratio then has the value

$$(S/N) = \eta N \frac{\pi}{n_f \sigma} \frac{1}{4} \quad (I-19)$$

and the range resolution is equal to the depth of focus for the diffraction limited image of a point source:

$$\delta L \approx \pi \Delta L = \lambda (L_o)^2 / R^2 \quad (I-20)$$

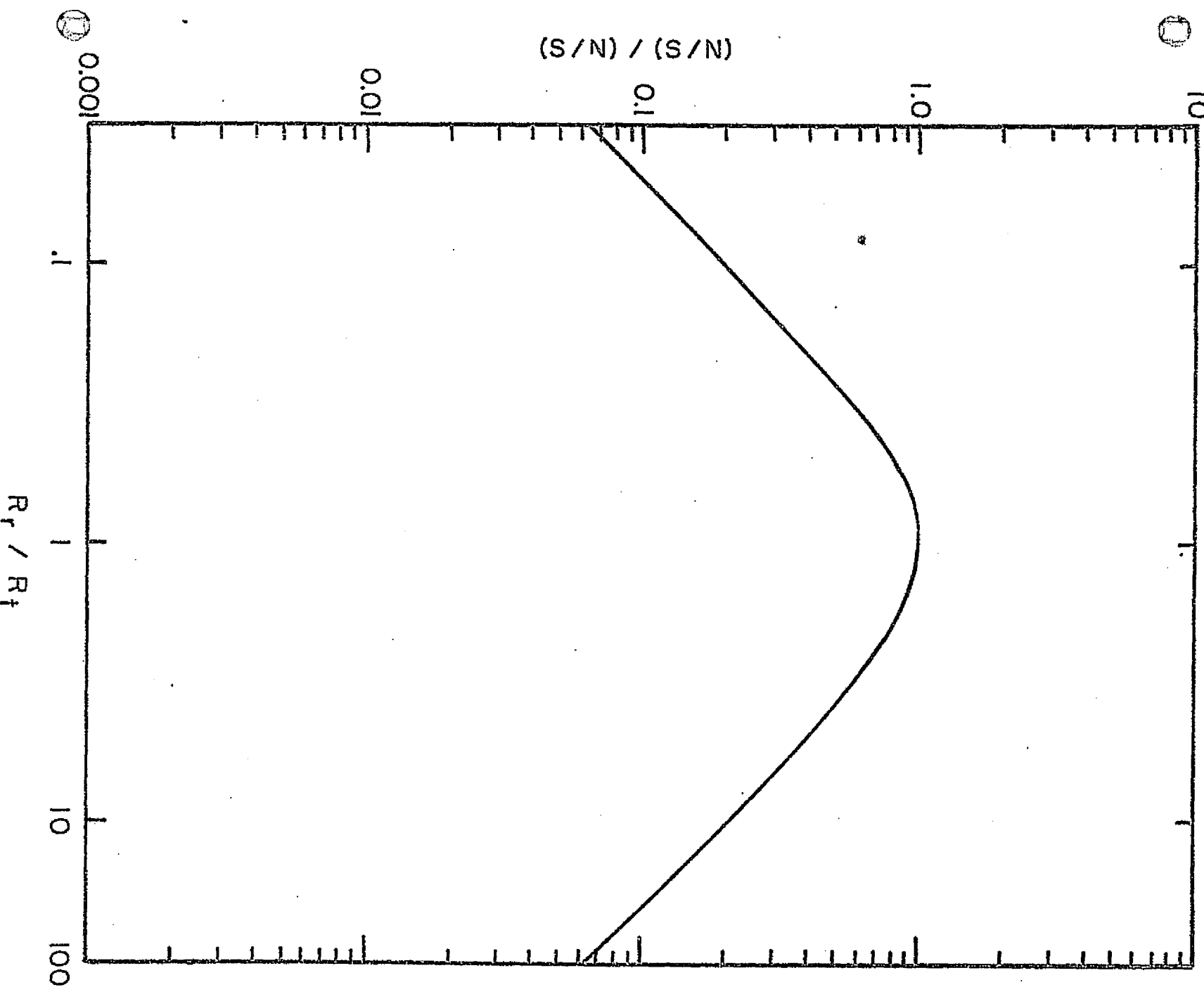


Figure I-4 Signal-to-Noise vs. Receiver/Transmitter Aperture Ratio.

For scattering at angles which are considerably greater than the beam spreading angle γ , the transmitter and receiver antenna patterns only overlap in the neighborhood of the range point L_o . In this case the signal-to-noise ratio is given by the expression

$$(S/N) = \eta N \frac{n_f}{\sigma} \frac{\pi}{4} \sqrt{\frac{2}{\pi}} \left[\frac{\lambda/\pi \gamma \sin\theta}{\sqrt{(L_o - L^*)^2 + \Delta L^2}} \right] \quad (I-21)$$

and the range resolution

$$\delta L \approx \sqrt{\pi} \gamma \sqrt{(L_o - L^*)^2 + (\Delta L)^2} / \sqrt{2} \sin\theta \quad . \quad (I-22)$$

In this finite scattering angle case, the maximum signal-to-noise ratio will be obtained when both transmitter and receiver are focused on the same point:

$$(S/N) = (S/N)^* \sqrt{\frac{2}{\pi}} \frac{R_t R_r}{L \sqrt{R_t^2 + R_r^2} \sin\theta} \quad . \quad (I-23)$$

Here $(S/N)^*$ is the maximum value for direct backscatter $(\eta N \frac{n_f}{\sigma} \frac{\pi}{4})$. For equal apertures the range resolution and the signal-to-noise ratio are given by the relations

$$\frac{\delta L}{L} = \lambda / \sqrt{\pi} R \sin\theta$$

and

$$\begin{aligned}(S/N) &= (S/N)^* R/\sqrt{\pi} L \sin\theta \\ &= (S/N)^* (R^2/\lambda L) (\delta L/L)\end{aligned}\quad . \quad (I-24)$$

Thus, when perfect, matched optics are focused on the range point and the scattering angle is adjusted so as to yield the desired range resolution δL , the S/N for a heterodyne detection system is identical to that for incoherent detection $[\eta N n \sigma (\pi R^2/4\pi L^2) \delta L]$. This will not, in general, be true for other optical configurations. For example, if collimated transmitter and receiver beams are used ($f_r = f_t = \infty$), the signal-to-noise ratio is given by

$$(S/N) = (S/N)^* R/\sqrt{\pi} \sin\theta \sqrt{L^2 + (\pi R^2/\lambda)^2} \quad . \quad (I-25)$$

In contrast to the focused configuration, the signal-to-noise ratio as a function of aperture for collimated beams has a maximum value when the aperture radius equals $\sqrt{\lambda L/\pi}$ and, at larger apertures, falls well below the value for a focused configuration. In general, any attempt to broaden the beam to accept larger solid angles (this is equivalent to setting f_r, f_t to infinity or negative) necessarily results in a reduction of the signal-to-noise ratio. For the crossed beam system just considered, the heterodyne

signal-to-noise ratio in the near field is reduced below the incoherent value by the factor $[1 + (\pi R^2 / \lambda L)^2]^{-1}$ if collimated rather than focused beams are used; this would entail a loss of about 15 db in the visible for $R = 1$ cm and $L = 100$ meters.

In Figure I-5 we have plotted, for various ranges, the maximum signal-to-noise ratio that can be attained at a given scattering angle with a 10 cm diameter aperture. In general, the levels shown can be reached only with matched and focused optics. The range resolutions that can be obtained in the visible with this aperture are indicated in the figure. It is apparent from this figure that, for moderate range resolution requirements ($\delta L/L > 10^{-3}$), the maximum signal-to-noise is obtained very close to direct back (or forward) scatter and that orders of magnitude loss in sensitivity may result if the scattering angle is chosen improperly.

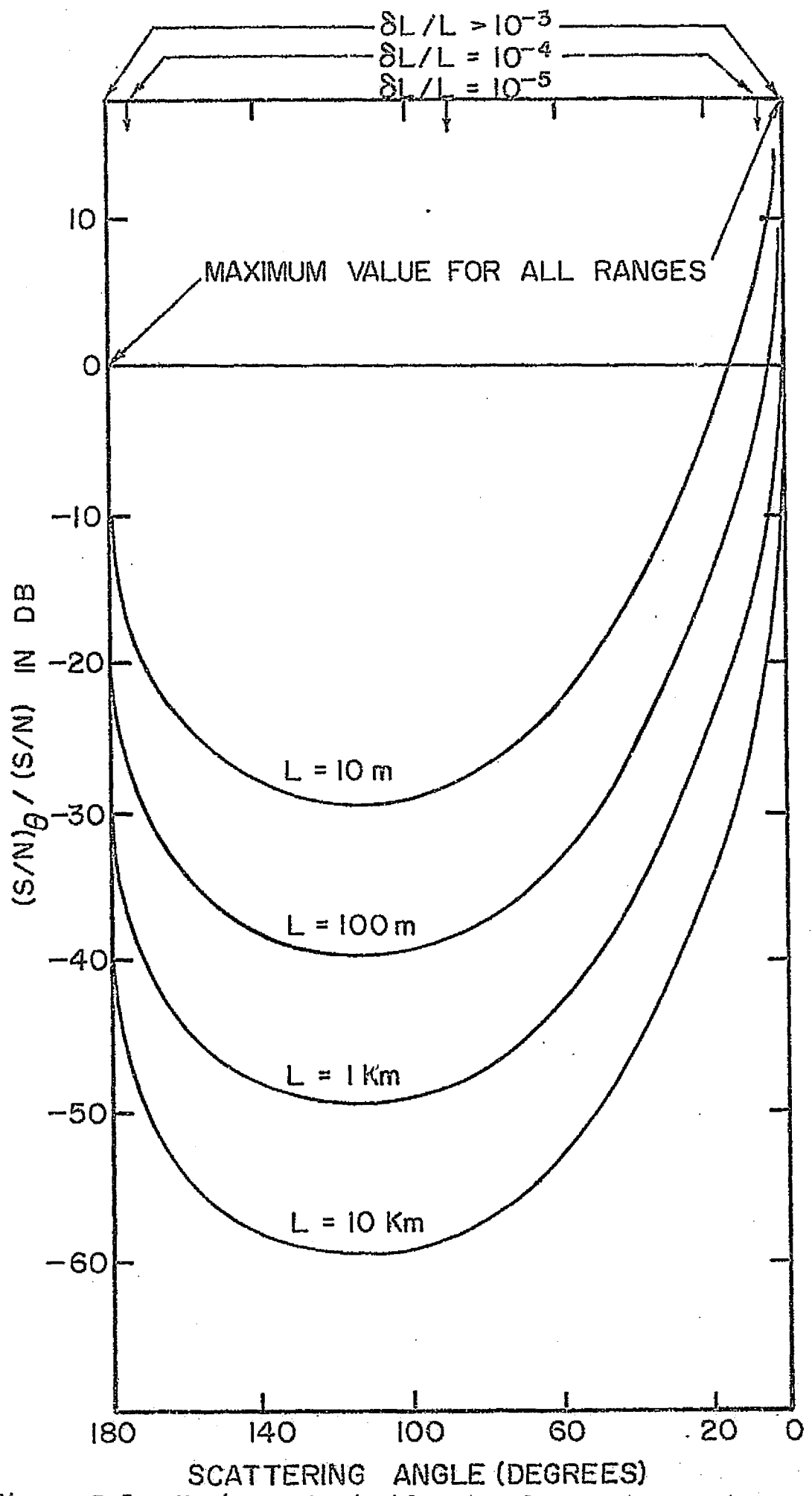


Figure I-5. Maximum Attainable Signal-to-Noise Ratio as a Function of Scattering Angle.

3.0 ATMOSPHERIC PROPAGATION EFFECTS

3.1 Turbulence Effects

Atmospheric turbulence between the scattering point and the transmitter and receiver will degrade the signal at long ranges. Inhomogeneities in the refractive index in the propagation path cause amplitude modulation, spreading, and wandering of the outgoing beam. The effect of turbulence on the returning beam may be thought of as a spreading and wandering of the virtual image of the local oscillator coupled with a fluctuating modulation of the receiver antenna gain.

The propagation of coherent beams through the atmosphere has been studied by a number of investigators.

Spreading and wandering of a coherent laser beam have been measured by Hinchman and Buck⁶ over 9- and 90-mile paths under clear night conditions of low humidity and stable winds of 5 to 7 mph. The (theoretical) beam width of 1.25 seconds of arc had spread to 8.7 seconds at 9 miles and 13 seconds at 90 miles. Further, the beam wandered about over a region several times the beam width. Straub⁷ has measured beam excursions up to 6 meters in a 3.5 km pathlength. Fried⁸ has shown theoretically that, for transmission of a modulated coherent beam from one point to another, little improvement in signal-to-noise can be obtained by increasing the collector aperture beyond a

certain critical diameter, which is characteristic of the phase structure function for the pathlength involved.

Goldstein, Miles, and Chabot⁹ have measured the effective aperture diameter for pathlengths of 4.0 and 23.8 km and obtained results in essential agreement with theoretical predictions.

An additional effect associated with random phase variations is that of frequency spreading of the signal.

Hodara¹⁰ has calculated the effect:

$$\langle \Delta f^2 \rangle = \frac{LL_c}{\lambda^2} \frac{\langle \Delta n^2 \rangle}{t_c^2}, \quad (I-26)$$

where L is the pathlength, L_c a coherence length associated with the outer scale size of turbulence which has been empirically determined to be of the order $\frac{0.4 h}{1 + 10^{-2}h}$ (h the altitude in meters), Δn the relative change in index of refraction associated with the turbulent cell, also empirically determined as approximately

$$\langle \Delta n^2 \rangle = 10^{-12} e^{-\frac{h}{1600}},$$

and t_c is the coherence time.

For a wavelength $\lambda = 0.6\mu$, L = 10 km, h = 1 km, $\langle \Delta n^2 \rangle = 10^{-12}$ and t_c = 1 second, the rms frequency spread is about a kilohertz. For the present Doppler scattering

problem, this effect may be safely ignored.

In general, the measured time-averaged propagation effects are consistent with existent propagation theory based on the Kolmogoroff theory of isotropic turbulence (such as that formulated by Tatarski¹¹). Most of the existent analyses, however, apply to the propagation of a collimated beam from a transmitter to a remotely located receiver and need to be modified somewhat for application to the present scattering problem. In this section we will evaluate the signal-to-noise ratio for detection of Doppler scattering in a manner similar to that given in the preceding section but will include the atmospheric propagation effects. It will be shown that the principal effects of atmospheric turbulence in the optical path are a reduction in the signal-to-noise ratio and a loss in range resolution. The analysis closely follows that of the previous section and only the differences necessitated by the inclusion of propagation effects will be indicated explicitly here.

When atmospheric propagation effects are important, the integrand in Eq. (I-4) should be multiplied by a factor $\exp[\chi(\vec{r}, \vec{r}'')]$ to account for the fluctuations in the amplitude of the outgoing beam due to inhomogeneities in the refractive index along the propagation path. Here $\chi(\vec{r}, \vec{r}'')$ is the perturbation to the log amplitude between the point \vec{r}'' in the transmitter aperture and the range point \vec{r} due to the

the turbulence in the intervening path. Similarly, the scattered wave in Eq. (I-6) should be multiplied by the factor $\exp[\chi(\vec{r}', \vec{r})]$ to account for perturbations in the log amplitude in the returning beam. Thus, instead of Eq. (I-10), the signal current due to an individual particle now is equal to the real part of the expression

$$\frac{\sqrt{2\sigma} \alpha A_t^2 n}{\pi L^2 R_t^2 \lambda} \iint \exp\left\{-\left[\vec{r}''^2/R_t^2 + (\vec{r}' - \Delta\vec{r})^2/R_r^2\right] + i(\Delta\omega t + \Phi)\right\} d\vec{r}'' d\vec{r}', \quad (I-27)$$

where the phase term Φ is given by the relation

$$\begin{aligned} \Phi(\vec{r}'', \vec{r}', \vec{r}) = & 2kL + \frac{\pi}{\lambda} \left[(\vec{r} - \vec{r}'')^2/L - \vec{r}''^2/f_t - (\vec{r}' - \Delta\vec{r})^2/f_r + 2(\vec{r}' - \Delta\vec{r}) \cdot \vec{n}_r \right. \\ & \left. + (\vec{r} - \vec{r}')^2/L \right] - i[\chi(\vec{r}'', \vec{r}) + \chi(\vec{r}', \vec{r})]. \end{aligned} \quad (I-28)$$

After averaging over frequencies of the order $2\Delta\omega$, the mean power per particle (i_s^2) may be shown to be equal to the real part of the expression

$$\begin{aligned} \frac{\alpha^2 A_t^4 n^2 \sigma}{\pi^2 L^4 R_t^2 \lambda^2} \iiint \iint \exp\left\{-\left[\frac{\vec{r}''^2 + \vec{r}'''^2}{R_t^2} + \frac{(\vec{r}' - \Delta\vec{r})^2 + (\vec{r}''' - \Delta\vec{r})^2}{R_r^2}\right]\right. \\ \left. + i[\Phi(\vec{r}'', \vec{r}', \vec{r}) - \Phi(\vec{r}''', \vec{r}''', \vec{r})]\right\} d\vec{r}' d\vec{r}'' d\vec{r}''' d\vec{r}'''. \end{aligned} \quad (I-29)$$

In evaluating the expected value of the signal power ($\langle i_s^2 \rangle$), we need to calculate the value of the expression

$$\left\langle \exp \left\{ \left[\chi(\vec{r}', \vec{r}) + \chi(\vec{r}'', \vec{r}) - \chi(\vec{r}''', \vec{r}) - \chi(\vec{r}'''', \vec{r}) \right] \right\} \right\rangle$$

where the brackets, $\langle \rangle$, denote an ensemble average over the various possible distributions of atmospheric inhomogeneities. An approximate representation of this expression can be obtained if the variations in the log amplitude for the outgoing and the returning paths are assumed independent. This approximation will underestimate the turbulence effects somewhat. With this assumption the ensemble average may be shown to be equal to the expression

$$\exp \left\{ -\frac{1}{2} [\theta(|\vec{r}' - \vec{r}'''|) + \theta(|\vec{r}'' - \vec{r}'''|)] \right\}$$

where $\theta(r)$ is the wave structure function.

For the Kolmogoroff theory of isotropic turbulence, the wave structure function has the form

$$\theta(r) = (r/r_a)^{5/3} \quad (I-30)$$

where r_a is a parameter dependent on the range, wavelength,

and level of turbulence*. For a plane wave propagating through a turbulent medium of length ℓ , r_a is given by the relation

$$r_a = 0.0581 \lambda^{6/5} / \ell^{3/5} C_N^{6/5} , \quad (I-31)$$

where C_N is the refractive index structure constant. Since we are concerned here with the structure function for a wave originating at the range point (\vec{r}) rather than for a plane wave, the effective length ℓ will be somewhat less than the actual range L . Setting $\ell = L$ will tend to overestimate the turbulence effects.

In order to obtain an explicit evaluation of the expected value of the signal-to-noise ratio, we will introduce one further approximation. Instead of the $5/3$ dependence for the wave structure function in Eq. (I-30), we approximate $\tilde{\delta}(r)$ by the simpler form $(r/r_a)^2$. This dependence on r would result for linear structure function for the temperature fluctuations and corresponds to somewhat greater correlation for small and less for large separations than the more accurate two-thirds law (see Figure I-6). With these approximations, the integration in

*The parameter r_a is equal to 0.314 times Fried's parameter r_0 . We have chosen to use this parameter rather than r_0 in order to simplify the algebraic form of the results.

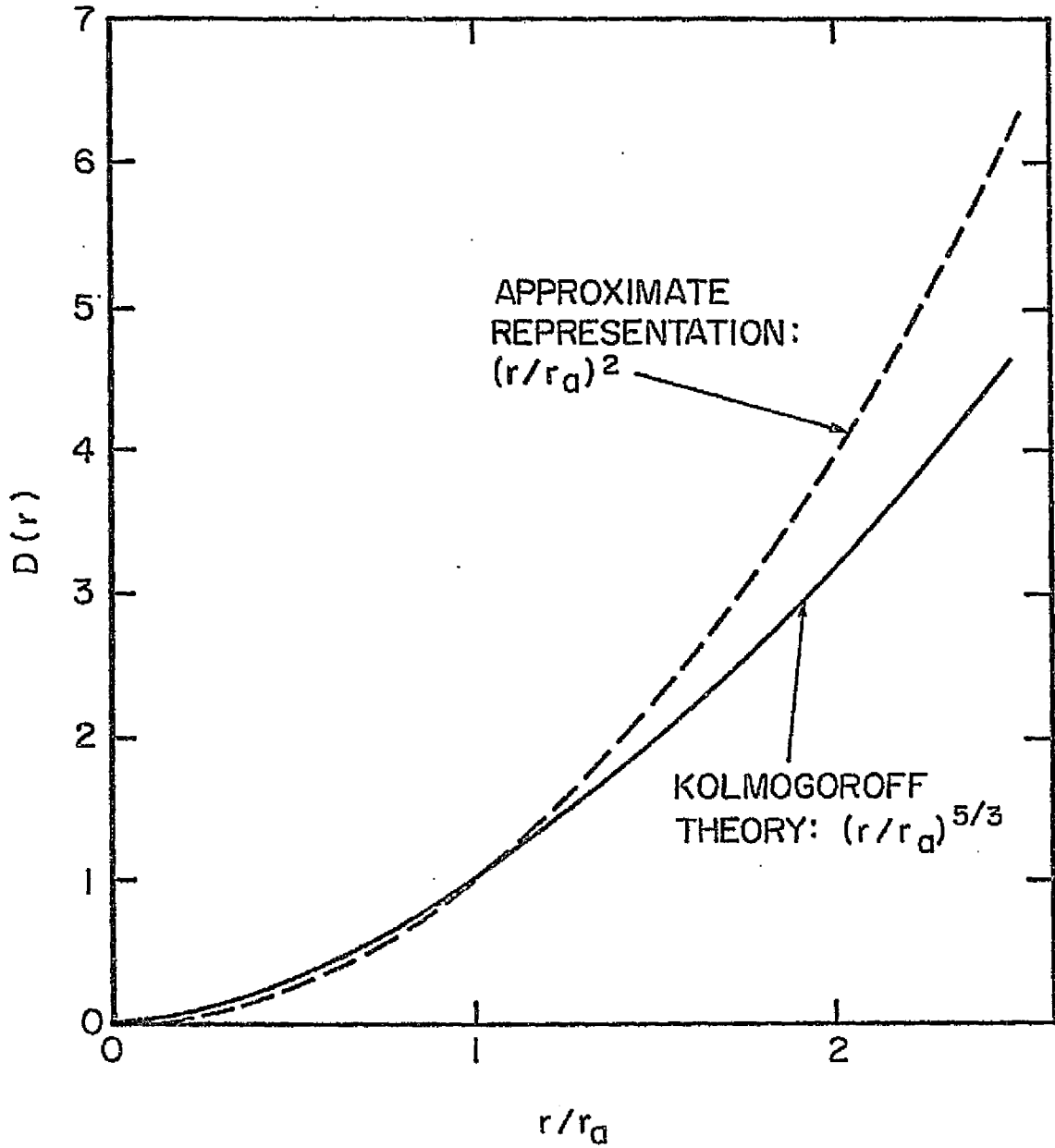


Figure I-6 Approximate and Exact Wave Structure Functions.

Eq. (I-29) may be carried out directly. The result for the expected value of the power signal-to-noise ratio for a single particle is

$$\langle S/N \rangle_{\text{particle}} = \eta N \sigma I_t I_r / \pi L^4 \lambda^2 \quad (\text{I-32})$$

where

$$I_t = \frac{\pi R_t^2}{1 + a_t^2 + \beta_t^2 (1 - \xi_t)^2} \exp \left[- \frac{2 \beta_t^2 (\vec{r}/R_t)^2}{1 + a_t^2 + \beta_t^2 (1 - \xi_t)^2} \right]$$

and

$$a_t^2 = (R_t/r_a)^2.$$

The factor I_r is defined in an analogous fashion. When both transmitter and receiver are focused on the particle, the signal-to-noise is again given by the standard radar equation [Eq. (I-12)] except that the aperture radii R_t and R_r must be replaced by the effective values $R_t r_a / \sqrt{r_a^2 + R_t^2}$ and $R_r r_a / \sqrt{r_a^2 + R_r^2}$. Thus, as expected from the results of Fried⁸ and of Goldstein, et al.⁹, the antennas gains saturate at aperture radii greater than r_a . Values of r_a are moderately small at the visible wavelengths unless the seeing conditions are exceptionally good. Typical values of r_o ($= 3.18 r_a$), measured by Goldstein, et al., are shown in Figure I-7. In Figures I-8 and I-9 we have

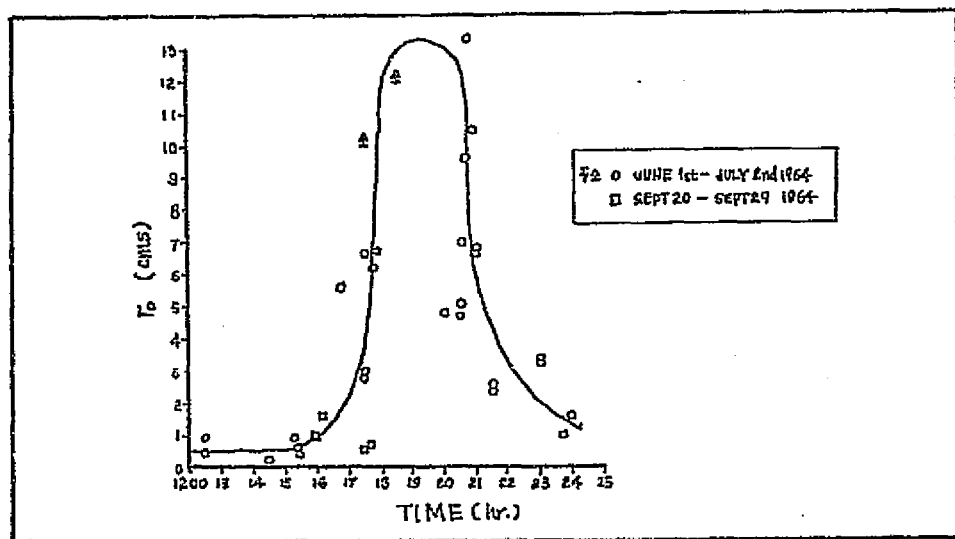


Figure I-7. Measured Values of Effective Aperture Diameter r_0 over a Twelve Hour Period,
 $R = 4$ km (from Goldstein⁹)

reproduced Fried's calculations of the dependence of r_o on wavelength, altitude, range, and turbulence strength.

Returning to the evaluation of S/N, we find that, for a distribution of particles with density n_f that gives rise to Doppler shifts in the band width Δf , the power signal-to-noise ratio is given by an expression identical to that for no atmospheric perturbations:

$$(S/N) = \frac{nN}{2} \left(\frac{\lambda}{\pi\gamma} \right)^2 \int_0^\infty \frac{n_f(L) \sigma \exp\left(-\left\{2(L-L_o)^2 \sin^2\theta / \gamma^2 [(L-L^*)^2 + \Delta L^2]\right\}\right)}{(L-L^*)^2 + (\Delta L)^2} dL \quad (I-33)$$

except that the values of the various parameters now depend explicitly on the value of r_a :

$$\gamma = \sqrt{\theta_D^2 + \theta_G^2}$$

$$\theta_D = \frac{\lambda}{\pi} \sqrt{\frac{1}{R_r^2} + \frac{1}{R_t^2} + \frac{2}{R_a^2}}$$

$$\theta_G = \sqrt{R_r^2 + R_t^2} / f_2$$

$$L^* = f_1 \sqrt{\left[1 + \left(\frac{\lambda f_2}{\pi R_r R_t} \right)^2 + 2 \left(\frac{\lambda f_2}{\pi r_a \sqrt{R_r^2 + R_t^2}} \right)^2 \right]}$$

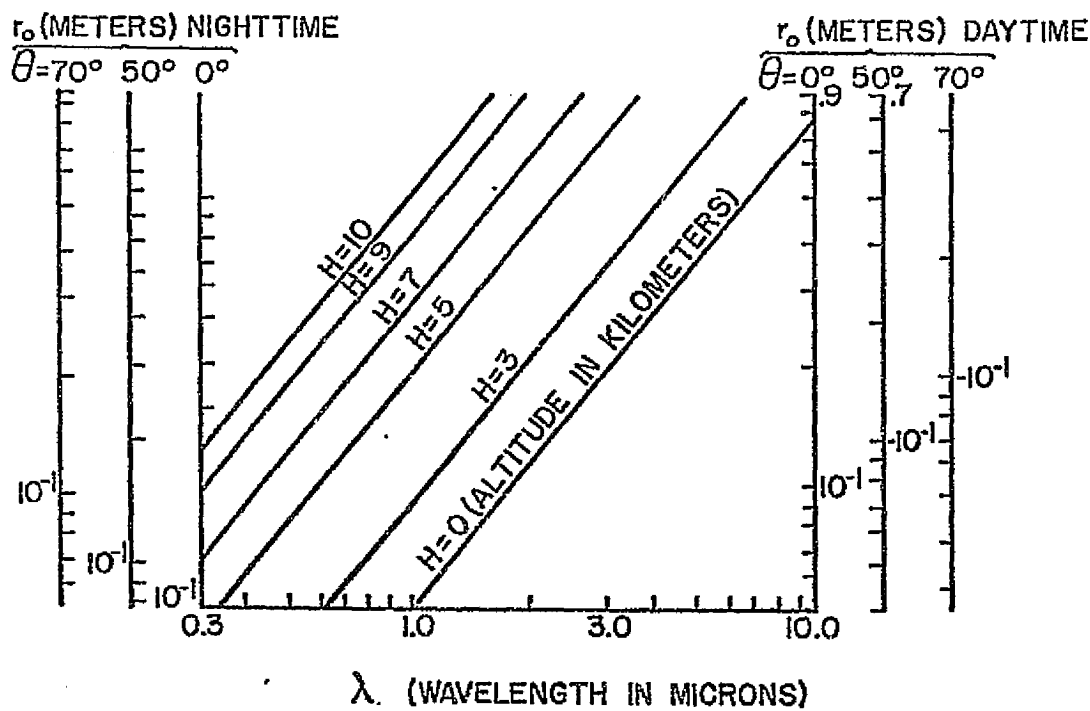


Figure I-8. Dependence of r_o on wavelength and altitude for (1-way) vertical pathlengths, average daytime conditions (from Fried⁸)

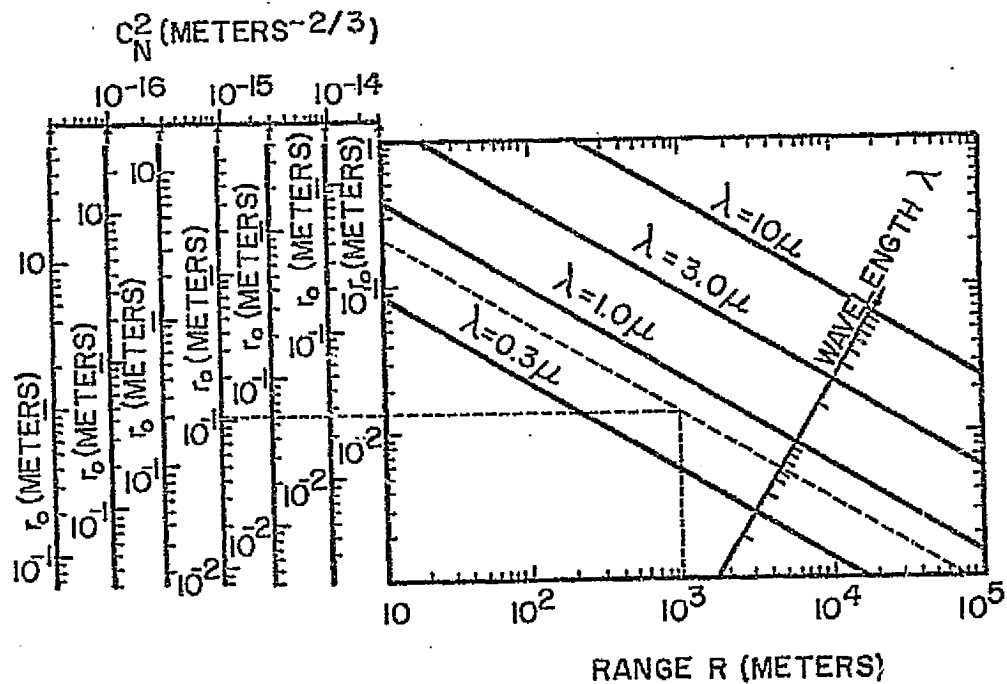


Figure I-9. Dependence of r_o on wavelength, range, and strength of turbulence C_N^2 for horizontal paths. (e.g., $r_o = 10$ cm for $\lambda = .63 \mu$, $R = 10$ km, $C_N^2 = 10^{-15} m^{-2/3}$) (from Fried⁸)

$$\Delta L = f_2 \sqrt{\frac{\left(\frac{\lambda f_2}{\pi R_r R_t}\right)^2 + 2 \left(\frac{\lambda f_2}{\pi r_a \sqrt{R_r^2 + R_t^2}}\right)^2 + \left(\frac{R_t R_r}{R_r^2 + R_t^2}\right)^2 \left(\frac{f_2}{f_r} - \frac{f_2}{f_t}\right)^2}{1 + \left(\frac{\lambda f_2}{\pi R_r R_t}\right)^2 + 2 \left(\frac{\lambda f_2}{\pi r_a \sqrt{R_r^2 + R_t^2}}\right)^2}}$$

(I-34)

At direct backscatter the signal-to-noise ratio is given by (for $R_t = R_r$, $f_r = f_t$)

$$(S/N) = (S/N)^* \sqrt{1 + (R/r_a)^2} \quad (I-35)$$

where

$$(S/N)^* = \eta N \overline{n_f} \sigma \lambda / 4.$$

At large apertures ($R \gg r_a$), the fractional range resolution is equal to $\lambda L/Rr_a$ and the signal-to-noise is $(S/N)^*(r_a/R)$. When the aperture radius is adjusted to get a given range resolution (δL), the dependence of the signal-to-noise on L is given by the relation

$$(S/N) = (S/N)^* (r_a^2 / \lambda L) (\delta L/L) \quad (I-36)$$

At large ranges the apertures required to obtain sharp range resolution become unwieldy. For these conditions

it is necessary to separate the transmitter and receiver to obtain adequate range resolution. In the near field ($L \ll \pi R r_a / 2\lambda$), the optimum signal-to-noise and range resolution are obtained by focusing on the region of interest. For such a focused system, the signal-to-noise ratio may be expressed in a form identical to Eq. (I-36) :

$$(S/N) = (S/N)^* \frac{r_a^2}{\lambda L} \left(\frac{\delta L}{L} \right) . \quad (I-37)$$

The scattering angle required to obtain this spatial discrimination is given by

$$\sin\theta = \lambda/\sqrt{\pi} r_a (\delta L/L) . \quad (I-38)$$

In the far field ($L \gg \pi R r_a / 2\lambda$), both L^* and ΔL are small compared to L and the signal-to-noise ratio is identical to that for collimated beams:

$$(S/N) = \pi^{-\frac{1}{2}} (S/N)^* (r_a^2 / \lambda L) (\delta L/L) / \left[1 + \left(\frac{\pi R r_a}{\lambda L} \right)^2 \right] \\ \approx \pi^{-\frac{1}{2}} (S/N)^* (r_a^2 / \lambda L) (\delta L/L) \quad (I-39)$$

and

$$\sin\theta = \sqrt{1 + \left(\frac{\pi R r_a}{\lambda L} \right)^2} \left[\lambda/\sqrt{\pi} r_a (\delta L/L) \right] \\ \approx (\lambda/\sqrt{\pi} r_a) (\delta L/L) . \quad (I-40)$$

These results may be summarized in the following manner. With high quality optics a signal-to-noise ratio in an optical heterodyne detection system equal to the incoherent value ($\eta N \overline{n_f} \sigma \pi R^2 \delta L / 4\pi L^2$) can always be obtained, in the absence of propagation losses due to atmospheric turbulence, if the transmitter and receiver have identical antenna patterns (i.e., equal apertures and focal lengths) and if both optics are focused on the same point in space. In order to achieve this limiting S/N, the transmitter-receiver separation must be adjusted for each range in such a way as to provide as much overlap as possible consistent with the desired range resolution δL . At a given range there is generally a limit to the maximum achievable value of δL , equal to $\lambda L^2 / R^2$. The achievable S/N is consequently never greater than $\eta N \overline{n_f} \sigma \lambda / 4$. This effect is only of consequence for antenna apertures large enough that the range point is within the near field of the antenna ($L < R^2 / \lambda$). For range points well inside the near field, the optimum scattering angle is 180° and the range resolution is determined primarily by the depth of focus.

Atmospheric turbulence acts to limit the effective useful aperture radius at long ranges to a value dependent on the wavelength, range, and turbulence level (.0581 $\lambda^{6/5} / C_N^{6/5} L^{3/5}$). At short ranges, there is also limit to the effective useful aperture (equal to $\lambda L^2 / \delta L$)

which is determined by the desired range resolution. Thus, use of aperture radii larger than the smaller of these values will not appreciably enhance the signal information. These limiting apertures are plotted in Figure I-10 and I-11 as a function of range, wavelength, and atmospheric turbulence levels. The maximum signal-to-noise ratio that can be achieved with an optimally designed CW system, while maintaining a range resolution capability of 10%, is shown in Figure I-12.

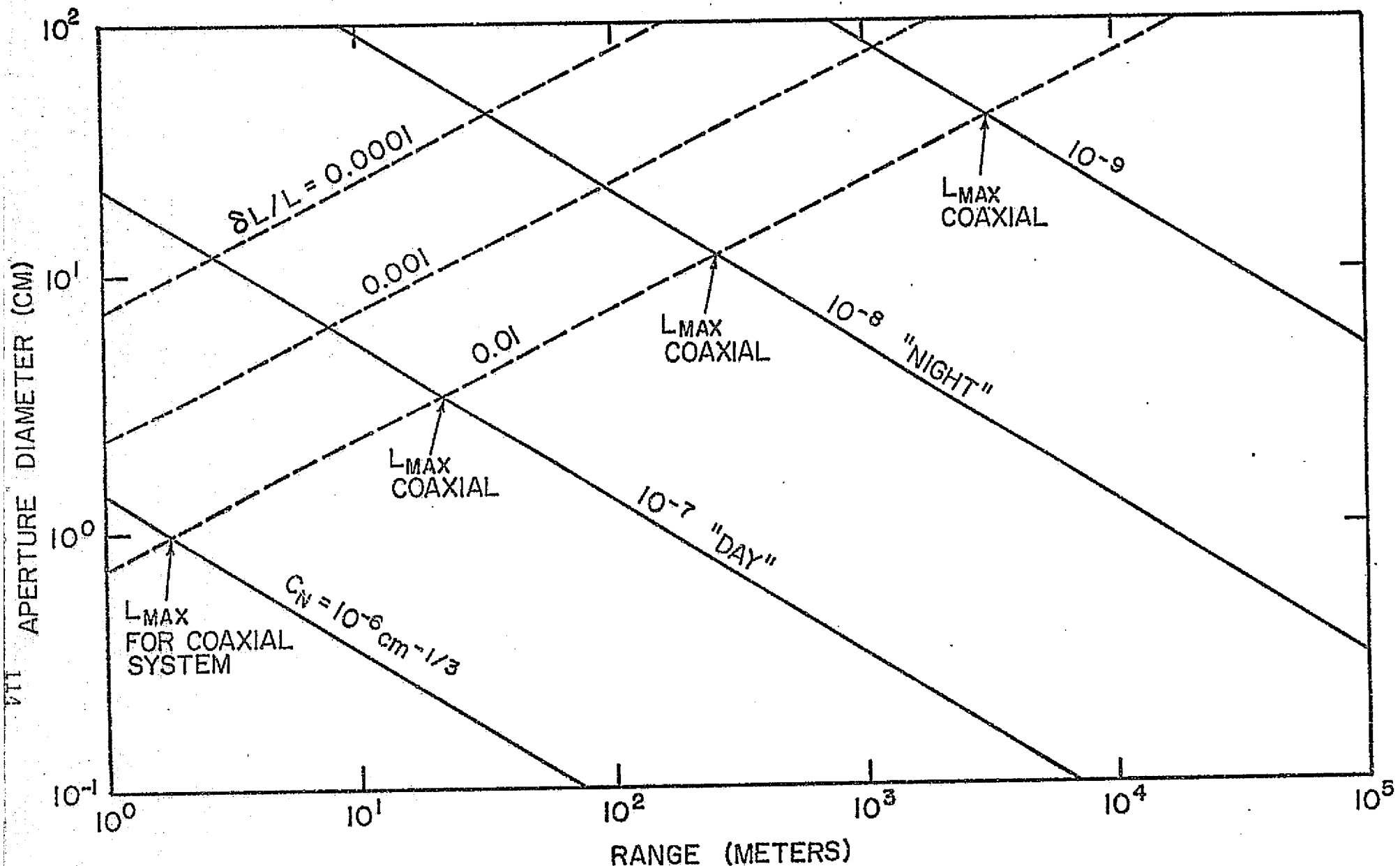


Figure I-10. Dependence of Effective Aperture on Range and Turbulence level,
 $\lambda = 0.5\mu$.

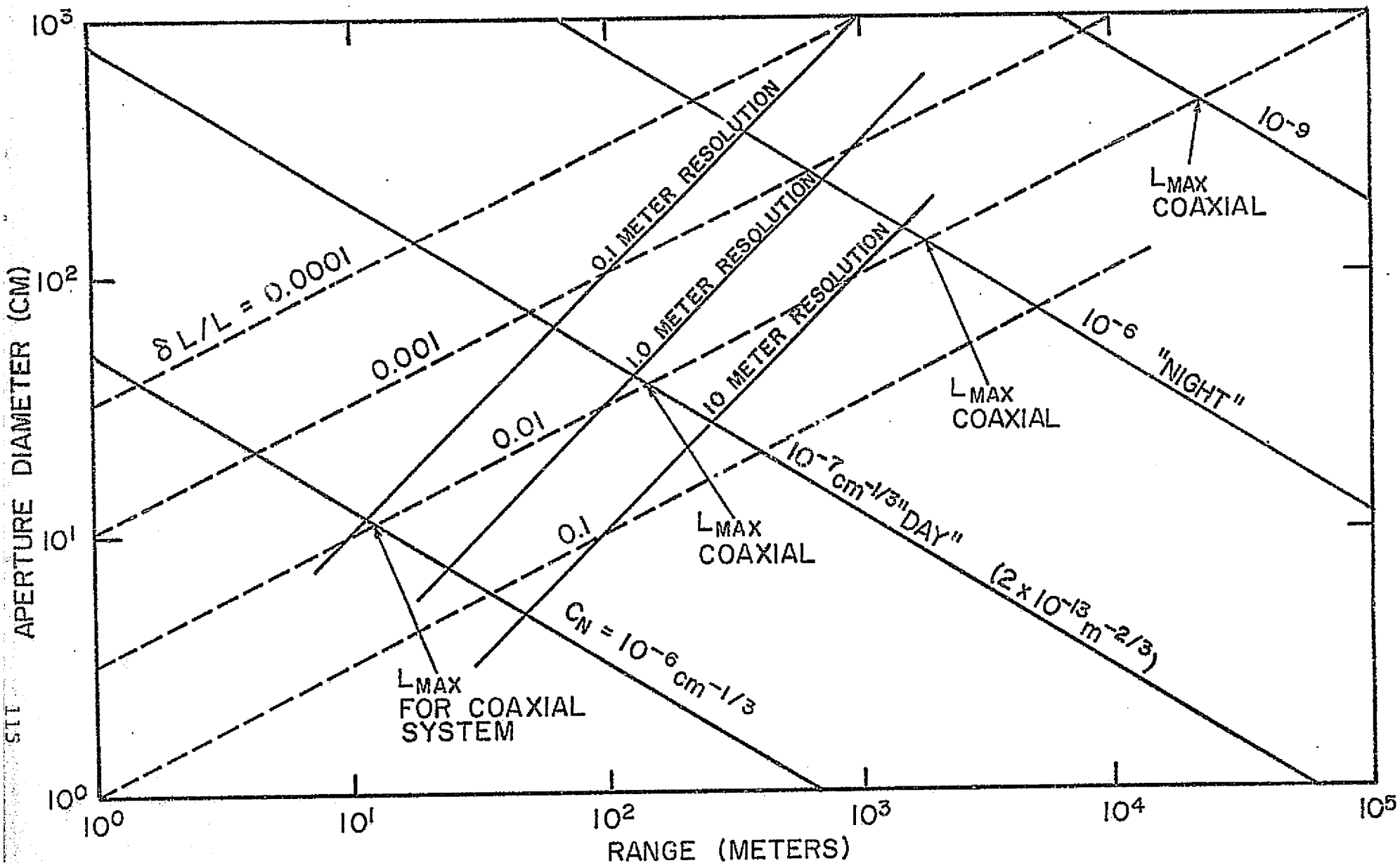


Figure I-11. Dependence of Effective Aperture on Range and Turbulence Level
 $\lambda = 10\mu$.

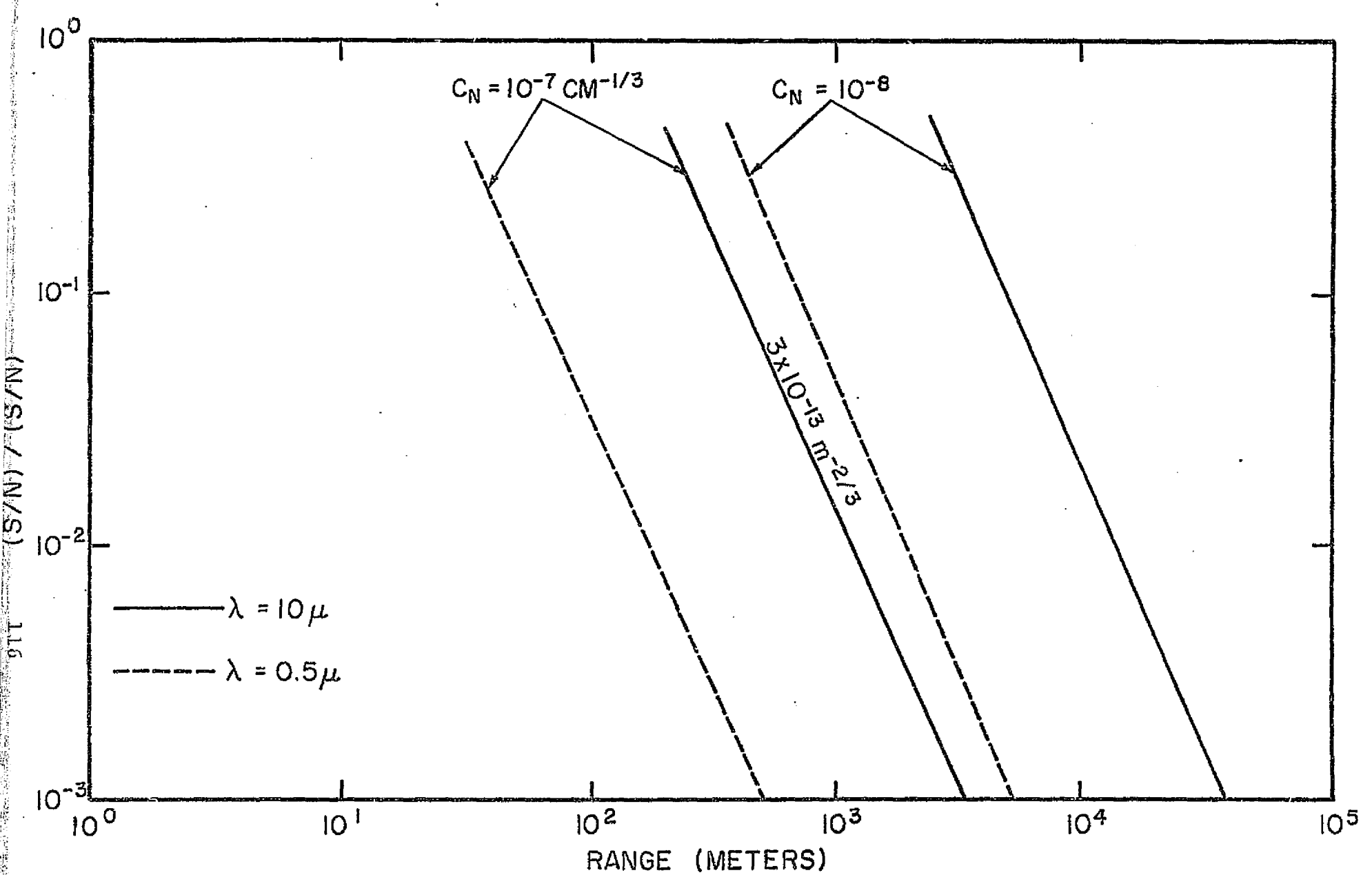


Figure I-12. Dependence of Signal-to-Noise on Range and Turbulence Level.

3.2 Characteristic of Natural Aerosol

In Figure I-13, we show typical distributions of aerosol sizes in continental air. The signal-to-noise for the heterodyne signal is proportional to the mean value of the product $\bar{n}\sigma$:

$$\bar{n}\sigma = \int_0^{\infty} \gamma_{180} \sigma_T(a) \frac{dn}{da} da \quad (I-41)$$

where σ_T is the total scattering cross section and γ_{180} the backscattering efficiency.

The backscattering efficiency for particles is defined as 4π times the ratio of the scattered intensity per unit solid angle at backscatter to the total scattered intensity. Diermendjian has calculated the angular dependence of scattering for haze at a wavelength of 0.7μ (see Figure I-14). A backscattering efficiency of 0.15 has been evaluated from these data by numerical integration. For rough estimates we will estimate σ by the approximate expression

$$\sigma_T \approx 2\pi a^2 \quad \text{for } a > \lambda/2\pi \quad (I-42)$$

$$\sigma_T \approx 0 \quad \text{for } a < \lambda/2\pi$$

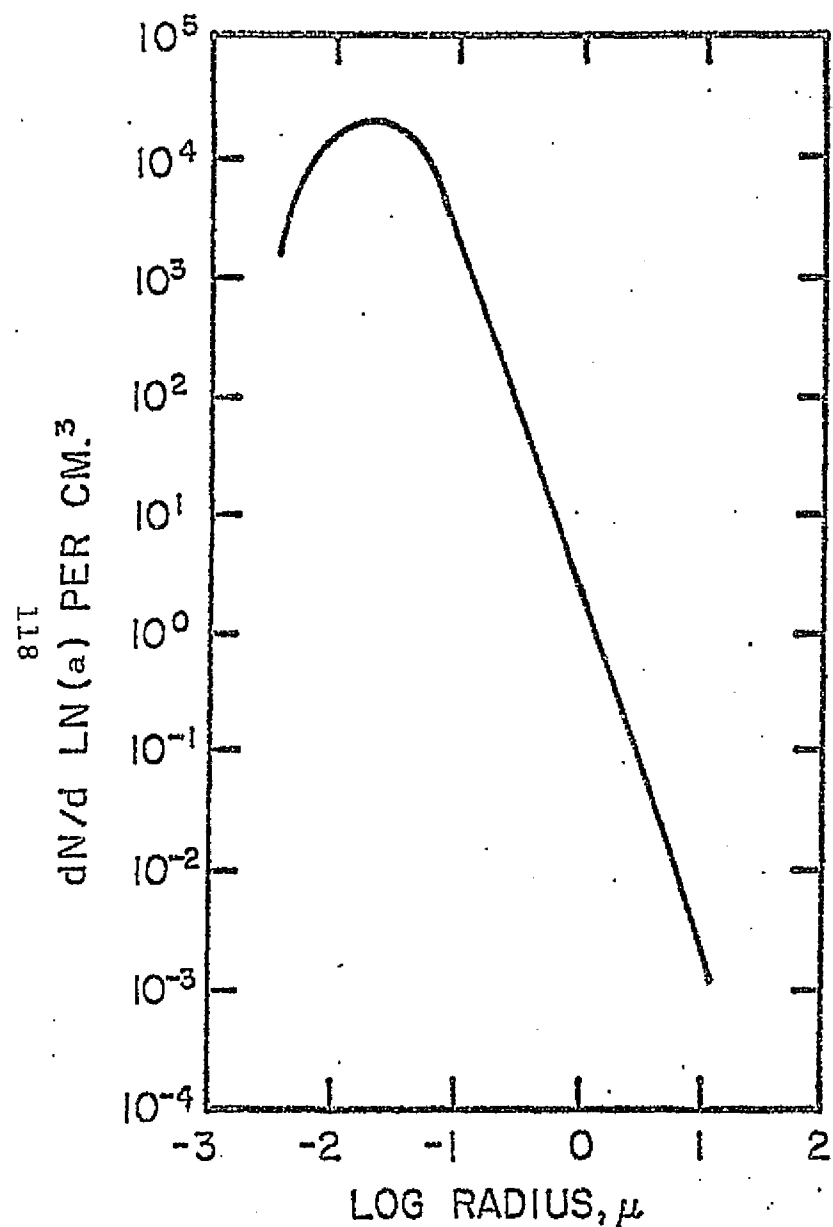


Figure I-13. Aerosol size distribution

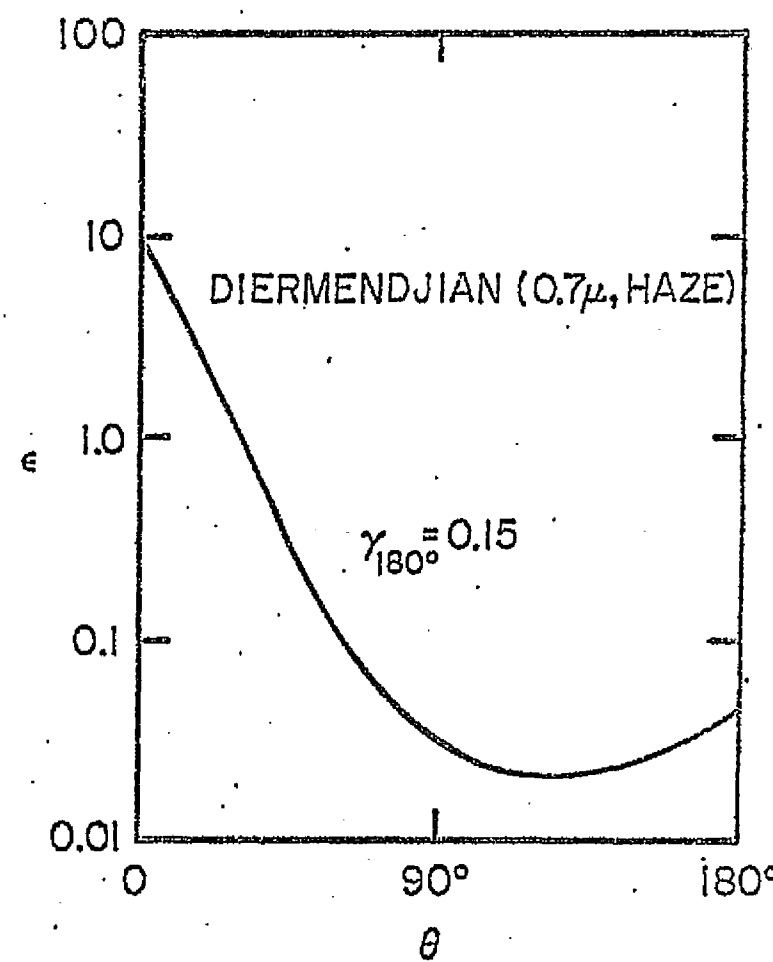


Figure I-14. Angular dependence of aerosol scattering

In continental air the particle size distribution may be roughly represented in the form¹²

$$\frac{dn}{da} \approx n_0 a_0^3 / a^4 \text{ cm}^{-4} \quad (\text{I-43})$$

for $a > 1000 \text{ \AA}$. Thus, the mean value of n_0 is roughly given by

$$\overline{n\sigma} \approx 4\pi^2 \gamma n_0 a_0^3 / \lambda \quad (\text{I-44})$$

From the Handbook of Geophysics model of continental air $n_0 \approx 2 \text{ particles/cm}^3$ when a_0 is chosen equal to 1 micron.

Thus,

$$\overline{n\sigma} = 7.89 \times 10^{-11} \gamma / \lambda \text{ cm}^{-1}$$

At 6000 \AA , $\overline{n\sigma}$ is $0.132 \gamma \text{ per km}$ and at 10.6μ is $0.00744 \gamma \text{ per km}$. These values of the total scattering coefficient and the inverse wavelength dependence are in good agreement with the detailed calculations by McClatchey, et al. (1971), for his clear air model (see Figure I-15.). For other atmospheric conditions, $n\sigma$ may be deduced from the value of the visual range L_v (visibility) which is defined as $3.9/\overline{n\sigma_p}$. Thus, at backscatter

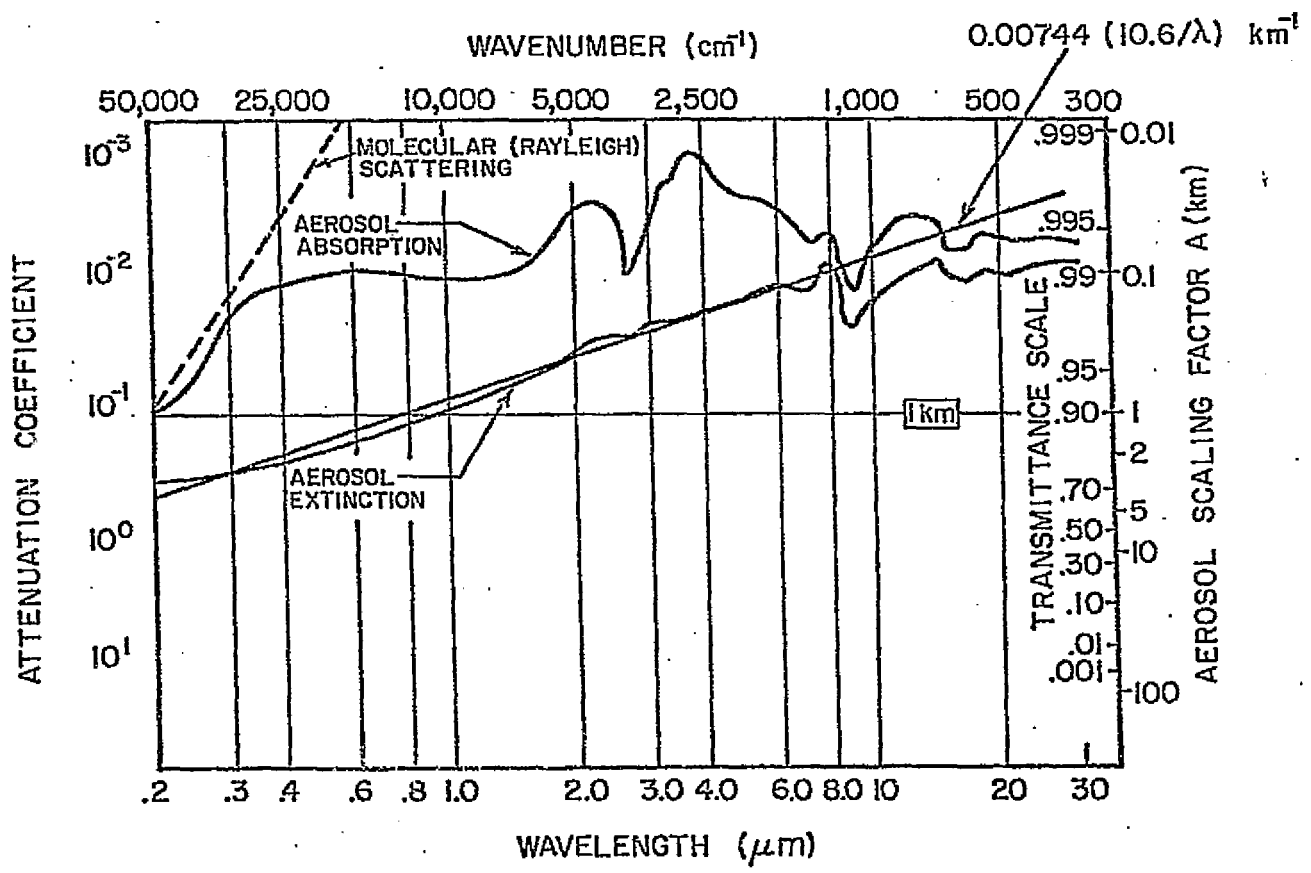


Figure I-15. Attenuation Coefficients (per km) for Aerosol Transmittance (Absorption and Total Extinction)

$$(\overline{n\sigma})_{vis} \approx 3.9 \gamma / L_v \approx 0.6 L_v \quad (I-45)$$

At 10.6μ , the model clear air backscatter cross section is (using $\gamma = 0.15$ and into 4π steradians)

$$\begin{aligned} \overline{n\sigma}_{10.6\mu} &= 1.12 \times 10^{-8} \text{ cm}^{-1} \\ &= 0.0011 \text{ km}^{-1} \end{aligned} \quad (I-46)$$

3.3 Atmospheric Attenuation

At a wavelength of 0.5μ , the predominant contribution to atmospheric attenuation will be aerosol scattering. At 10.6μ , the characteristic wavelength of a CO_2 laser, absorption by atmospheric CO_2 and H_2O will give rise to losses somewhat greater than scattering losses under most conditions.

These losses depend upon atmospheric temperature and humidity, and upon altitude for given atmospheric conditions. CO_2 absorption at the center of the P20 line can be calculated from standard formulas and line intensity data.

Specific expressions are given below:

$$k = S/\pi \alpha_C \quad [0-16 \text{ km}] \quad (\text{I-47})$$

$$k = (S/\alpha_D) (\ln 2/\pi)^{\frac{1}{2}} \exp(a^2) \operatorname{erf}(u) \quad [16-65 \text{ km}] \quad (\text{I-48})$$

$$k = (S/\alpha_D) (\ln 2/\pi)^{\frac{1}{2}} \quad [>65 \text{ km}] \quad (\text{I-49})$$

Here k is the absorption coefficient, S the line strength, α_C the collision half-width, α_D the Doppler half-width

$$\alpha_D = (2kT \ln 2/mC^2)^{\frac{1}{2}} \omega_0 \quad (\text{I-50})$$

and a is given as

$$a = \left[\alpha_C / \alpha_D \right] (\ln 2)^{\frac{1}{2}} \quad (I-51)$$

The collision half-width is a function of both temperature and pressure,

$$\alpha_C = \alpha_C^0 (P_e / P_0) (T_0 / T)^n \quad (I-52)$$

where for the CO_2 P20 line P_e is an effective broadening pressure related to the partial pressure of CO_2 and the total pressure as

$$P_e = 0.3 P_{\text{CO}_2} + P$$

and n is 0.58¹³. From the AFCRL line compilation¹⁵,
 $\alpha_C^0 = 0.072$.

The line strength is a function of temperature according to

$$S(T) = S(T_0) \frac{Q_V(T_0)}{Q_V(T)} \frac{Q_R(T_0)}{Q_R(T)} \exp \left[\frac{hc}{k} E^n \frac{(T-T_0)}{TT_0} \right] \cdot \frac{\left[1 - \exp(-hc\omega_0/kT) \right]}{\left[1 - \exp(-hc\omega_0/kT_0) \right]} \quad (I-52)$$

Here Q_V and Q_R are the vibrational and rotational partition functions, which for CO_2 are approximately

$$Q_V(T) \approx [1 - \exp(-960/T)]^2 [1 - \exp(-1921/T)] [1 - \exp(-3380/T)] \quad (\text{I-53})$$

and

$$Q_R(T) = T/0.561 \quad (\text{I-54})$$

The AFCRL compilation¹⁴ gives $S(296^\circ\text{K})$ as 5.73×10^{-4} $(\text{cm}^2\text{-atm})^{-1}$ and E'' as 1552.046 cm^{-1} , while the central wavenumber ω_0 of the P2O line is 944.19 cm^{-1} .

H_2O produces spectrally continuous absorption in the $8-14\mu$ region. This absorption is produced by the far wings of strong H_2O lines in the 6.3μ or rotational bands or (possibly) with H_2O dimer formation. The absorption coefficient for the P2O line at 296°K can be expressed as¹⁵

$$k = 2.50 \times 10^{-5} (P + 193 P_{\text{H}_2\text{O}}) \text{ cm}^{-1} \text{ atm}^{-1} \quad (\text{I-55})$$

where P and $P_{\text{H}_2\text{O}}$ are the total pressure and the H_2O partial pressure, respectively, in atmospheres. No measurements are available at lower temperatures. The trend at higher temperature¹⁶ is that k decreases with increasing temperature. In the absence of much data on temperature dependence, the above expression for k can be used at atmospheric temperatures.

Conditions in the atmosphere vary considerably with time and position. The U.S. Standard Atmosphere Supplements (1966) contain several model atmospheres which can be used for design studies. Table I-1 gives the temperature and relative humidity at altitudes up to 10 km for several of these model atmospheres. Table I-2 gives the temperature structure at higher altitudes, where the water absorption is negligible with respect to CO_2 absorption. The pressure at a given altitude can be found from the more detailed tables given in the 1966 tables or by using the relation

$$P(h) = P(0) \exp \left[- \int_0^h dh' / H_p \right] \quad (I-56)$$

where

$$H_p = \frac{R}{M} \frac{T}{g} = .0293 T \text{ km} \quad (I-57)$$

is the atmospheric scale height.

Yin and Long¹³ have calculated the CO_2 absorption coefficient as a function of altitude up to 65 km for the P20 line center for the January and July 30°N model atmospheres. Their results for the optical depth per km of path length ($\tau/l = k P_{\text{CO}_2}$) are given in Table I-3 in the form of polynomial fits in different altitude regions.

McCoy, Reusch, and Long¹⁵ have calculated the H_2O absorption coefficient as a function of altitude up to 10 km

Table I-1: Temperature and Relative Humidity as Functions
of Altitude for Several Model Atmospheres

Altitude (km)	15° N		30° N				45° N				60° N				75° N			
	Annual		Jan		July		Jan		July		Jan		July		Jan		July	
	T	H	T	H	T	H	T	H	T	H	T	H	T	H	T	H	T	H
0	299.65	75	287.15	80	301.15	80	272.15	77	294.15	75	257.15	80	287.15	75	249.15	80	278.15	85
1	293.65	75	284.15	70	293.65	65	268.65	70	289.65	65	259.15	70	281.75	70	252.15	65	275.55	75
1.5	--	--	--	--	--	--	--	--	--	--	--	--	--	--	253.65	60	274.25	--
2	287.65	75	281.15	50	288.15	60	265.15	65	285.15	55	255.95	70	276.35	70	250.90	60	272.95	65
2.25	286.15	75	--	--	--	--	--	--	--	--	--	--	--	--	--	--	--	--
2.5	286.95	35	--	--	--	--	--	--	--	--	--	--	--	--	248.15	--	271.65	65
3	--	--	274.65	45	282.65	60	261.65	55	279.15	45	252.75	65	270.95	65	245.40	55	268.40	--
3.5	--	--	--	--	--	--	--	--	--	--	251.15	60	268.25	--	--	--	--	--
4	276.50	35	268.15	35	277.15	50	255.65	50	273.15	40	247.75	60	265.55	60	239.90	50	261.90	55
5	--	--	--	--	--	--	--	--	--	--	240.95	--	260.15	55	--	--	--	--
6	263.50	35	255.15	30	266.15	40	243.65	45	261.15	30	234.15	50	253.15	50	228.90	45	248.90	45
8	250.10	30	242.15	30	252.15	40	231.65	35	248.15	30	220.55	40	239.15	40	217.90	40	235.90	35
9.5	--	--	--	--	--	--	--	--	--	--	--	--	--	--	--	226.15	30	
10	236.70	20	229.15	30	238.15	30	219.65	30	235.15	30	--	--	225.15	30	--	--	226.65	20

Table I-2: Temperature as a Function of Altitude
for Several Model Atmospheres

Altitude km	15° N	30° N		45° N		60° N		75° N	
	all year	Jan	July	Jan	July	Jan	July	Jan	July
0	299.65	287.15	301.15	272.15	294.15	257.15	287.15	249.15	278.15
1	--	--	293.65	--	--	259.15	--	--	--
1.5	--	--	--	--	--	--	--	253.65	--
2	--	281.15	--	--	285.15	--	--	--	--
2.25	286.15	--	--	--	--	--	--	--	271.65
2.5	286.95	--	--	--	--	--	--	--	--
3	--	--	--	261.65	--	--	--	--	--
3.5	--	--	--	--	--	251.15	--	--	--
5	--	--	--	--	--	--	260.15	--	--
6	--	--	266.15	--	261.15	--	--	--	--
8.5	--	--	--	--	--	217.15	--	215.15	--
9.5	--	--	--	--	--	--	--	--	226.15
10	--	--	--	219.65	--	--	--	225.15	--
11.5	--	--	--	--	--	--	--	213.65	--
12	--	216.15	--	--	--	--	--	--	--
13	--	--	--	--	215.65	--	--	--	--
13.5	--	--	--	--	--	--	--	--	230.15
15	--	--	203.15	--	--	217.15	--	--	--
16	--	--	203.15	--	--	--	--	--	--
16.5	193.15	--	--	--	--	--	--	--	--
17	--	203.15	--	--	215.65	--	--	--	--
18	--	203.15	--	--	--	--	--	--	--
19	--	--	--	--	--	--	--	207.65	--
21	--	--	214.15	215.15	--	--	--	--	--
22	215.15	213.15	--	--	--	--	--	--	--
23	--	--	--	--	--	--	225.15	--	--
25	--	--	--	--	--	211.15	--	--	230.15
25.5	--	--	--	--	--	--	--	--	--
27	--	--	--	215.15	227.65	--	--	--	--
30	--	--	--	--	--	--	--	207.65	237.95
32	--	233.15	236.15	219.15	238.15	--	238.65	--	--
34	--	--	--	--	--	220.15	--	--	--
35	--	--	--	--	--	--	--	--	--
37	--	--	--	--	--	--	--	--	--
40	--	--	--	--	--	--	--	--	--
43	--	--	--	--	--	--	271.65	--	--
47	270.15	269.15	272.15	265.65	275.65	--	--	--	--
48	--	--	--	--	--	--	277.15	--	--
50	--	--	--	--	--	260.15	--	--	--
51	270.15	269.15	272.15	--	--	--	--	--	--
52	--	--	--	265.65	275.65	--	--	277.15	--
53	--	--	--	--	--	--	--	--	--
54	254.15	--	--	--	--	260.15	--	--	--
59	--	253.15	256.15	--	--	251.15	265.15	--	--
62	--	--	--	--	250.65	--	--	--	--
65	--	--	--	241.65	--	--	--	--	--

Temperature varies linearly between tabulated altitudes.

Table I-3: Polynomial Coefficients for CO₂ Optical Depth per km of Path Length as a Function of Altitude h in km (30°N, after Yin and Long)

Month	Range	h^0	h^1	h^2	h^3	h^4	h^5
January 128	0-2	6.177301^{-2}	-4.243258^{-3}	3.331791^{-5}			
	2-12	7.1772259^{-2}	-1.018966^{-2}	5.438857^{-4}	-1.440797^{-5}	2.111184^{-7}	
	12-17	2.168201^{-2}	-1.708914^{-3}	4.794412^{-5}	-4.821832^{-7}		
	18-47	2.749415^{-2}	-6.043183^{-3}	4.952857^{-4}	-1.73234^{-5}	2.748747^{-7}	-1.644807^{-9}
	47-51	-5.0246274^{-1}	3.209868^{-2}	-6.729368^{-4}	4.656468^{-6}		
	51-65	1.241526^{-1}	-5.636995^{-3}	8.609204^{-5}	-4.4187473^{-7}		
July	0-15	8.585241^{-2}	-1.439371^{-2}	2.255601^{-3}	-3.082077^{-4}	2.079833^{-5}	-5.087808^{-7}
	15-47	4.409444^{-2}	-8.501794^{-3}	6.408721^{-4}	-2.137128^{-5}	3.280708^{-7}	-1.912325^{-9}
	47-51	-5.381483^{-1}	3.443774^{-2}	-7.221806^{-4}	4.994872^{-6}		
	51-65	8.595289^{-1}	-5.584211^{-2}	1.371591^{-3}	-1.5063^{-5}	6.229936^{-8}	

for the CO₂ P2O line for the January and July 30° N model atmospheres. Their results for the optical depth ($\tau = \int_0^h p_{H_2O} dz$) as a function of terminus altitude for vertical propagation from sea level are

$$\tau(\text{Jan}) = 0.0475[1 - \exp(-0.705 h)] + 0.0877[1 - \exp(-1.15 h)] \quad (\text{I-58})$$

and

$$\tau(\text{July}) = 0.118[1 - \exp(-0.635 h)] + 0.429[1 - \exp(-1.01 h)] \quad (\text{I-59})$$

where h is the altitude in km.

For LDV applications along atmospheric slant paths, one is interested in the two-way loss coefficient

$$\begin{aligned} L(h_2 - h_1) &= L_{CO_2} L_{H_2O} \\ &= \exp\left[-\frac{2}{\cos\theta} \int_{h_1}^{h_2} (\tau/\ell)_{CO_2} dh\right] \\ &\quad \exp\left[-\frac{2}{\cos\theta} \left\{ \tau_{H_2O}(h_2) - \tau_{H_2O}(h_1) \right\}\right] \quad (\text{I-60}) \end{aligned}$$

These expressions can be readily evaluated using the relations given previously.

Aerosol extinction is primarily due to scattering at wavelengths shorter than 6μ. At longer wavelengths (at least in the continental aerosol) aerosol absorption is

comparable to scattering losses. Figure I-15 shows the aerosol attenuation coefficients (optical depth per km of path length) presented by McClatchey and Selby¹⁶. These attenuation coefficients are for a "clear" atmosphere at sea level with a particle size distribution comparable to that of Figure I-13. They scale with particle density for other conditions. Table I-4 gives particle densities as a function of altitude for two aerosol models, the "clear" atmosphere (Visibility 23 km) and a "hazy" atmosphere (Visibility 5 km).

In Table I-5 we compare molecular and aerosol losses at 0.5μ and 10.6μ for level paths at sea level and at 10 km altitude at different ranges and visibilities. These calculations are for the July 30°N model atmosphere and the 5 km and 23 km visibility aerosol models.

Table I-4: Aerosol Models - Vertical Distribution
for a "Clear" and "Hazy" Atmosphere

Altitude (km)	PARTICLE DENSITY N (PARTICLES PER cm ³)	
	23-km Visibility Clear	5-km Visibility Hazy
0	2.828E+03	1.378E+04
1	1.244E+03	5.030E+03
2	5.371E+02	1.844E+03
3	2.256E+02	6.731E+02
4	1.192E+02	2.453E+02
5	8.987E+01	8.987E+01
6	6.337E+01	6.337E+01
7	5.890E+01	5.890E+01
8	6.069E+01	6.069E+01
9	5.818E+01	5.818E+01
10	5.675E+01	5.675E+01
11	5.317E+01	5.317E+01
12	5.585E+01	5.585E+01
13	5.156E+01	5.156E+01
14	5.048E+01	5.048E+01
15	4.744E+01	4.744E+01
16	4.511E+01	4.511E+01
17	4.458E+01	4.458E+01
18	4.313E+01	4.313E+01
19	3.634E+01	3.634E+01
20	2.667E+01	2.667E+01
21	1.933E+01	1.933E+01
22	1.455E+01	1.455E+01
23	1.113E+01	1.113E+01
24	8.826E+00	8.826E+00
25	7.429E+00	7.429E+00
30	2.238E+00	2.238E+00
35	5.890E-01	5.890E-01
40	1.550E-01	1.550E-01
45	4.082E-02	4.082E-02
50	1.078E-02	1.078E-02
70	5.550E-05	5.550E-05
100	1.969E-08	1.969E-08

Table I-5: Atmospheric Attenuation at Different Visibilities,
Altitudes, Ranges and Wavelengths.

Altitude	Visibility (0.5μ)	Range, km	2-way Attenuation in db				
			λ=0.5μ		λ=10.6μ		
			Aerosol	Aerosols	CO ₂	H ₂ O	**
Sea Level	5 km	1	6.76	0.62	0.75	3.78	
		3	20.3	1.84	2.23	11.3	
		10	67.8	6.16	7.46	37.8	
		30	204	18.5	22.3	113	
	23 km	1	1.48	0.13	0.75	2.78	
		3	4.42	0.40	2.23	11.3	
		10	14.7	1.34	7.46	37.8	
		30	44.2	4.02	22.3	113	
		100	147	13.4	74.6	378	
	10 km (1146*)	10	.03	--	1.42	--	
		30	.09	.01	4.27	--	
		100	.30	.03	14.2	--	

*For particle density of Table I-4

** July, 30°N model atmosphere

3.4 Frequency Properties of the Signal

The range of beat frequencies $\Delta f = \frac{2v}{\lambda}$ corresponding to wind velocities from 0 to 20 m/sec will be (0-80 MHz) $\cos\phi$ at 0.5μ and (0-4 MHz) $\cos\phi$ at 10μ , where ϕ is the angle between the line of sight and the velocity vector. The frequency spread due to turbulent eddy velocities within the heterodyne volume will be independent of ϕ , with a half-power width corresponding to the rms eddy velocity.

Frequency broadening due to atmospheric turbulence in the optical path, calculated to be on the order of kilohertz in the preceding section, can therefore be neglected for any reasonable velocity resolution requirement. Broadening due to fluctuations in the laser frequency is larger (of the order of 20 to 100 khz for a non-stabilized single mode laser) and could introduce errors of a few cm/sec into the velocity measurement.

In situations where the total molecular scattering considerably exceeds the particulate scattering (for example, in maritime air), interference by the thermal molecular motion may occur. About 5% of the molecular scattered signal will be present in the frequency range corresponding to velocities from 0 to 20 m/sec. If this component is comparable to the Mie scattering, it will be necessary to provide some sort of discrimination technique to separate the molecular and Mie components.

The particle size distribution for maritime aerosols peaks at about 1μ radius. Palmer and Zdunkowski¹⁷ have estimated the particle density necessary for the particulate backscattering from 1μ particles at a wavelength of 0.7μ to equal the molecular Rayleigh component. Scaling their results to sea level, we find that a particle concentration of 10 cm^{-3} would produce backscattering equal to molecular scattering. Measured values of maritime aerosols are in the 1 cm^{-3} range. Integrated over frequencies corresponding to 0 to 20 m/sec, the Rayleigh and Mie contributions to the power density spectrum are thus expected to be comparable. There are two significant differences in the signals, however. First, the power density spectrum due to molecular scattering will be essentially flat in the frequency range of interest so that scanning the spectrum would provide discrimination.

Second, the angular distribution of wind velocities peaks in the direction of the mean velocity, whereas the thermal molecular velocities are essentially independent of the viewing angle. Thus, spatial scanning would also provide a means of discrimination for systems operating in the visible. Molecular scattering are very weak for infrared systems.

3.5 Choice of Wavelength

Bullrich¹⁸ has shown that the effective mean value of $\bar{n}\sigma$ for atmospheric aerosols in continental air varies inversely as the wavelength for λ between 0.1 and 20μ (see also Figure I-15). This conclusion is essentially dependent on the existence of an inverse cube dependence on the particle radius for $dn/dlogr$ (see Figure I-14). For this type of particle distribution, the signal-to-noise ratio per joule output for an optimally designed system should exhibit a linear dependence on wavelength in the near field and a $\lambda^{2.4}$ dependence in the far field (assuming that comparable quantum efficiencies can be obtained at any wavelength). In terms of the net laser output energy E (joules), the maximum signal-to-noise ratios are given by the expression.

$$\begin{aligned} (S/N)_{\max} &= 1.25 \times 10^{22} \eta E \xi \lambda && \text{for } L < L_n \\ &= 4.2 \times 10^{19} \eta E \xi (\delta L/L) \lambda^{12/5} / C_N^{12/5} L^{11/5} && \text{for } L > L_n . \quad (I-61) \end{aligned}$$

Here ξ is the wavelength independent scattering function $\bar{n}\sigma$ and L_n is the near field range.

Thus, the figure of merit to consider in the selection of a CW laser is $\eta E \lambda$ at short ranges and $\eta E \lambda^{12/5}$ at long ranges (with, of course, the requirement that the detector be able to respond to the megahertz beat frequencies). Since

available quantum efficiencies in the infrared are,
if anything, greater than in the visible, there is a strong
bias in favor of long wavelengths, especially for long range
applications.

3.6 Requirements on Detector Frequency Response

In Table I-6 we have tabulated the maximum detector time constants that can be tolerated for the detection of radial velocities in the 0 to 20 meter/second range for visible and IR wavelengths and for both a stationary platform and a platform moving at a velocity of 300 meters/second.

Table I-6: Time Constants Required to Detect Atmospheric Motion in the Range 0 to 20 m/sec ($\tau = 1/2\pi f$)

λ	Stationary	Observer Moving
	Observer	at 300 m/sec
0.5 μ	2 ns	0.15 ns
10 μ	40 ns	3 ns

These rather stringent requirements for very fast detectors can be softened considerably (to time constants of the order $1/2\pi \Delta f = \lambda/4\pi\Delta v$, where Δv is the velocity resolution desired) if the frequency of the local oscillator can be suitably controlled. For Δv of the order of 2 m/sec, this would permit use of detectors having time constants in the more easily obtainable range of 20 nanoseconds in the visible and 400 nanoseconds in the infrared. Separate tuning of the local oscillator can be obtained by using separate, frequency stabilized, and tunable lasers for the transmitter

and the local oscillator. Alternately, single or multiple reflection of the reference beam from a moving mirror will permit sweeping of the local oscillator frequency. This latter technique is most useful when sinusoidal repetitive sweeping of the local oscillator frequency is acceptable.

3.7 Signal-to-Noise for Various Applications

In a typical coaxial heterodyne system, both the transmitted and received beams suffer a 50% loss at the beam splitter. In a side-by-side system, these losses can be reduced by using beam splitters with transmission $> 50\%$. The following calculations will thus be somewhat conservative for side-by-side systems. Some sort of modulating chopper is assumed to achieve the narrow band detection corresponding to integration times on the order of seconds. An efficiency of 25% in the remaining optical and electronic components would result in an overall optical-electronic efficiency in the neighborhood of 3%.

Assuming 3% optical efficiency, 20% quantum efficiency and a range resolution requirement of 10%, the signal-to-noise per joule of transmitted energy is presented in Figure I-16 as a function of range in maritime and continental atmospheres at wavelengths of 0.5 and 10μ and for turbulence levels of 10^{-7} and $10^{-8} \text{ cm}^{-1/3}$. Atmospheric attenuation has been neglected for the sake of clarity.

In order to be able to measure the mean wind velocity to within 10%, it is estimated that the power S/N should be at least 300. Using a 10 watt CW Argon laser operating at 0.48μ , the daytime detection range is thus seen to be on the order of 100 meters in a maritime atmosphere and a few hundred meters in continental air, assuming an integration

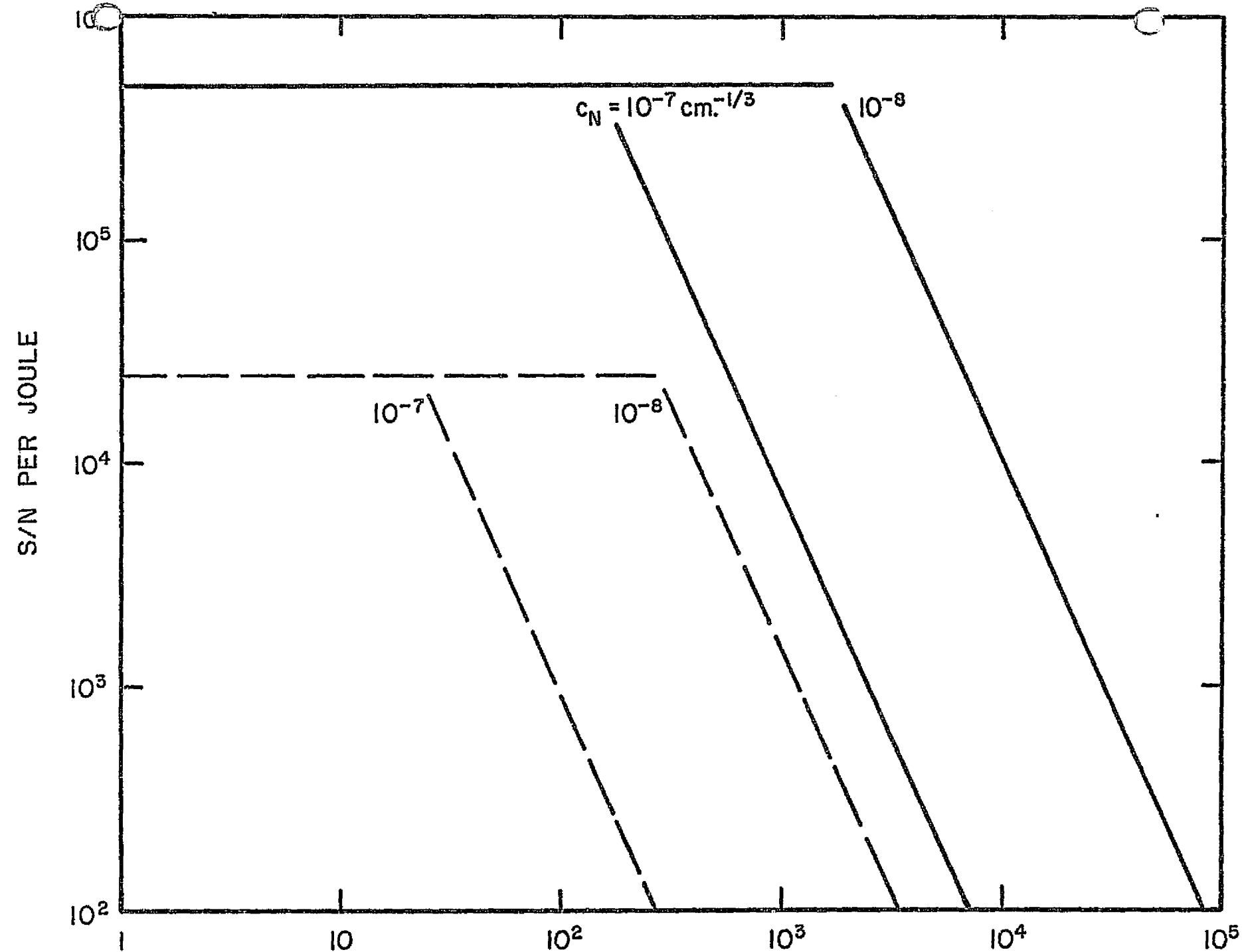


Figure I-16 Signal-to-Noise per Joule vs. Range.
(Continental Air)

time of one second. A 10 watt CO₂ laser (10.6 μ) would extend the effective daytime measurement range to something like 10 km. Coupled with the fact that 10 watts is currently the upper limit of available CW lasers in the visible, with efficiency (ratio of power out to power in) considerably less than 0.01%, whereas CO₂ lasers provide up to one kilowatt CW power with efficiency better than 10%, it would appear to be strongly desirable to go to 10.6 μ .

Disadvantages of operating at 10.6 μ include the necessity of cooling the detector (best detector available with adequate frequency response is Ge:Hg, which must be cooled to less than 40°K), a requirement for CO₂, N₂, and He flow for the laser (although sealed units are now beginning to appear on the market) and difficulty in aligning the optical system outside of the visible region.

In most applications, the advantages of a CO₂ system will outweigh the disadvantages. For long-term untended operation, however, the requirement for liquid He (or H₂) may preclude the long wavelength system.

To evaluate the effect of a physical limitation on the size of the optical system, which may be the case in some practical applications, the two upper curves in Figure I-16 illustrate the degradation in S/N as a function of range if the aperture diameter is limited to 30 cm. For daytime turbulence, the effect is negligible; for nighttime turbulence levels, the S/N may be reduced by as much as an order

of magnitude from the S/N achievable with no size limitations on the optics. The effect is more pronounced at altitude where lower turbulence levels permit the use of large apertures. Figure I-17 illustrates the S/N per joule as a function of range at an altitude of 10 km. If one assumes an upper limit of 30 cm for the aperture diameter (which would be a reasonable upper limit for aircraft), the S/N advantage of the longer wavelength is negated by the size restriction.

In Figure I-18 two of the curves from Figure I-16 are reproduced and the effects of atmospheric attenuation are included. From the figure it can be seen that atmospheric attenuation becomes important at ranges where the S/N is becoming marginal, putting rather sharp limits on the detection range possible.

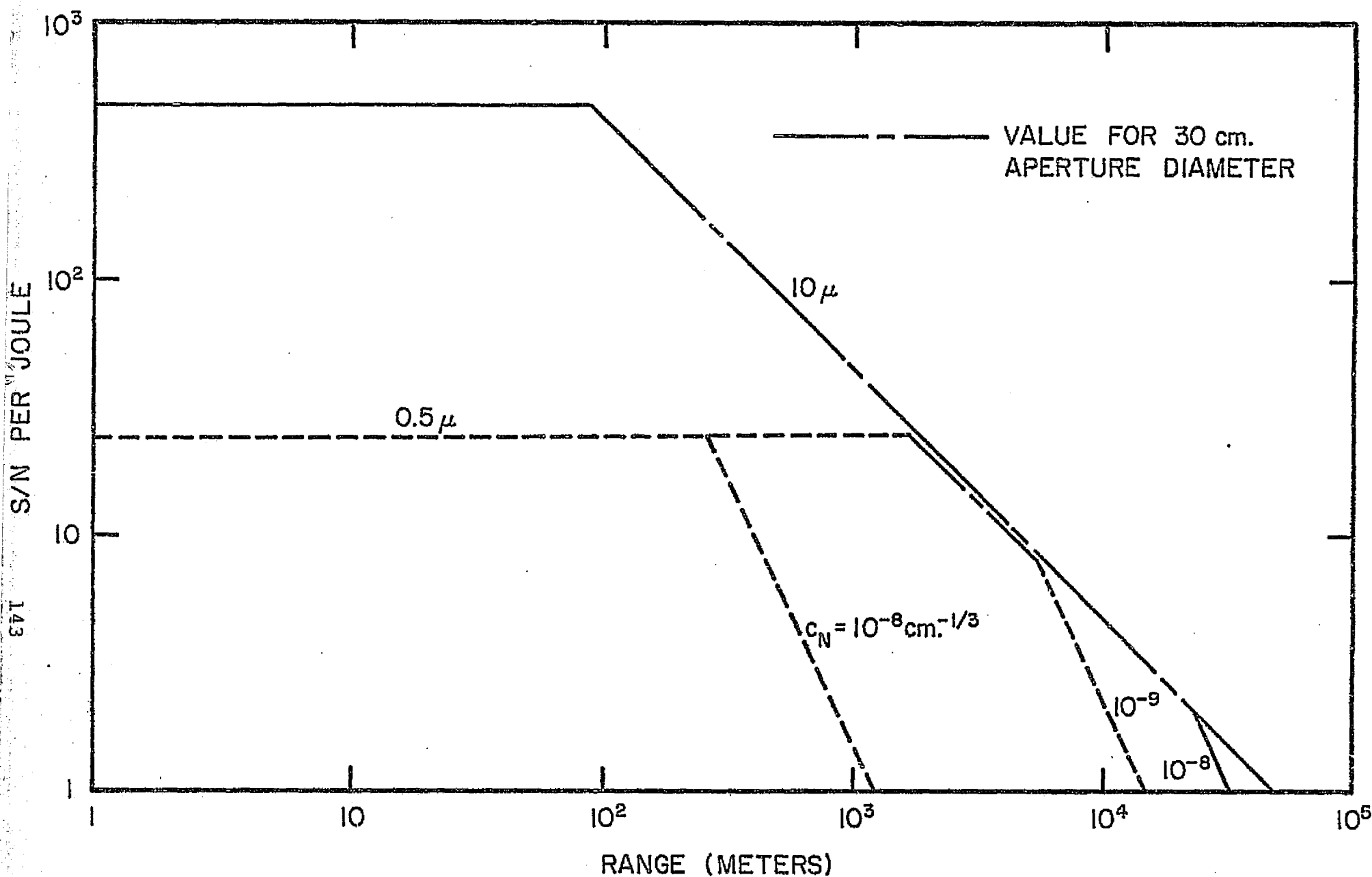
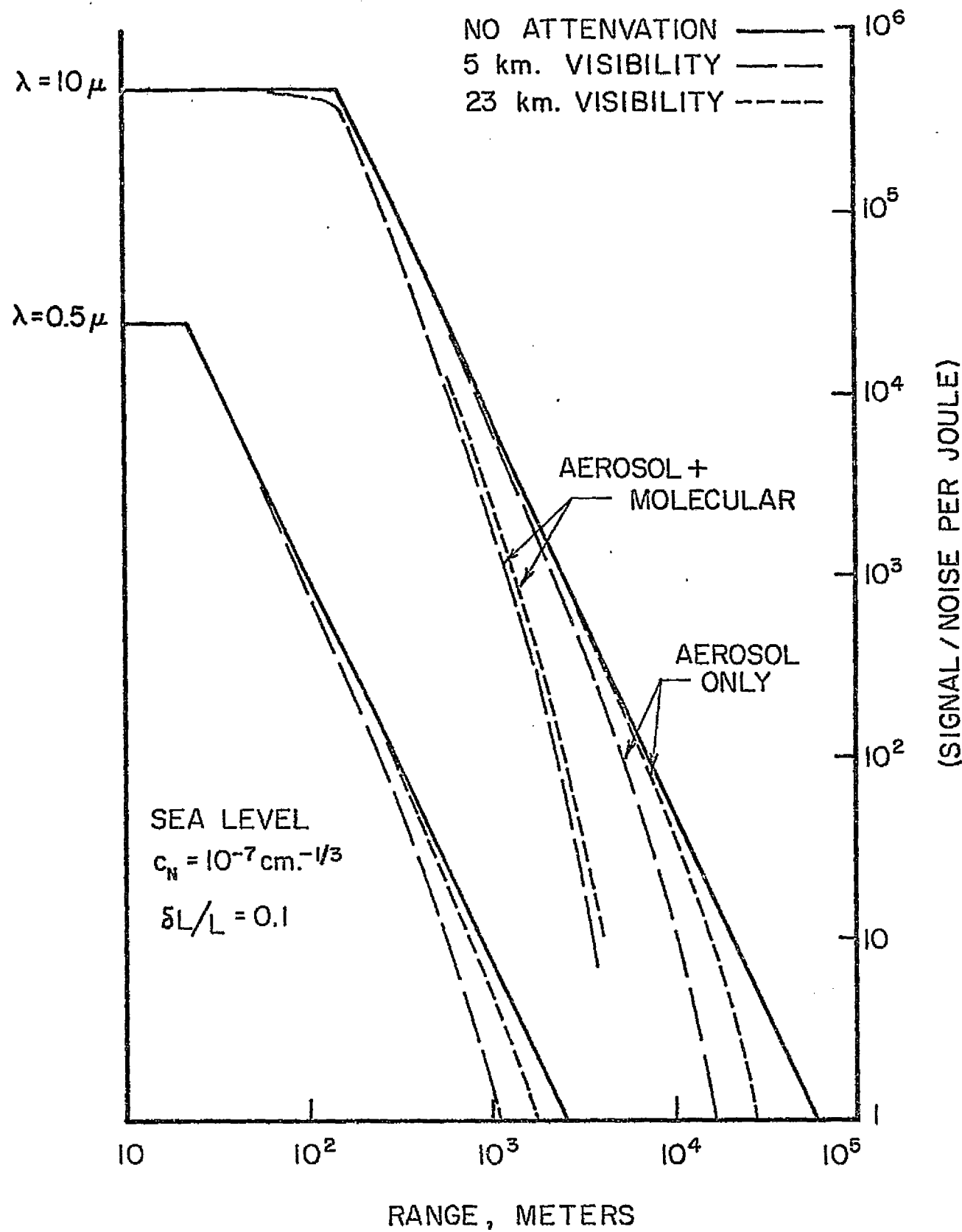


Figure I-17 Signal-to-Noise per Joule vs. Range and Turbulence Level for Horizontal Path at 10 km Altitude.

Figure I-18. Signal-to-Noise per Joule vs. Range
(Atmospheric attenuation included).



3.8 CW versus Pulsed Doppler Lidars

The theoretical limits for the S/N values that can be achieved in an optimally designed heterodyne system are the same for both pulsed and CW operation so long as diffraction limited antenna patterns can be achieved in both modes. Thus, the detectivity limit for ideal systems is dependent only on the average output power level. Large differences can be expected, however, in practical implementation. The major advantages of a pulsed system are that a single coaxial system can be used at all ranges and that range resolution is obtained automatically with time, whereas in a CW system at long ranges, separate transmitter and receivers are required and a precision mechanical adjustment of the scattering angle is needed to change ranges. Also, a pulsed system is much less sensitive to the detailed structure of the antenna pattern, whereas a CW system can suffer greatly from the existence of side lobes. Nevertheless, if greater mean, single mode, diffraction limited output powers can be obtained in CW operation, it is clear that this mode would have the greatest inherent sensitivity. Thus, a CW system coupled with amplitude or frequency modulation or coding techniques to obtain the ranging advantages of a short pulse system may be the more appropriate for practical applications.

3.9 A NOTE ON PREDOMINANT NOISE IN THE HETERODYNE SIGNAL

In the preceding discussion, the limiting noise in the heterodyne signal was assumed to be the photon noise in the reference beam. The conditions under which this assumption is justified are as follows.

In most heterodyne systems, the reference beam is attenuated to avoid detector saturation and to minimize the effects of any intensity fluctuations in the reference beam which might occur at the heterodyne frequency. If, after this attenuation, the signal is still limited by shot noise in the reference beam, the S/N will be independent of the actual value used for the attenuation.

The noise terms which must be evaluated include the photon noise in the scattered signal, given by $n \cdot \tau \frac{\lambda}{4}$, fluctuations in the laser output at signal frequencies, given by $\alpha n \cdot \tau \delta$, where α is the attenuation of the reference beam and δ the fractional fluctuation per unit bandwidth, detector noise given by $2 i_d \tau$ and background noise. The worst background condition will be that for sunlit clouds, given by $\frac{n N_\lambda \Delta \lambda \tau}{hv} \Omega A_C$, where N_λ is the spectral radiance of the clouds, Ω the acceptance angle and A_C the collecting area of the receiver optics. For a diffraction limited system the product of the solid angle of acceptance and the collecting area is equal to λ^2 .

A comparison of these terms and the implied restrictions on the attenuation coefficient α are given in Table I-7. For strong signals, i.e., when the scattered intensity exceeds the background level and the detector NEP, α is determined as follows:

$$\frac{1}{\delta^2 \eta N \tau} \gg \alpha \gg \frac{n\sigma}{4} \lambda$$

For the example in Table I- ,

$$\frac{6 \times 10^{-17}}{\delta^2} \gg \alpha \gg 6.5 \times 10^{-13}$$

This is equivalent to stating that the S/N given in Figure 15 cannot be achieved if fluctuations in the laser output approach 1% in the frequency range of interest.

A comparison of background and detector noise terms in Table I-7 indicates that detector noise will exceed background noise (for the example chosen), even for the 0.1μ spectral bandwidth assumed in the example. Background levels can be further reduced by orders of magnitude by means of interference filters or monochromators if necessary. Thus, for weak signals, α is determined by detector noise and laser output fluctuations:

$$\frac{1}{\delta^2 \eta N \tau} \gg \alpha \gg \frac{2i_d}{nN}$$

Table I-7: Conditions for Photon Noise in Reference Beam to Predominate

Source	Noise Term	Necessary Conditions	
		General Case	Example*
Reference Beam	$\alpha \eta \dot{N} \tau$		
Scattered Beam	$\eta \dot{N} \tau n\sigma \frac{\lambda}{4}$	$\alpha > \overline{n\sigma} \frac{\lambda}{4}$	$\alpha > 6.5 \times 10^{-13}$
Laser Output Fluctuation	$(\alpha \delta \eta \dot{N} \tau)^2$	$\alpha \ll \frac{1}{\delta^2 \eta \dot{N} \tau}$	$\alpha \ll \frac{6 \times 10^{-17}}{\delta^2}$
Cloud Radiance	$\lambda^2 \frac{N_\lambda \Delta \lambda}{h\nu}$	$\alpha > \frac{N_\lambda \Delta \lambda}{\dot{N} h\nu}^2$	$\alpha > 6.5 \times 10^{-14}$
Detector	$2i_d \tau$	$\alpha > \frac{2i_d}{\eta \dot{N}}$	$\alpha > 8 \times 10^{-13}$

*For following conditions:

$$\lambda = 0.5\mu$$

$$N_\lambda = 10^{-1} \text{ w/cm}^2 \text{ ster } \mu$$

$$\eta = 0.2$$

$$\Delta \lambda = 0.1\mu$$

$$\dot{N} = 3\% \left(\frac{10 \text{ w}}{h\nu} \right) = 7.5 \times 10^{17} \text{ ph/sec} \quad i_d = 6 \times 10^4 \text{ elec/sec} (10^{-14} \text{ amps})$$

$$\tau = 1 \text{ sec}$$

$$\overline{n\sigma} = 1.3 \times 10^{-6} \text{ m}^{-1}$$

or

$$\frac{1}{\delta^2} \gg \alpha \eta N \tau \gg 2i_d \tau$$

For $i_d = 6 \times 10^4$ elec/sec (10^{-14} amps) and $\tau = 1$ sec,
 δ should be not more than a few tenths of a percent.

REFERENCES
(APPENDIX I)

13. P.K.L. Yin and R.K. Long, *Appl. Optics* 7 (1968) 1551.
14. R.A. McClatchey, W.S. Benedict, S.A. Clough, D.E. Burch, R.F. Calfee, K. Fox, L.S. Rothman, and J.S. Garing, "AFCRL Atmospheric Absorption Line Parameters Compilation", AFCRL-TR-73-0096, Environmental Research Papers No. 434, January 1973.
15. J.H. McCoy, D.B. Rensch, and R.K. Long, *Appl. Optics* 8 (1969), 1471.
16. R.A. McClatchey and J.E.A. Selby, "Atmospheric Attenuation of Laser Radiation from 0.76 to 31.25 μ m", AFCRL-TR-74-0003, Environmental Research Papers No. 460, 3 January 1974.

APPENDIX II

Doppler Offset

One of the principal problems with the current airborne system is a ringing effect that allows the transmitter to continue to transmit small amounts of energy after its nominal cutoff time.

The Doppler frequency offset in a ground-based system is small and some method for isolating the receiver from scattered radiation from the transmitter is required. For a range of 10 km the round-trip time is $2 \times 10^6 / 3 \times 10^{10}$ = 70μ sec. A mechanical shutter can easily operate in this time, i.e., a disk rotating at 600 rps (36,000 rpm) and having diameter of 4 cm has peripheral speed $2\pi(600) \cdot 2 = 7539$ cm/sec. In 50μ sec a slot at the edge moves $7539 \times 50 \times 10^{-6}$ cm = 0.39 cm = 3.7 mm. Thus, by focusing the beam to a small spot on such a switch and synchronizing the transmitter, the transmitter feed-through can be strongly blocked. Two such switches could be used to eliminate virtually all feed through. At a range of 2 km the round-trip time is 14μ sec (the time after start of pulse that signal begins to return from 2 km). Here we would need a switch that operates in less than 14μ sec, i.e., a slot width of 0.7 mm.

APPENDIX III

In this section we shall derive the dispersion relation for the Helmholtz waves in a confined system of two steadily flowing layers of different densities. Although it is possible to derive the formula for a general three-layer model with the middle layer of higher stability, it is more straight-forward to deal with the asymptotic case when the depth of the middle layer approaches zero and both the top and bottom layers are of constant densities. Because of the constant densities, if the flow is initially irrotational, it will remain so. Velocity potentials ϕ_0 and ϕ_1 exist in both the top and bottom layer. Figure A shows the coordinates and the wave form of the interface.

The equations of motion in the small perturbation limit are:

$$\rho_0 U \frac{\partial u_0}{\partial x} = - \frac{\partial p_0}{\partial x} \quad (\text{III-1})$$

$$\rho_0 U \frac{\partial w}{\partial x} = - \frac{\partial p_0}{\partial z} - \rho_0' g \quad (\text{III-2})$$

$$\rho_1 U \frac{\partial u_1}{\partial x} = - \frac{\partial p_1}{\partial x} \quad (\text{III-3})$$

$$\rho_1 U \frac{\partial w_1}{\partial x} = - \frac{\partial p_1}{\partial z} - \rho_1' g \quad (\text{III-4})$$

where subscript 0, 1 denote the corresponding variables in the top

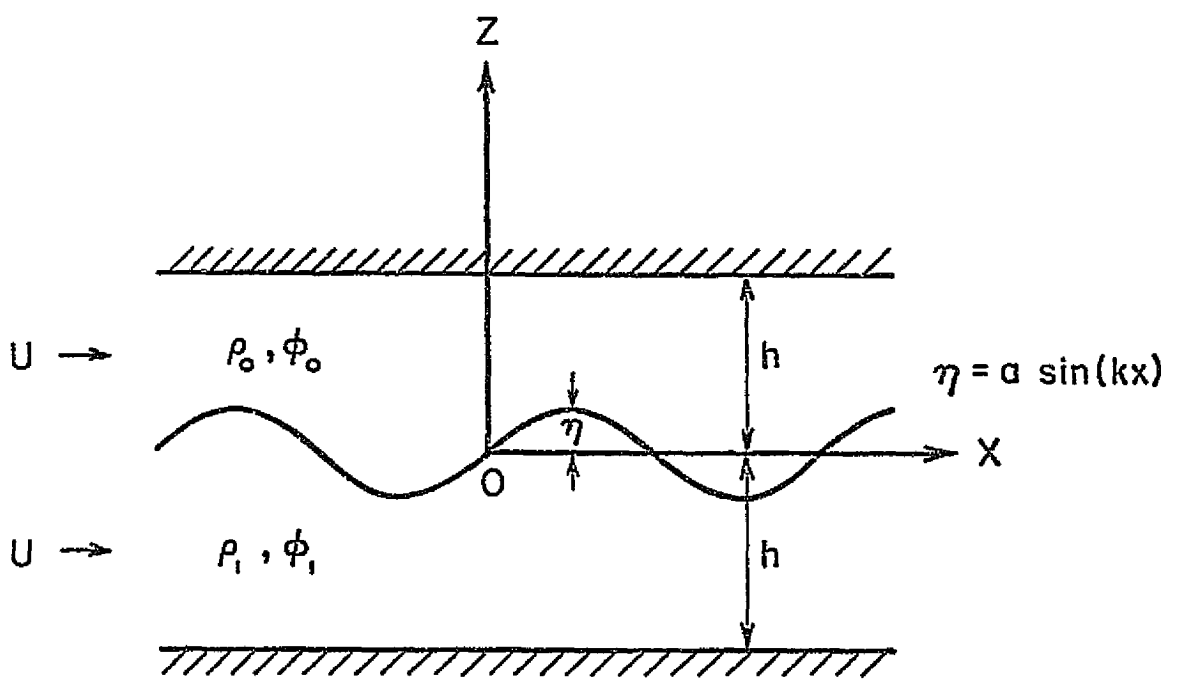


Figure III-1 Sketch of the Two Layer Model

and bottom layer and u , w , p , ρ' are the perturbed variables. Since $\vec{u}_0 = \nabla \phi_0$ and $\vec{u}_1 = \nabla \phi_1$, the pressure can be expressed in terms of ϕ_0 and ϕ_1 by integrating (III-1) and (III-4) with respect to x and z correspondingly. Hence, we obtain:

$$p_0 = -\rho_0 U \frac{\partial \phi_0}{\partial x} \quad (\text{III-5})$$

$$p_1 = -\rho_1 U \frac{\partial \phi_1}{\partial x} - \rho_1' gz \quad (\text{III-6})$$

Assuming a standing wave of the unknown wave number k exists at the interface so that the displacement is given by

$$\eta = a \sin(kx), \quad (\text{III-7})$$

we apply the boundary conditions:

$$\text{kinematic condition: } \frac{\partial \phi_0}{\partial z} \Big|_{\eta} = \frac{\partial \phi_1}{\partial z} \Big|_{\eta} = U \frac{\partial \eta}{\partial x} \Big|_{\eta} \quad (\text{III-8})$$

dynamic condition: the pressure in each layer given by (III-5) and (III-6) should agree at the interface.

Further boundary conditions on the top and bottom walls are that normal velocity should vanish, i.e.,

$$\frac{\partial \phi_0}{\partial z} \Big|_h = 0 \quad (\text{III-9})$$

$$\frac{\partial \phi_1}{\partial z} \Big|_{-h} = 0 \quad (\text{III-10})$$

The general solutions to $\nabla^2\phi = 0$ are

$$\phi_0 = \cos kx \left(A \exp(kz) + B \exp(-kz) \right) \quad (\text{III-11})$$

$$\phi_1 = \cos kx \left(C \exp(kz) + D \exp(-kz) \right) \quad (\text{III-12})$$

Applying the boundary conditions (III-5), (III-6) and (III-8), we can obtain the following relations:

$$\rho_0 U k (A+B) = \rho_1 U k (C+D) - \rho_1' g a \quad (\text{III-13})$$

$$A-B = C-D = U a \quad (\text{III-14})$$

Equations (III-9) and (III-10) require

$$A \exp(kh) - B \exp(-kh) = 0 \quad (\text{III-15})$$

$$C \exp(-kh) - D \exp(kh) = 0 \quad (\text{III-16})$$

Eliminating A, B, C, D from Equations (III-13) through (III-16), we obtain the relation determining the k.

$$k - \frac{g(\rho_1 - \rho_0)}{U^2(\rho_1 + \rho_0)} \tanh(kh) = 0 \quad (\text{III-17})$$

Substituting $\frac{g(\rho_1 - \rho_0)}{U^2(\rho_1 + \rho_0)}$ = .1027 km⁻¹ and h = 10 km, the

root for Equation (17) can be found to be .025 km⁻¹. This agrees well with the numerical result .02576 km⁻¹ obtained from the present code solving a three-layer model. This model is composed of a thin middle layer with a depth one thousandth of that of its neighboring layers. The middle layer stability is 4.52 km⁻¹ which is 1369 times higher than that of both the top and bottom layer.